UNIVERSITÀ DEGLI STUDI DI PADOVA

FACOLTÀ DI INGEGNERIA

DIPARTIMENTO DI INGEGNERIA MECCANICA

TESI DI LAUREA MAGISTRALE
IN INGEGNERIA DEI MATERIALI

Scaffolds ceramici 3D tramite sinterizzazione laser (LSD)

3D ceramic scaffolds by laser sintering (LSD)

Relatore: Prof. Paolo Colombo
Correlatore: Prof. Enrico Bernardo

Laureando: ANDREA ZOCCA

Anno accademico 2011-12

INDEX

2

ABSTRACT

Selective laser sintering (SLS) of layerwise slurry deposition (LSD) and 3D printing were studied for the production of ceramic scaffolds.

SLS of LSD was used with a CO_2 laser on layers deposited from a silica slurry, and it was proved that is possible to build up a scaffold. With LSD a high density of the green layers could be achieved, close to the theoretical maximum packing value.

The surface finish is good in the x-y laser plane, but the surface along the z-axis resulted rough and laddered.

An LAS glass-ceramic slurry was prepared for LSD; even though a good stability and viscosity were achieved, some further research should be done to improve the drying behaviour and the deposition.

The effect of the laser sintering parameters on the LAS layers was studied, with a fiber laser in a power range 15-39 W and scan velocity 20-80 mm/s and an area of stable sintering was determined.

Nevertheless, the sintered layers have a low density (less than 50% of the theoretical value) and a lot of closed big pores.

The influence of the laser parameters on the line width was also investigated, revealing that the minimum width possible for a complete line is about 200 μm.

Some LAS scaffolds were produced by 3D printing, binding the powder with a resin and building the object layer-by-layer. The binder was finally burned and the sample crystallized to form β-spodumene and sintered.

Different printing parameters were used and their effect was analyzed: powder size, printing "passes", layer thickness and curing time.

The best result amongst the samples was obtained using a powder with a size 63-125 μm , increasing the curing time of the resin and doubling the standard number of passes; a higher amount of binder in facts results in a higher green and sintered density.

The surface finish that was obtained with 3D printing is worse compared to the laser sintered surfaces in the x-y plane, but it has the advantage to be uniform along all the three axis, while big differences were noticed for the laser sintering process.

Scaffolds with a geometrical density of 0.9 g/cm^3 have been printed, where also the struts are highly porous, with an opened porosity up to 41%.

CHAP 1: INTRODUCTION

1.1 Motivation

In this thesis, two different rapid prototyping (RP) techniques were employed to produce ceramic scaffolds.

A study on selective laser sintering (SLS) of layerwise slurry deposition (LSD) was performed at Clausthal TU (Germany), Institute for non-metallic materials.

Some experiments with 3D printing were also carried out at BAM (Federal Institute for Materials Research and Testing) in Berlin.

A structure like a 3D scaffold is important in many applications, but it is very complicated or even impossible to produce with the standard ceramic techniques.

1.1.1 3D scaffolds by Rapid Prototyping

The new RP methods introduced in the 90's allowed new outstanding possibilities for producing complex geometries as the 3D scaffolds are, and these soon attracted the interest of the researchers in the medical field.

Using this technology for example, it may become possible to regenerate or replace damaged tissues with laboratory-grown parts such as bones, cartilage, blood vessels and skin **(1)**.

Scaffold-based tissue engineering concepts involve the use of combinations of viable cells, biomolecules and a structural scaffold combined into a construct to promote the repair and regeneration of tissues.

In this field many attention in these last years has been concentrated in ceramic scaffolds made of calcium phosphates and in particular hydroxyapatite **(2)**.

Ceramic scaffolds are interesting also for other applications, as filters, or even sensors, where the ceramic acts like a support for the deposition of the active material.

A transparent glass scaffold for example could be an optimal support for the deposition of a gas-sensing thin layer **(3)**.

In the following paragraphs will be given a general introduction on Rapid Prototyping section 1.2 with a focus on techniques for ceramics (section 1.3).

The two technologies used in Berlin (3D printing) and Clausthal (selective laser sintering of LSD) will be more widely explained, in section 1.4 and 1.5 respectively.

The experimental part will follow, first with the material preparation and characterization (CHAP 2), then properly with the the description of SLS in CHAP 3 and 3D printing in CHAP4.

1.2 A general introduction on Rapid Prototyping

A prototype is an approximation of a product or its components, in some form for a definite purpose in its implementation.

One of the biggest challenges in the last decades has been finding the way to shorten the time between a new idea or project and his production.

This often goes through a step that is the creation of a prototype of the full-scale object, which permits to visualize, analyze and test it.

In the 80's and the 90's, thanks to the improvements in the applications of computer in the industry, many new manufacturing technologies were developed with the name of Rapid Prototyping (RP), all with the intent of reducing the time needed for the development of a prototype.

In particular, the emergence of RP systems would not have been possible without the existence of CAD, that is Computer-aided Design.

The term Rapid Prototyping basically has to be considered in the widest possible meaning, so it includes many different techniques, that have at least two aspects in common.

The first aspect is that RP is almost always performed with an Additive Manufacturing, because the materials is not removed (Subctractive Manufacturing) or just shaped (Formative Manufacturing), but it is added step by step, usually layer by layer.

The second aspect can be explained with the name of Solid Freeform Manufacturing (SFF).

Solid is used because while the initial state may be liquid, powder, pellets or laminates, the end result is a solid, 3D object, while freeform stresses on the ability of RP to build complex shapes with little constrains on its form **(4)**.

Common to all the different techniques is the basic approach they adopt, which can be

described as follows:

1) A model or component is modeled on a CAD-CAM (Computer-aided manufacturing) system. The model which represents the physical part to be built must be represented as closed surfaces.

2) The solid model to be built is next converted into a format dubbed the "STL" file (from Stereolithography that is the first RP technology invented) file format. The STL file approximates the surfaces of the model by polygons.

3) A computer program analyzes the STL file and "slices" the model into cross sections. The cross sections are systematically recreated through the solidification of either liquids or powders and then combined to form a 3D model. Another possibility is that the sections are already thin, solid foils that are glued together

The firsts RP systems where developed to work with resins, because of the low energy and low temperature requirements, that make the process easier and reduce the distortions.
These systems in the years have been adapted to metals and ceramics, and new special systems have been developed.
In the next section a brief introduction on RP techniques for ceramics will be given.

1.3 Rapid prototyping techniques for ceramics

Traditionally the use of technical ceramics has been limited by the difficulty of shaping.
There are many categories of technical ceramics, for example piezoelectrics, magnetic ceramics, gas and humidity sensors, varistors etc. In all these fields, complex shapes may be required.
On one side, high costs for machining or dies makes inconvenient the production of small quantities; on the other side many complicated shapes are very difficult or even not feasible, for example reticular structures or with complex cavities.
These factors delay the prototyping and so all the work of the designers, from the basic idea to the new product.
Industrial applications of ceramic materials especially for the jobbing work and complicated components are largely restricted by the lack of the net-shaping capability for the components with complex structures.

In response of this need, Rapid Prototyping techniques have been developed in the middle 90's also for ceramics, when they were available since middle 80's only for polymers at first and metals later.

There are several processes to realize the net or near-net shaping of the ceramic functional components such as stereolithography, extrusion of ceramic paste, fused deposition of ceramic-loaded polymer filaments, laminated object manufacturing, selective laser sintering of ceramic powder and 3D printing.

The most important of these processes will be summed up, following a review by Tian, Li and Heinrich (2011) **(5)**.

1.3.1 Stereolithography (SL) of ceramic slurry

Stereolithography (SL) was the first rapid prototyping technology to be developed, with its first commercial system marketed in 1988 by 3D Systems company.

Photocuring is the basis of SL, one of the most popular and most accurate SFF techniques.

Commercial SL machines produce plastic prototypes from epoxy resins by photo-polymerization of a liquid monomer with a UV laser.

The SL at the moment can obtain the best surface finishes amongst RP, and one of the best accuracies.

For the 3D-fabrication of ceramics via stereolithography the liquid monomer is replaced by a "ceramic resin", a suspension of ceramic powder dispersed in a UV-curable resin, first demonstrated by Griffith and Halloran in 1996 **(6)**.
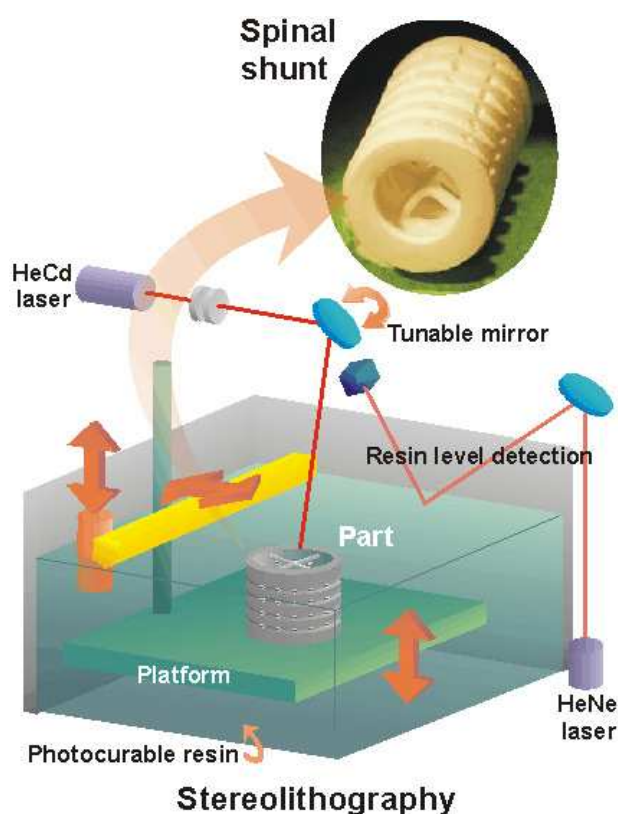
As shown in **fig. 1** [1], the first step is curing a thin layer (150~200 μm) by laser scanning the cross section on the surface of the ceramic resin.

The part is attached by supports to an elevator platform beneath the surface of the

ceramic resin. After curing the layer, the elevator platform dips into the suspension allowing the liquid ceramic resin to flow over the cured portion of the part. A doctor blade sweeps over the surface leaving a layer of fresh ceramic suspension which becomes the next cured layer after the laser curing process. Repeating this process builds up the three dimensional green body of the ceramic components.

Then, after post sintering in furnace, dense ceramic objects are obtained.

---

1   Image from: Ceramic/polymer Composite Materials through Stereolithography
Jim H. Lee, Princeton University ceramic materials laboratory

fig.1 Schematic representation of a Stereolithghraphy process

Lasers used in current practice are helium cadmium gas lasers, argon ion gas laser and more recently solid state Nd-YVO$_4$ lasers.

The main drawback of SL is that the solidified sample is surrounded of liquid material, so a support has to be designed and fabricated.

1.3.2 Extrusion forming techniques

The Fused Deposition Modeling (FDM) was first developed for polymers by Scott Cramp in 1988, patented in the U.S. in 1992 and commercialized by Stratasys (Minnesota).

The Fused Deposition Manufacturing of Ceramics (FDMC) was developed firstly by Ahmad Safari in 1997 **(7,8)**.

Filaments were fabricated with a ceramic powder loaded of 50-55vol% in a six-component thermoplastic binder system that contained polymer, elastomer, pacifiers, wax, surfactant, and plasticizer. The filament with a diameter of about 1.8 mm passes through a heated liquefier (140-200°C) and acts thereby as a piston to extrude a continuous bead, or "road'

of molten material through a nozzle with a diameter of 0.254-1.5mm (**fig.2[2]**).
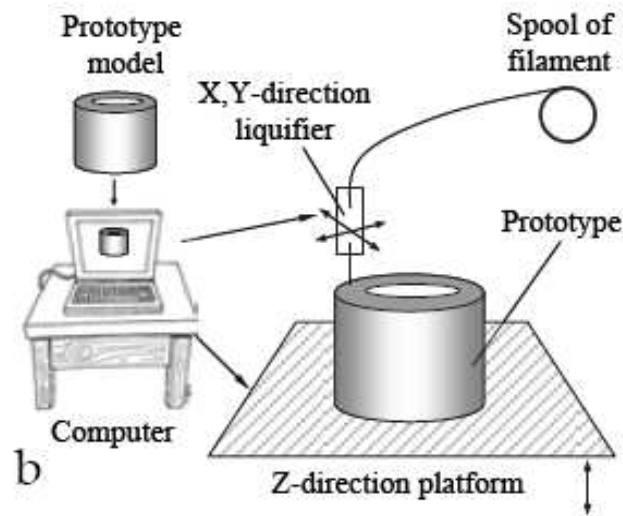
fig.2 Schematic representation of Fused Deposition Manufacturing

The bead is deposited on a platform that indexes down after the first layer is completed. Bonding of neighbouring beads and previous deposited layers takes place due to adhesiveness of partly molten material.

The 3D components were fabricated by repeat this deposition process layer by layer. After the green part was fabricated, the part was removed from the substrate for further heat treatment processing to remove the organic additives.

The main advantages of FDM are the good strength of the parts and the minimum wastage, while the main disadvantages are the limited accuracy, that depends on the nozzle diameter, and the general slowness, caused by the limited extrusion rate.

1.3.3 Three-dimensional printing

There are two kinds of 3D printing fabrication processes. One is the three-dimensional printing which uses layered ceramic powder and organic binder. Another is the direct ceramic ink-jet printing which uses a ceramic powder loaded ink.

The powder based system was used in Berlin with the LAS powder and it will be introduced more in detail in the next section.

---

2   Schematic for the extrusion fabrication process (Bandyopadhyay et al., 1997)

Direct ceramic ink-jet printing (DCIJP) makes use of ink-jet printers to create components by multilayer printing of a colloidal suspension dispersed with ceramic powder.

This process has the potential to produce a wide range of fine ceramic contours with high resolution enabling miniature components to be manufactured. Functional gradients and multi materials components can be fabricated by this printing method according to the multi nozzles. By adjusting the aperture of the printing head and by controlling the spreading phenomenon of the droplet, one can expect to reach a standard definition of around 50μm and ultimately of 10μm, taking into account the tremendous evolution in the printing field **(9,10)**.

1.3.4 Laminated object manufacturing (LOM)

Laminated object manufacturing was invented by Michael Feygin, who set up the company Helisys in 1985, then taken over from Cubic Technologies.

Laminated object manufacturing (LOM) generates three-dimensional ceramic components by sequential stacking, laminating, and shaping of pre-ceramic paper or ceramic green tape (**fig.3[3]**). It can be considered as a hybrid between additive and subtractive processes: a part is built up in a layer-by-layer lamination approach.

Each layer is individually cut by a knife or laser beam according to the cross section of the part defined by the CAD model. Each layer is bonded to the previous layer with a thermoplastic adhesive coating on the bottom side of the paper sheet, which is activated by heat and pressure during the LOM processing.
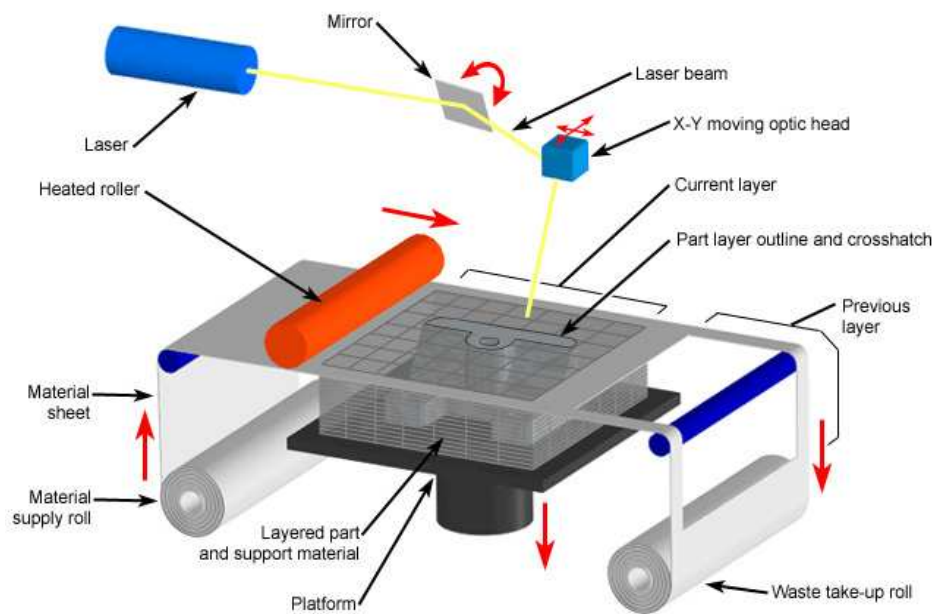
Al_2O_3 and SiC pre-ceramic papers have been prepared for the LOM process **(11)**. Commercial Low Temperature Co-fired Ceramic (LTCC) green tapes were also used to fabricate complicated ceramic components by Cold Low pressure Lamination [CLPL] process **(12)**.

For LOM the main advantages are the wide variety of materials that can be used, a fast build time (only the outlines have to be scanned) and high precision.

The main drawbacks are the difficult removal of the part at the end and the fact that LOM is not well suited for building parts with thin walls.

---

3   Image from: Custompart.net

fig.3 Schematic representation of Laminated Object Manufacturing

1.4 Selective laser sintering

Selective Laser Sintering (SLS) was developed and patented at the University of Texas.
DTM Corporation was established in 1987 to commercialize the SLS technology, and the company shipped its first commercial machine in 1992.

DTM had worldwide exclusive licence to commercialize LS until they were bought over by 3D Systems in 2001.

The basic principle of SLS is hereby described:

1) a thin layer powder is spread by a roller from the powder container to the platform, as shown in **fig.4[4]**.

2) the new powder layer is then selectively sintered by a laser via a scanner

controlled by a computer according to the pattern of the cross section in the CAD model.

Non-sintered powder is left to serve as a support for the following layers.

3) the laser sintered part is obtained by removing the unsintered powder.

This technology has the capability to directly process a variety of thermoplastic, metallic, ceramic materials and thermoplastic composites.

---

4   Image from: ARPTECH, Rapid Prototyping Service

Some great advantages are that no support is needed and overall that little post-processing is required. In facts when a high mechanical strength is not necessary, the completed sintered part out of the machine is already solid enough to be handled.

For ceramic powders, post treatment is often required to densify the microstructure and achieve a high mechanical strength
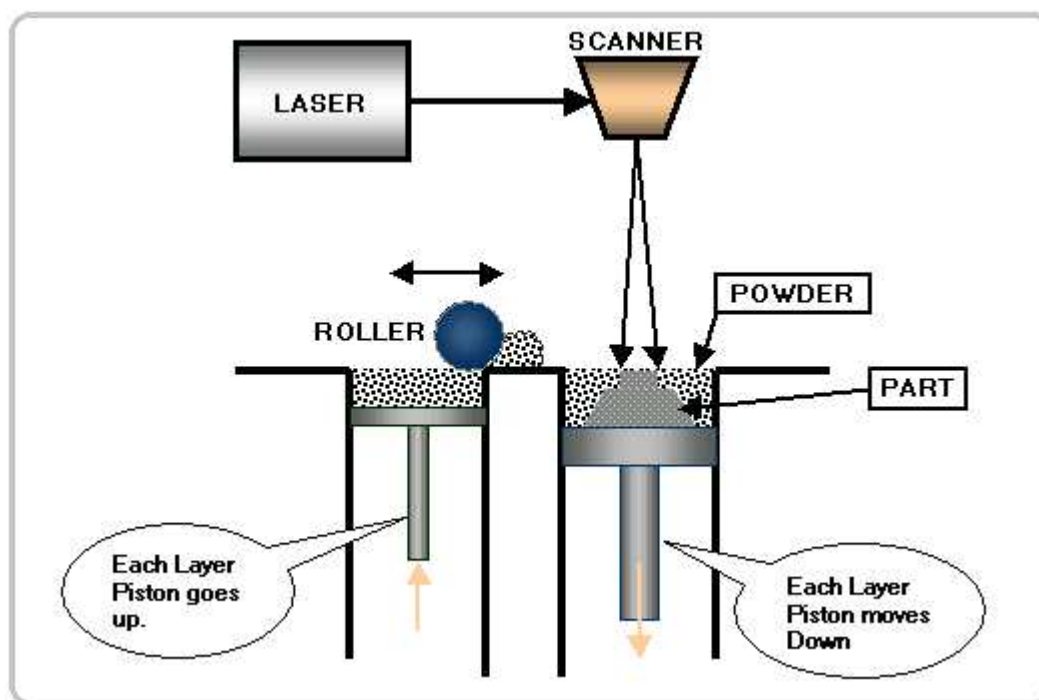
fig.4 Schematic representation of powder bed Selective Laser Sintering

Oxide ceramic powders, such as alumina and silica, have been selectively sintered by ND: YAG-laser (1064 nm) **(13)**. Pure yttria-zirconia powder was also sintered by a fiber laser with a wavelength of 1.064um. But the density and the mechanical properties of the produced samples could not meet the requirement for their potential medical application as dental bridges **(14)**. Lower melting point constitutions, such as metal and organic powder were added into the ceramic powder to lower the sintering temperature and then form composite components.

Polymer derived ceramic parts with complex shapes have been fabricated by selective laser curing (SLC). The ceramic parts were produced by sequentially sintering of SiC loaded polysiloxane powder with a CO_2-laser beam ($\lambda = 10.6$um), which locally induces curing reaction of the polymer phase at moderate temperatures around 400°C. The laser-cured bodies were converted to Si-O-C/SiC ceramic parts in a subsequent pyrolysis treatment at 1200°C in argon atmosphere. A post-infiltration with liquid silicon was carried out in order

to produce dense parts. The bending strength was only 17MPa before infiltration as a result of both micro cracks in the Si-O-C matrix and a pronounced porosity, while an average value of 220MPa was achieved after post-infiltrating with Si **(15)**.

There are different kinds of possible binding mechanisms in SLS **(16)**:

1) *Solid state sintering* is a thermal process that occurs at temperatures between $T_{Melt}/2$ and T_{Melt}, where T_{Melt} is the melting temperature of the material. Various physical and chemical reactions occur, the most important being diffusion. It involves neck formation between adjacent powder particles. The main driving force for sintering is the lowering of the free energy when particles grow together A gradient in vacancy concentration between the highly curved neck (high vacancy concentration) and the 'flat' surfaces (low vacancy concentration) causes a flux of vacancies from the neck and a flux of atoms towards the neck thus increasing the neck size.

2) *Liquid phase sintering*:

- Different binder and structural materials: a specific low-melting material is added to the structural powder material. The binder may be another mixed powder or a coating or in other forms. The final morphology consists in the structural particles connected by the binder that was melted.
- No distinct binder and structural material. The material may be single or multi-phase, and rather than the distinction between binder and structural material, there is a distinction between molten and non-molten material areas. Therefore 'Partial Melting' is a better name for these technologies.

3) Full Melting permits to achieve full dense structure, with mechanical properties comparable to those of bulk materials and possibly to avoid lengthy post processing cycles. However for each new material, a process-window needs to be determined experimentally, in order to ovoid scan track instabilities (sphereodisation of the liquid melt pool, also known as 'balling'), porosity and cracks.

Liquid phases promote the sintering velocity and are therefore predestinated for short sintering times as they occur during laser sintering of ceramics.
Under a short laser-irradiation of the powder bed, the particle bonding and sintering must be rapid and thus solid-phase sintering, which requires a long diffusion time, does not seem

to be feasible in selective laser sintering.

Y.Wu and al. for example described the sintering process of an alumina powder bed **(17)**.

In practice, laser sintering of alumina powder beds may be considered in three stages:

(1) initial sintering up to a eutectic formation of liquid-phase. The eutectic phase systems result from the impurities in the starting alumina powder

(2) liquid-phase sintering allowing the liquid-phase to spread

(3) liquid–solid phase bonding and sintering during the period of cooling after laser irradiation.

J.Heinrich, Gahler and al. **(18)** demonstrated that liquid phase sintering can be achieved in a system composed of Al_2O_3 and SiO_2 powders, and studied the microstructure evolution. The ceramic powder was sintered without the use of any organic or metallic binder.

A siliceous melt is formed within a few seconds, which incorporates Al_2O_3 by subsequent dissolution of the starting alumina.

Despite of the short laser time, as soon as a critical Al_2O_3 concentration is reached, mullite nucleates within the bulk of the melt. The dissolution-precipitation process typical

for reaction sintering of mullite and subsequent unhindered grain growth leads to mullite needles.

With the aim of increasing the density of the green layers, in the last years different methods have been proposed instead of the classic roll-spreading of the powder bed.

In this way sintering is more activated and the densities of the green bodies as well as the post sintered ceramic bodies are higher than the traditional SLS process.

One method is the spraying of a ceramic slurry, used for example by A.Waetjen et al **(19)**.

The laser sintering process using layer-wise slurry deposition has been investigated only by Günster et al. and Gahler et al. **(20,21)**

This process is called Layerwise Slurry Deposition: basically instead of a ceramic powder, a ceramic slurry is deposited by a doctor blade.

The sequence of operations is represented in **fig.5[5]** and can be listed as:

---

5   Image from: Fabrication process of ceramic components by using Layer-wise Slurry Deposition
and direct laser sintering (Gahler et al., 2006)

(1) slurry deposition of a layer

(2) drying, to obtain a ceramic tape

(3) laser sintering of the object's cross section

(4) repeat (1) to (3) until all the hight of the sample is built

(5) cleaning with water

(6) post sintering (if needed)
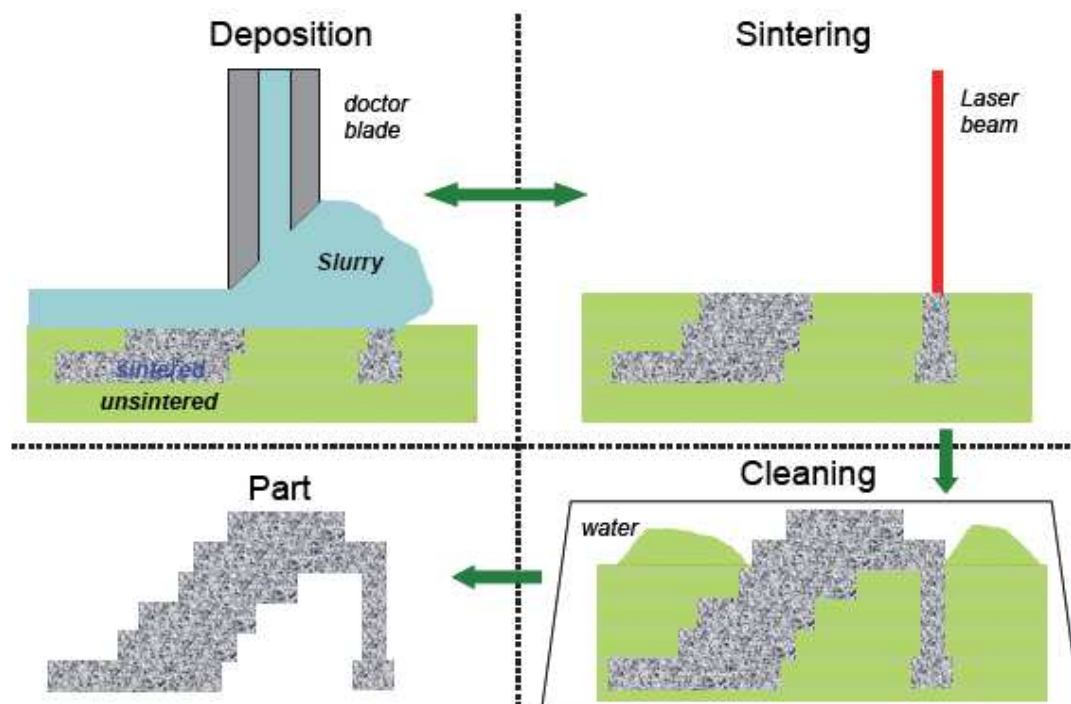
fig.5 Schematic representation of Laser Sintering of Layerwise Slurry Deposition

The cleaning step is usually quite easy, since it is enough to dip the green body containing the part in an ultrasonic bath, and the non-sintered powder will simply dissolve.

This step however may take a short (minutes) to long time (hours or even days), depending on the material and the complexity of the shape.

The process time itself instead is up to 5 minutes per layer; since each layer is usually 100 μm thick, this corresponds to up to 8 hrs each 1cm.

Many samples can be built at the same time, reducing the process time per single part.

As said the main advantage of this process is that a high green density, up to 70%, can be achieved.

The main drawback is that for every different material, a different slurry has to be prepared and optimized, limiting the versatility.

Fig.6 shows the specific technology used in Clausthal, with a silica slurry:

- the first layer is deposited by the doctor blade (**fig.6a**)
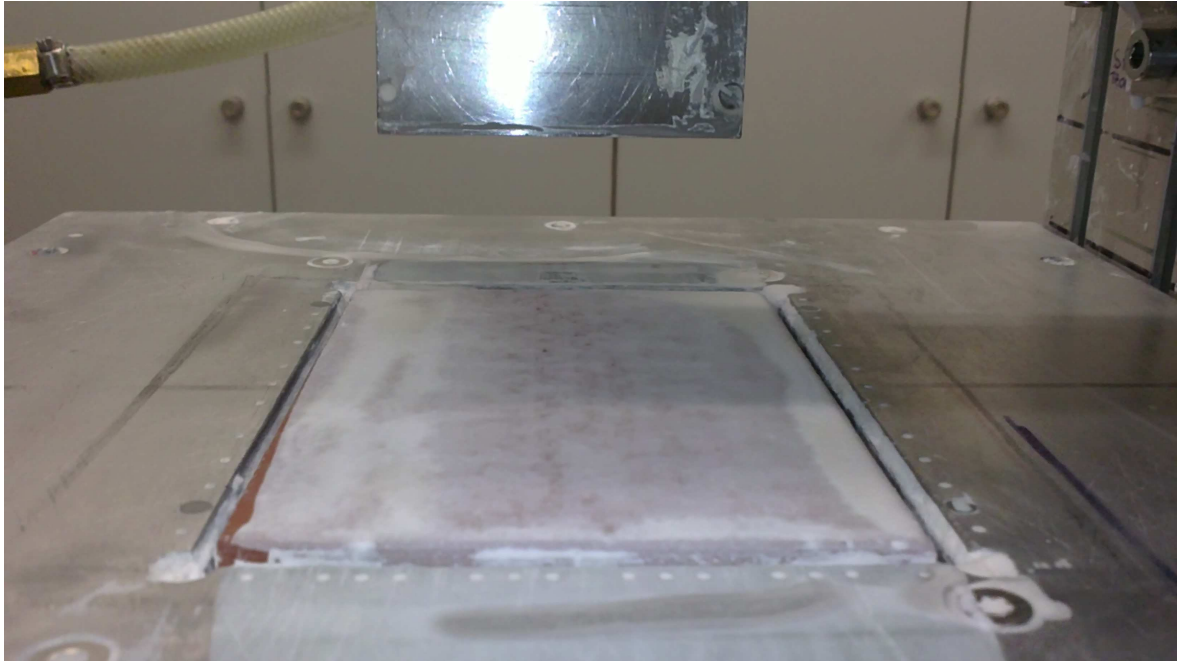
fig.6a Deposition of the first pre-layer by doctor blade

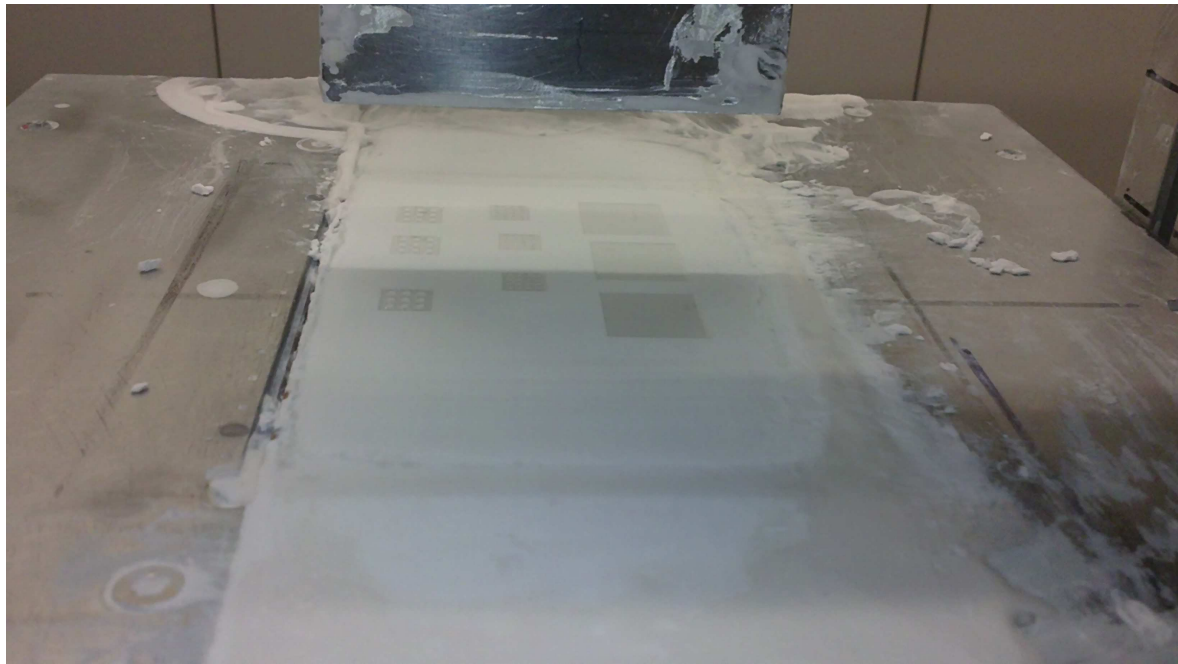- drying of the layer (**fig.6b**). This operation may be accelerated heating the tile up to 200°C.

Ten pre-layers are deposited to guarantee a perfect base, before the laser starts
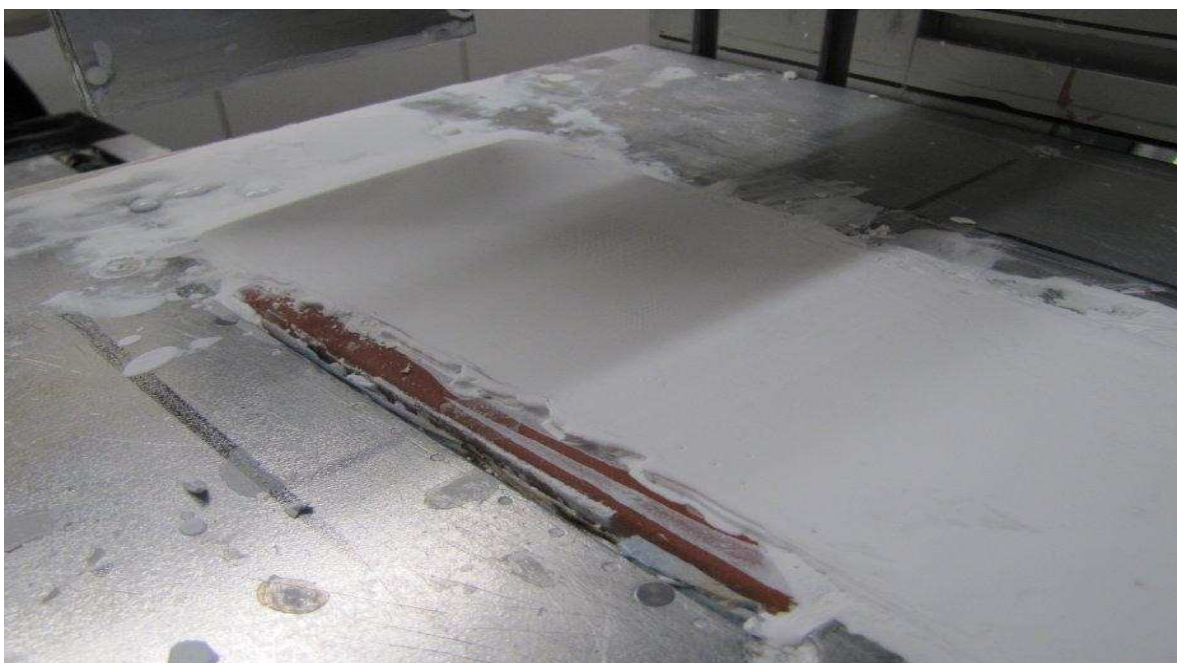
fig.6b Ten pre-layers deposited and dried

- the laser sinters the cross section of the object (**fig.6c**)

fig.6c The first layer after laser sintering

- a new layer is deposited, dried, sintered and so on (**fig.6d**)

fig.6d Laser sintering of a new layer

- the green layers are removed from the tile and the samples are washed in a water-based solution (**fig.6e**)
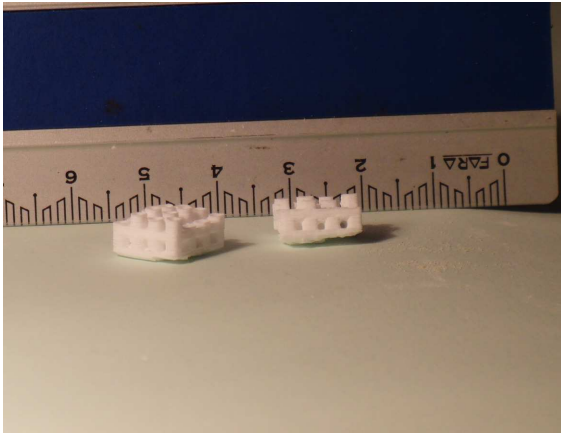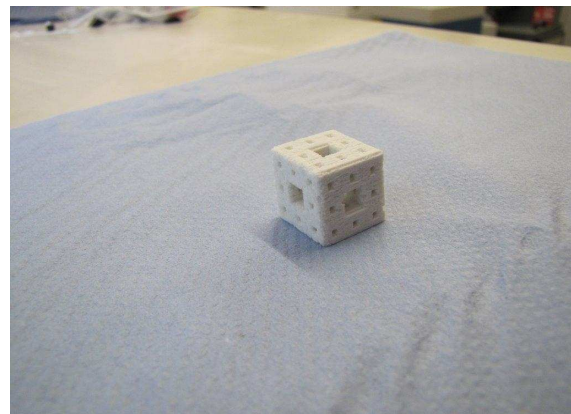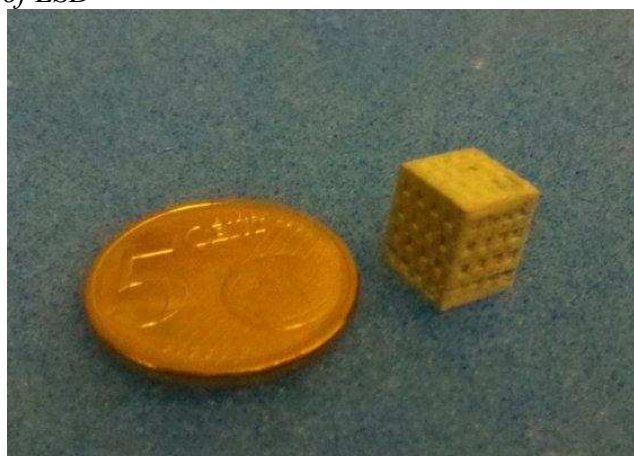

fig.6e Samples after cleaning
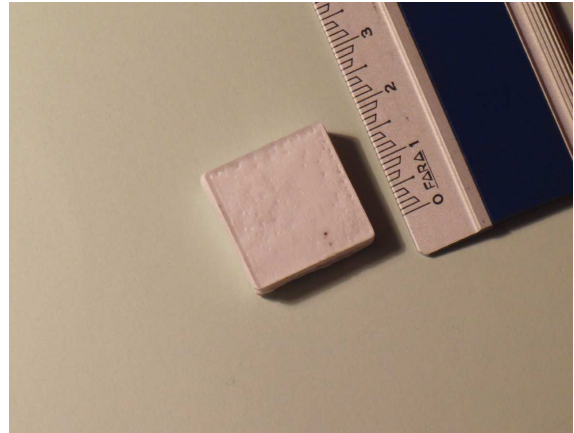
Some state-of-art objects produced in Clausthal[6] with a porcelain commercial slurry are displayed in **fig.7a,b.** A 3D scaffold was produced with this slurry as a proof of concept (**fig.7c**).
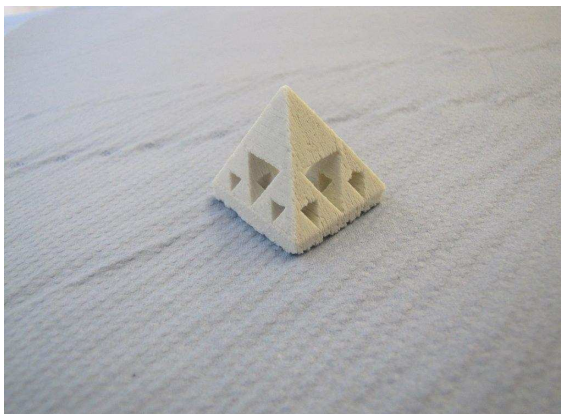
fig.7a State-of-art porcelain products by SLS of LSD

fig.7b

fig.7c porcelain scaffold produced by SLS of LSD

6 Thomas Mühler, LaserAnwendungsCentrum, Clausthal TU

20

1.5 3D printing

Powder based three-dimensional printing was developed at Massachusetts Institute of Technology, USA in 1992 as a method to create preforms from powdered metals and ceramics **(22)**.

The method can be described like this:

(1) An individual two-dimensional layer is created by adding a layer of powder to the top of a piston and cylinder which contain a powder bed and the part being fabricated.

(2) A new layer of the being built component is to be formed by "ink-jet" printing of a binder material.

(3) Then, the piston, powder bed and part are lowered and new a layer of powder is spread out and selectively joined. This layering process is repeated until the part is completely printed.

(4) After removing the unbound powder with a simple air flow, a heat treatment process follows to densify the fabricated part.

A schematic representation of a 3D system is in **fig.8**.
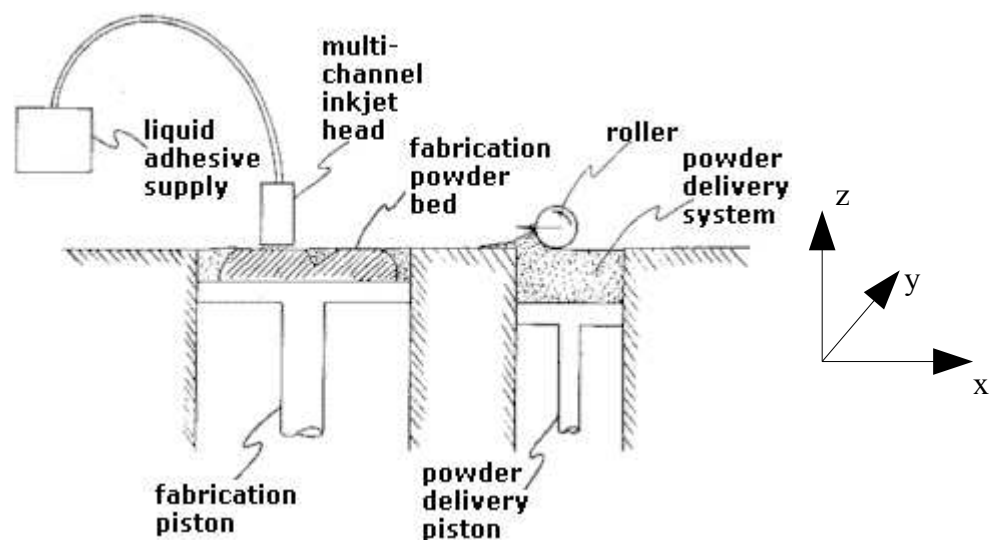
fig.8 schematic representation of powder based 3D printing

In the system used at BAM in Berlin with a ceramic powder, between step (3) and (4) there is a heating time, while the sample bed is moved to a heating zone to cure the polymer.

At the end, the cleaned sample was treated in an oven at 125°C for one night to complete the cure. After that, the binder is burned at 300-400°C for 1h and the ceramic powder is

sintered, with the standard sintering treatment for the specific material.

A picture of the machine used is showed in **fig.9** where the most important components are indicated.

A great advantage of this technique is that it is very easy to use, versatile, and even very complex shapes are easy to print.

Clearly, there is some requirement for the powder dimension and morphology, because a good flowability has to be achieved in order to have a good layer spreading; but besides that, almost every powdered material can be used.

Since a low temperature is involved in the process, also low-melting point materials can be used, for example the pre-ceramic polymers. The sintering step is out of the machine, so it can be easily controlled.

On another point of view this is a drawback, because usually a long post treatment is needed, compared for example to selective laser sintering.

The process itself however is pretty quick: depending mainly on the section area, a layer can be printed in 3-5 minutes.

Another drawback is that usually the accuracy and the surface finish are worse compared to other techniques, depending on the particle size and the binder absorption.

It is not possible to obtain fully densified objects, both for the presence of the binder that is later burned, and also because the green density is low, due to the fact that the powder is not pressed during the rolling.

The porosity may be a disadvantage, but it may also be useful, for example for bone implants.
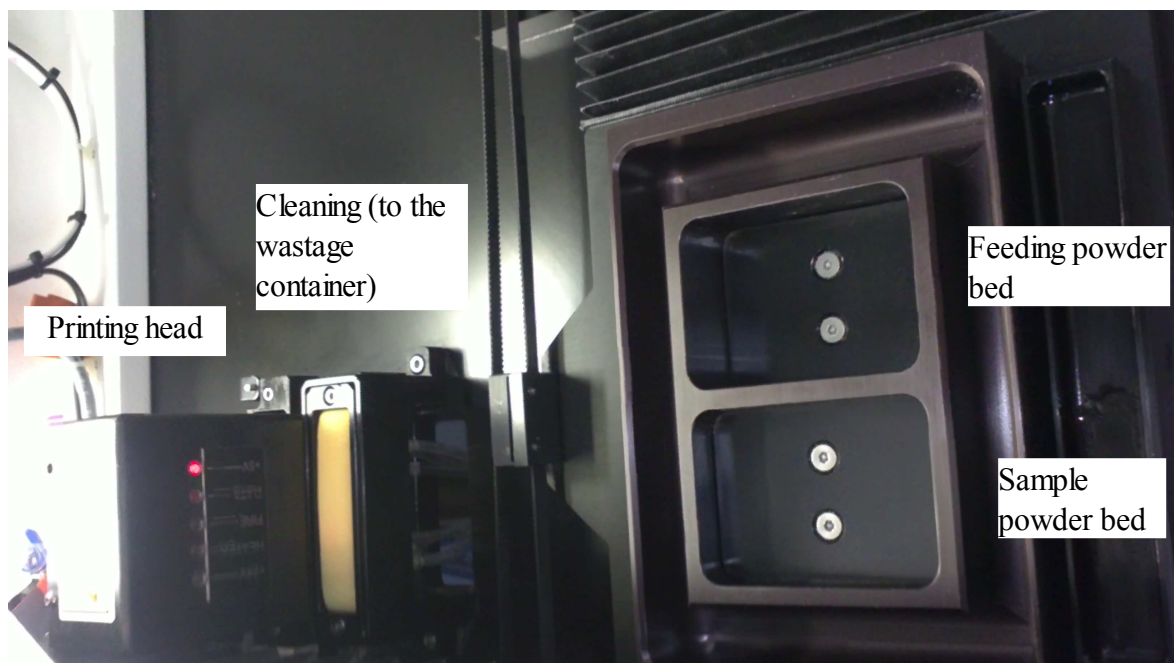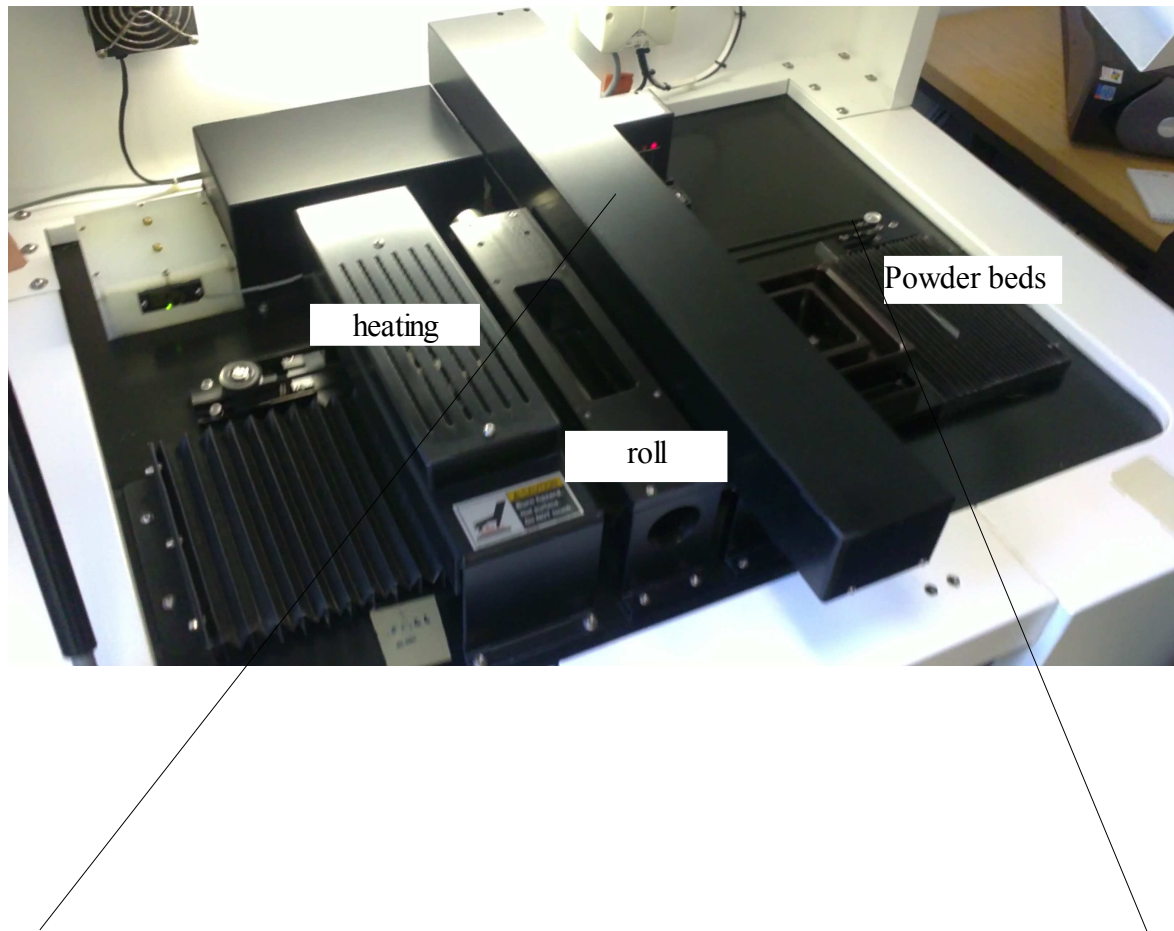
fig.9 The 3D printing machine used at BAM, a Prometal RX Series (Germany)

1.6 Choice of the materials

Different materials were used for the experiments:

- silica was used for selective laser sintering of layerwise slurry deposition.

Silica has outstanding thermal properties, especially a low thermal expansion coefficient. This makes the material a good choice for laser treatment, because that causes high temperature gradients that may lead to distortion.

Moreover amorphous silica is transparent, and the final product might be transparent as well at least when completely dense.

Based on A.Gahler Ph.D. work **(21,23)** a silica slurry was optimized and 3D parts were produced.

Silica powder characterization is in section 2.2.2 and slurry optimization can be found in section 3.1.4.

The choice of laser parameters is in section 3.3.1.1; finally 3D scaffolds have been produced by SLS and they are characterized in section 3.4.2.

- LAS glass ceramic was studied for selective laser sintering as well. The composition used crystallizes to lithium silicate and beta-spodumene, that is famous to have a very low coefficient of thermal expansion.

Thus also this powder is interesting for lasers applications, and for producing samples with high thermal stability **(24)**.

LAS powder is characterized in section 2.3.2, the preparation and optimization of the slurry is described in section 3.1.5 and finally a laser parameters analysis is carried out in section 3.3.1.3.

Since the process parameters still have to be improved with this material, it was not possible to complete any 3D part.

However 3D scaffolds have been actually produced with this powder, using 3D printing; the final samples are shown and studied in CHAP 4.

- Pre-ceramic polymer powders were prepared at Padova University.

Even if they haven't been used at the end, these materials have attractive properties both for laser sintering and 3D printing.

In facts, the polymers can be either laser-cured and converted to ceramic **(15)**, or printed as

a powder and ceramized with a post oven treatment.

There might be also another option, that is dissolving the polymers in a solvent to produce a low viscosity liquid for ink-jet printing **(25)**.

For this work of thesis, one pre-ceramic is formulated to produce mullite, the other to give rise to wollastonite, that is known to have a good biocompatibility and often used together with hydroxyapatite **(26)**.

Since these materials are so interesting for possible applications with Rapid Prototyping, hopefully they will be used for further studies in the future.

More information about the materials and their preparation can be found in the next chapter.

CHAP 2: MATERIALS PROPERTIES AND PREPARATION

In this section follows a brief presentation and a description of the preparation of the materials used in the experimental part.

Since the particle size has a strong influence on both 3D printing and LSD, all the measured distributions are reported, and all the comments in the following chapters are referred to these data.

2.1 Pre-ceramic polymers

2.1.1 Overview

Pre-ceramic polymers are special polymers that after pyrolysis produce a ceramic product with high yield.

In particular polysiloxanes are well known to give a ceramic residual that in inert atmosphere is composed of SiOC (amorphous silica where part of Si is replaced with C) and SiC, while in oxidizing atmosphere it is composed only of SiO_2, because all the carbon is burned **(27)**.

For these experiments it was used a pre-ceramic polymer with commercial name MK.

MK is a poly(methylsilsesquioxane) with the structure shown in **fig.10** besides a 2% mol hydroxyl and ethoxyl groups as functional units **(28).**

At room temperature it is a white powder with a Tg of 45-60°C.

The SiO_2 yield is about 84% wt, while the remaining is lost with the gas release (mostly CO_2) during the decomposition.

fig.10 basic structure of MK polymer
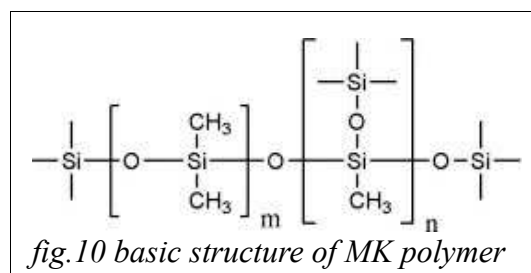
These materials are interesting because they can be formed with the common polymer techniques and only later ceramized.

The use of the polymer alone is however limited both by the shrinkage and the gas release, that seriously damage the shape and the integrity of the product.

For this reason different fillers have been developed, some metallic that react with the gas, other that are inert and used only to lower the transforming phase content, other that react with the ceramic residual.

Adding different types of oxide in the right amounts, it is possible to obtain different crystalline phases.

For this thesis alumina and calcium carbonate were used, the former to produce mullite **(29)** and the latter to produce wollastonite **(27)**.

Wollastonite in particular is known as a bioactive material, often used together with hydoxyapatite.

Mullite

Mullite is an aluminosilicate of approximate composition $3Al_2O_3 \cdot SiO_2$, often used as refractory material but quite difficult to produce and sinter.

The synthesis from pre-ceramic materials is then particularly interesting, because it permits an easy formability, an a rather low treatment temperature (1350°C).

The molar ratio of the two oxides is $Al_2O_3/SiO_2 = 1.5$, and the weight ratio is then 2.55.

Calculating that from each gram of MK 0.84g of SiO_2 result, the weight ratio should be $Al_2O_3/MK = 2.14$.

Actually, as can be seen in a binary diagram silica-alumina (**fig.11**), mullite is not a stoichiometric compound, but it has a certain range, so a slightly higher amount of alumina can be used.

In this way it is less likely that some silica can form crystallites during the oven treatment.

Cristobalite is highly undesired because it has a phase transformation with a volume change that easily causes cracking in the sample.

In order to have a complete reaction between silica (from the polymer) and alumina (the filler) the mixture should be homogeneous.

For this reason the MK is dissolved in an organic solvent (acetone or isopropilic alcohol), then the alumina is added slowly, always maintaining the liquid stirred and being careful to avoid any precipitation.

An alumina nano-powder with a mean size of 15 nm was used.

The solvent is then evaporated at 60°C for one night and the material is milled.

The standard heating treatment to obtain mullite is 1h at 1350°C, with a heating rate of 10°C/min.
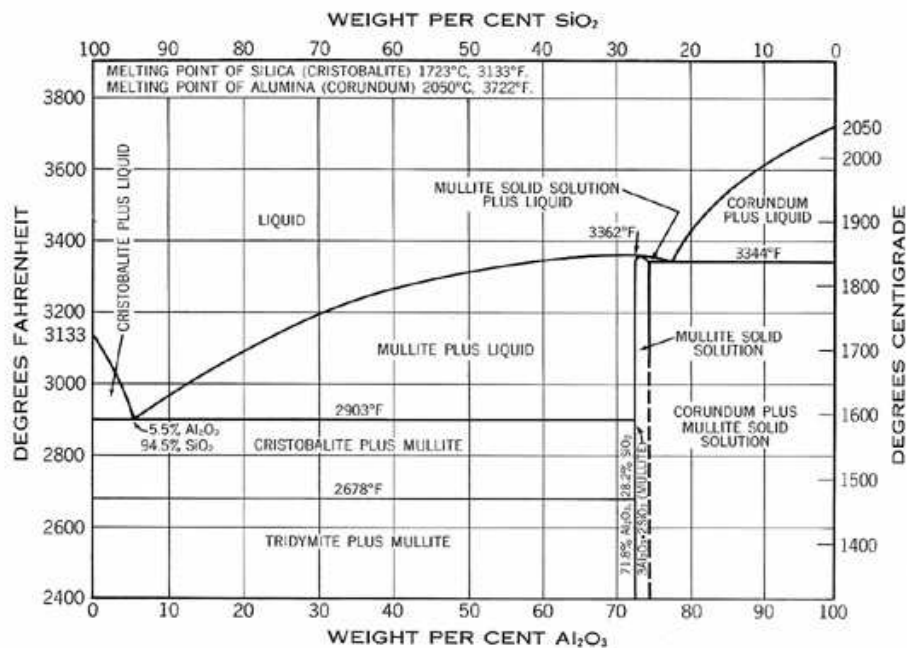
fig.11 Phase diagram Alumina-Silica

Wollastonite

Wollastonite is a calcium inosilicate, with the chemical composition $CaSiO_3$, that is CaO-SiO_2 (CS).

It can be obtained for reaction of silica with different calcium compounds; in particular with calcium carbonate the reaction is as follows:

$CaCO_3 + SiO_2 \rightarrow CaSiO_3 + CO_2$
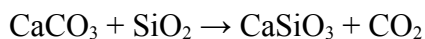
The pre-ceramic powder is prepared in the same way of the mullite, but in this case the carbonate powder is micrometric.

The heating treatment is 1h at 900°C with a heating rate of 10°C/min.

Using a micrometric powder it is more difficult obtain a good mixing of the calcium carbonate with the polymer; so, likely, there are zones with a higher concentration of CaO, where $2(CaO)$-SiO_2 (C_2S) is produced instead than CS, and other zones where some unreacted silica remains.

Thus it is still important to control that cristobalite is not produced, as already explained.

2.1.2 Synthesis and characterization

The mass ratios $Al_2O_3/MK=2.14$ and $CaCO_3/MK=1.4$ have been calculated from the ceramic yields.

The standard procedure to mix MK and the powder (Al_2O_3 or $CaCO_3$) is to dissolve the polymer in acetone or isopropanol and then add, while stirring, 1g of solid each 10cc of solvent (10%).

In this way the suspension is quite diluted and remains stable easily, but also few product is obtained. In order to produce more material in a single step, the possibility of using a more concentrated solution was studied.

Firstly, a standard concentration of 10% was used for comparison, then an attempt with a 30% concentration was done for calcium carbonate and 20% for alumina.

The four suspensions (two standard and two concentrated) were dyed at 60°C and milled. The powder particle size distribution after milling is reported in **tab.1**

Under (%)	D10 (µm)	D50 (µm)	D90 (µm)	D97 (µm)
Pre-Al_2O_3	1.42	12.26	71.33	52.72

tab.1 Particle size distribution of the milled pre-ceramic polymer containing Al_2O_3

The powder was finally put in the oven, 1h at 1350°C for mullite and 1h at 900°C for wollastonite.

The samples were analyzed by XRD (D8 advance by Brucker) in the range 10-60° and a 0.05° step.
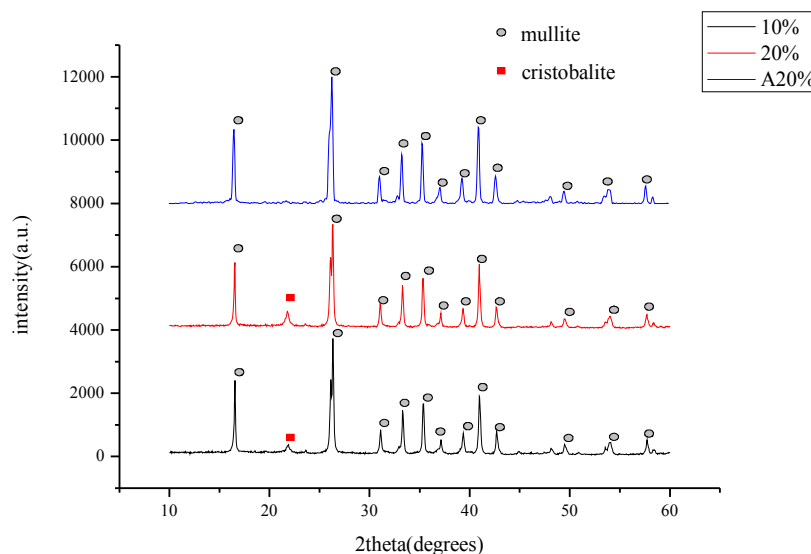
Mullite

The diffractograms measured for mullite are plotted in **fig.12**.

It is clear that the main phase is mullite, and the results are similar for the samples at concentration 10% and 20% (black and red line respectively).

Nevertheless there is a peak that marks the presence of some cristobalite, and this peak is more evident in the sample at 20%.

This happens because in the latter case the distribution of alumina is less homogeneous

Therefore, another attempt was done with the same concentration 20% but with a slightly different composition.

fig.12 Diffractograms of mullite samples from Al₂O₃ filled pre-ceramic, for different concentrations of the starting solution

Al$_2$O$_3$ was increased from 60% to 63% (mol), that is the maximum value in the mullite range.

The diffractogram for this new powder is in the same graph, it is the blue line called A20%. The cristobalite peak is almost disappeared, so this composition was found to be suitable.

Wollastonite

The powder particle size distribution of the pre-ceramic powder (before ceramization) after milling is reported in **tab.2**

Under (%)	D10 (μm)	D50 (μm)	D90 (μm)	D97 (μm)
Pre-CaCO$_3$	5.02	51.07	225.63	335.82

tab.2 Particle size distribution of the milled pre-ceramic polymer containing CaCO₃

The diffractograms obtained for the powder with calcium carbonate are plotted in **fig.13**. Wollastonite is actually the main phase, but there is some larnite (C$_2$S) as a secondary phase; this was expected because a micrometric powder was used.

Since there is no cristobalite in neither one of the two diffractograms and the two graphs are similar, the conclusion is that a concentration of 30% can be used.
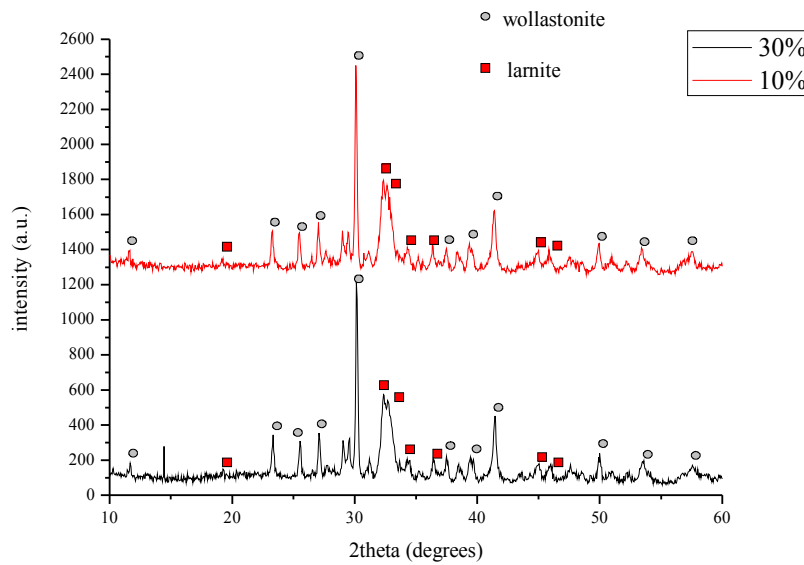
fig.13 Diffractograms of wollastonite samples from CaCO₃ filled pre-ceramic, for different concentrations of the starting solution

2.2 Silica

2.2.1 Overview

Amorphous silica exhibits very interesting properties, some of them are summed up in **tab.3** [7], compared to a soda-lime glass.

First of all the low thermal expansion coefficient (α), transparency (when dense) and good chemical inertness make this material used in many applications, such as temperature insensitive optical components supports, lenses and mirrors in highly variable temperature regimes.

Silica has a high resistance to thermal shock, a property that is often characterized for ceramics with a thermal shock parameter (TSP):

[1] $$TSP = \frac{\lambda \sigma (1-\nu)}{\alpha E}$$

---

7   Data from: Granta Design CES edupack 2010

where λ= thermal conductivity

σ= tensile strength

ν= Poisson coefficient

α= thermal expansion coefficient

E= Young modulus

For comparison [2] $\dfrac{TSP_{silica}}{TSP_{sodalime}} \simeq 60$

	E (GPa)	λ (W/mK)	α (10^{-6}/K)	σ (MPa)
Silica	68-74	1,4-1,5	0,55-0,75	45-155
Soda-lime	68-72	0,7-1,3	9,1-9,5	31-35

tab.3 some properties of Silica and Soda-lime glass

As just shown, silica can resist much more than soda-lime to a laser treatment, that always causes high and quick temperature variations.

2.2.2 Characterization

Two different powders were used for the silica slurry preparation:

Nano-silica:

This powder (SiO2-HDK from Wacker, Germany) was analyzed with a Ultraschallspektrometer DT1200 to determine the particle size and the zeta potential in a 4% water suspension.

A D50 of 36 nm was measured and a zeta-potential of -14mV (distribution in **fig.14**)
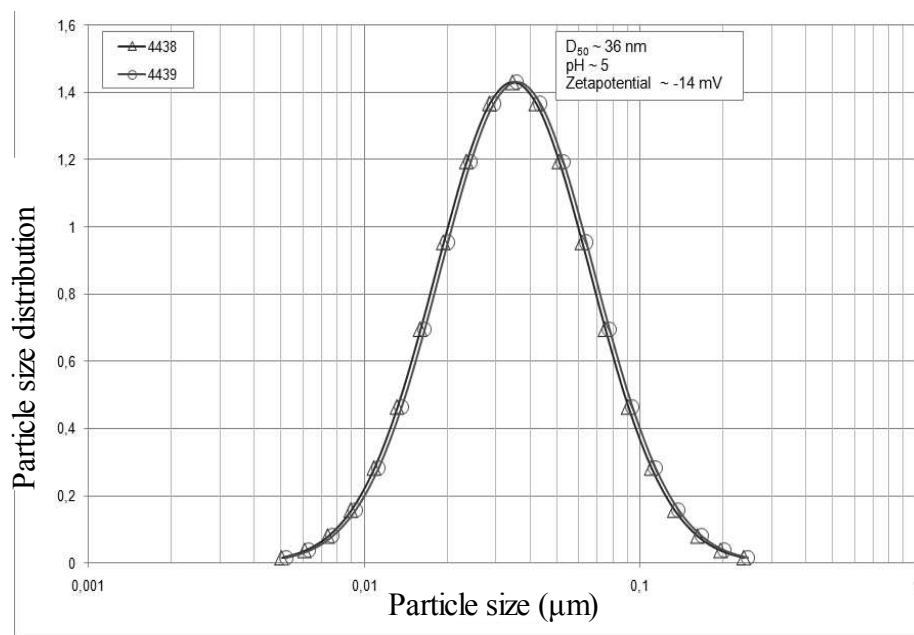
fig.14 particle size distribution and zeta-potential of the nano-silica

Fig.15a and **fig.15b** show SEM pictures of the powder, where the particles are spherical and the nano-size is confirmed, but it's also clear that the powder is agglomerated up to 5 µm.
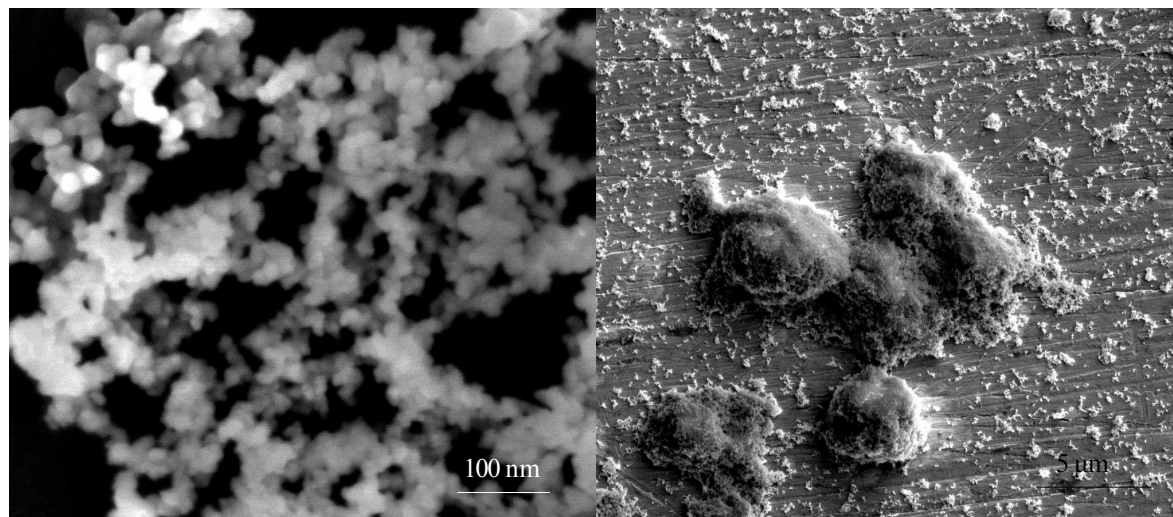
| *fig.15a SEM picture of the silica nano-particles* | *fig.15b SEM picture showing the nano-silica agglomerates* |

The specific surface of the nano-silica is 204 m^2/g.

Fused Silica

This powder is a spherical coarse silica, fused at Waker, Germany, as can be seen in **fig.16a** and **fig.16b**
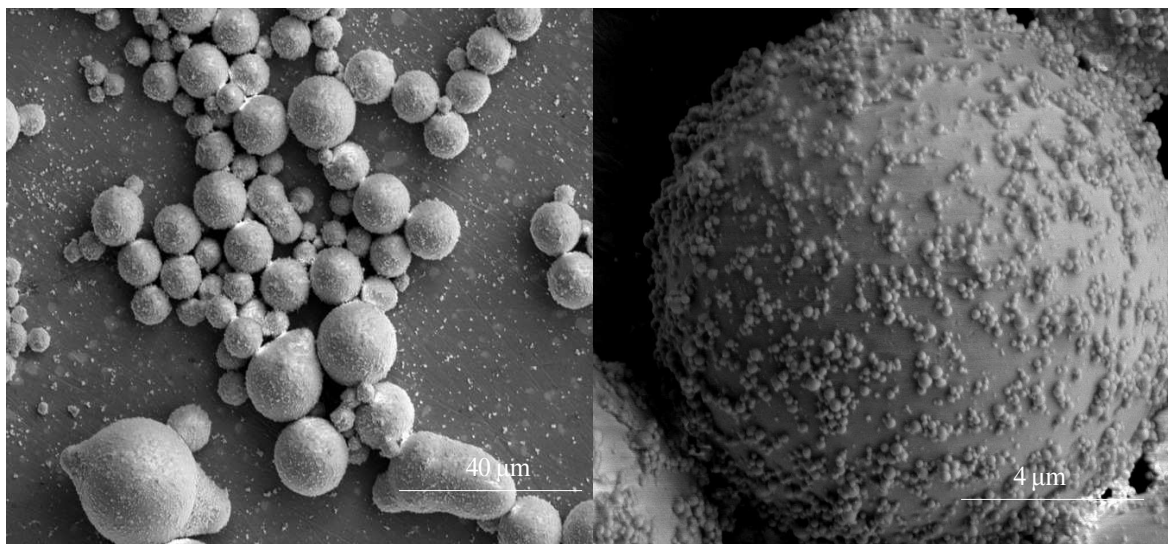
fig.16a SEM picture of the spherical micro-silica   *fig.16b SEM picture of a single micro-silica particle*

The particle size distribution is reported in **tab.4**

Under (%)	D10 (µm)	D50 (µm)	D90 (µm)	D97 (µm)
Silica	5.97	16.94	38.83	52.72

Tab.4 particle size distribution of the micro-silica

The silica powder is amorphous, the diffractogram is shown in **fig.17**
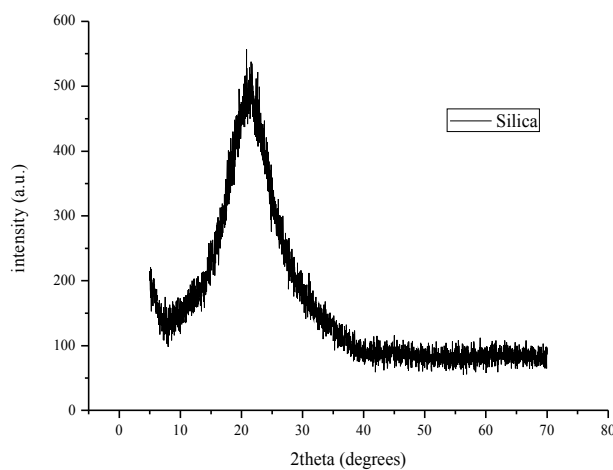
fig.17 diffractogram of the amorphous silica

2.3 LAS Glass-ceramic

2.3.1 Overview

Glass ceramic are well known to combine properties of glass and ceramics to obtain characteristics that differ from every other material.

Crystallization of the parent glass usually improves the strength and the fracture toughness, while the optical properties may vary from translucent to complete opaque, depending on type, dimension and content of the crystalline phase.

$Li_2O-Al_2O_3-SiO_2$ systems have been widely studied also for the possibility to obtain after crystallization a low value for α, thanks to the nearly zero or even negative coefficient of thermal expansion of the crystalline phase.

There are mainly two LAS groups:

- − solid solutions of β-eucryptite ($LiAlSiO_4$) and silica with the structure of β-quartz, called also β-quartz solid solutions (ss)
- − solid solutions of β-spodumene ($Li_2O-Al_2O_3-4SiO_2$) with the structure of keatite, that is a metastable tetragonal form of SiO_2.

Usually, to produce a glass-ceramic, a nucleating agent as TiO_2 or ZrO_2 is added to the parent glass composition **(30)**.

Firstly the glass is formed to the desired shape with the normal glass technologies; lately the sample is heated and internal nucleated, until finally the crystals grow on the previous nuclei.

In recent years, another method of manufacture has been proven viable.

The manufacture of glass-ceramics from powdered glass, using conventional ceramic processes such as spraying, slip-casting, or extrusion, extends the range of possible glass-ceramic compositions by taking advantage of surface crystallization. In these materials, the surfaces of the glass grains serve as the nucleating sites for the crystal phases. The glass composition and processing conditions are chosen such that the glass softens prior to crystallization and undergoes viscous sintering to full density just before the crystallization process is completed. Given these conditions, the crystalline microstructure is essentially the same as that produced from the bulk process.

The precursor glass powders may be produced by various methods, the simplest being the milling of quenched glass to an average particle size of 3–15mm.

Applications include multilayer substrates for electronic packaging, matrices for fiber

reinforced composite materials, refractory cements and corrosion resistant coatings, honeycomb structures in heat exchangers and bone and dental implants and prostheses. These products take advantage of the complete densification, thermal stability, and wide range of physical properties possible in glass-ceramic systems, and provide a number of advantages over conventional glass frits.

2.3.2 Characterization

The LAS powder utilized in this thesis was supplied by Colorobbia S.p.a. (Firenze, Italy). It is a composition in the β-spodumene solid solutions, milled from the glass frit.

The coefficient of thermal expansion of the glass is $8 \cdot 10^{-6}$, and $6.5 \cdot 10^{-6}$ after crystallization. Four different particle sizes were grinded, two for LSD and two for 3D printing; the relative data are reported in **tab.5** and **tab.6**

LSD

Under (%)	D10 (µm)	D50 (µm)	Mean (µm)	D90 (µm)	D97 (µm)
LAS1	1.16	4.41	5.94	13.43	17.18
LAS2	0.99	5.08	8.94	22.94	33.01

tab.5 particle size distribution of the powders used for LSD

3D printing

Under (%)	D10 (µm)	D50 (µm)	D90 (µm)	D97 (µm)
LAS3	4.43	75.52	157.13	199.14
LAS4	112.68	223.05	367.73	440.15

tab.6 particle size distribution of the powders used for 3D printing

All these powders are amorphous except for LAS1, which was pre-crystallized.

XRD graphs for LAS1 and LAS2 are in **fig.18**, where is confirmed for LAS1 that the main crystal phase is spodumene, and there is some lithium silicate as secondary phase.
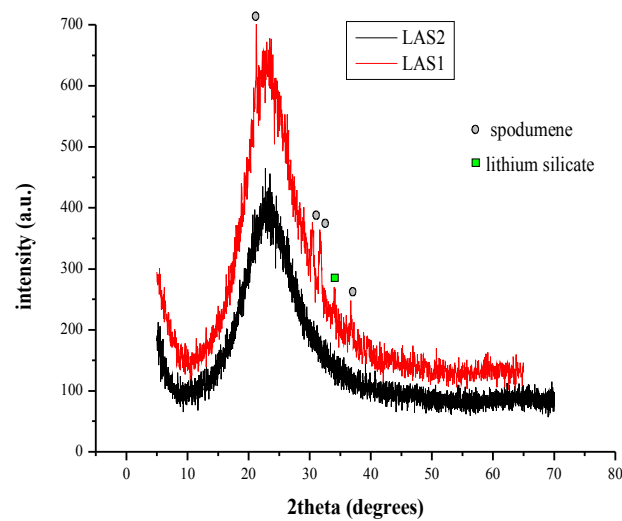
fig.18 diffractogram for LAS1 (pre-crystallized) and LAS2 (amorphous) powders

In this case however the spodumene is in the low temperature α-phase, that is monocline, while the β-spodumene is tetragonal.

LAS2 powder was also analysed with a EMI hot stage microscope (Hesse Instruments, Osterode, Germany) to determine the sintering temperature.

In **fig.19** are plotted the variations of geometrical parameters of a cubic sample, pictured in **fig.20**, when heated.

Four main points are recognized:

1) sintering temperature: this is not really a single point, but an interval in which the particles sinter; in this period the volume decreases (and so the measured area) but the shape of the sample does not change (the shape factor is constant).
   As can be noticed there's a first slow decrease starting from 500°C, but the sintering temperature can be considered to be around 860 °C (picture 4)

2) glass temperature: when this value is reached, the angles at the corner of the square start to round off and the shape factor increases.
   For this material Tg is about 933°C.

3) Sphere temperature is 951°C

4) Half sphere temperature is 968°C
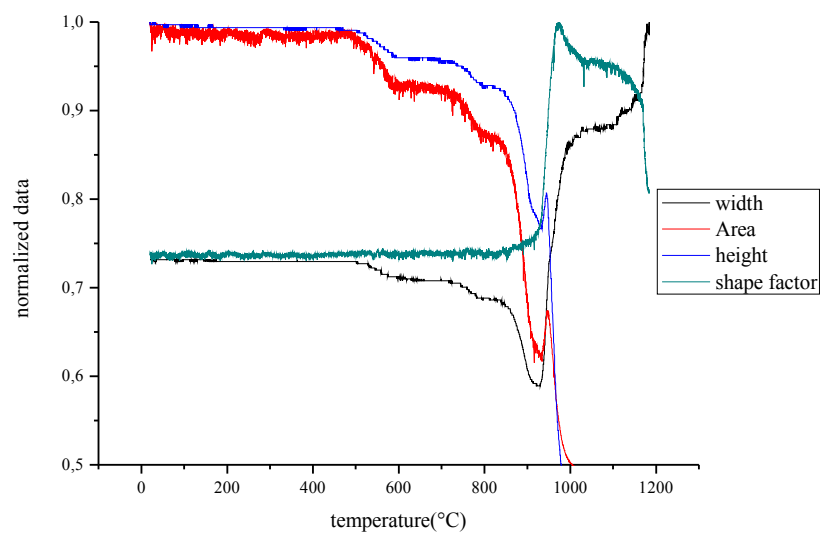
fig.19 variation of geometrical parameters with temperature
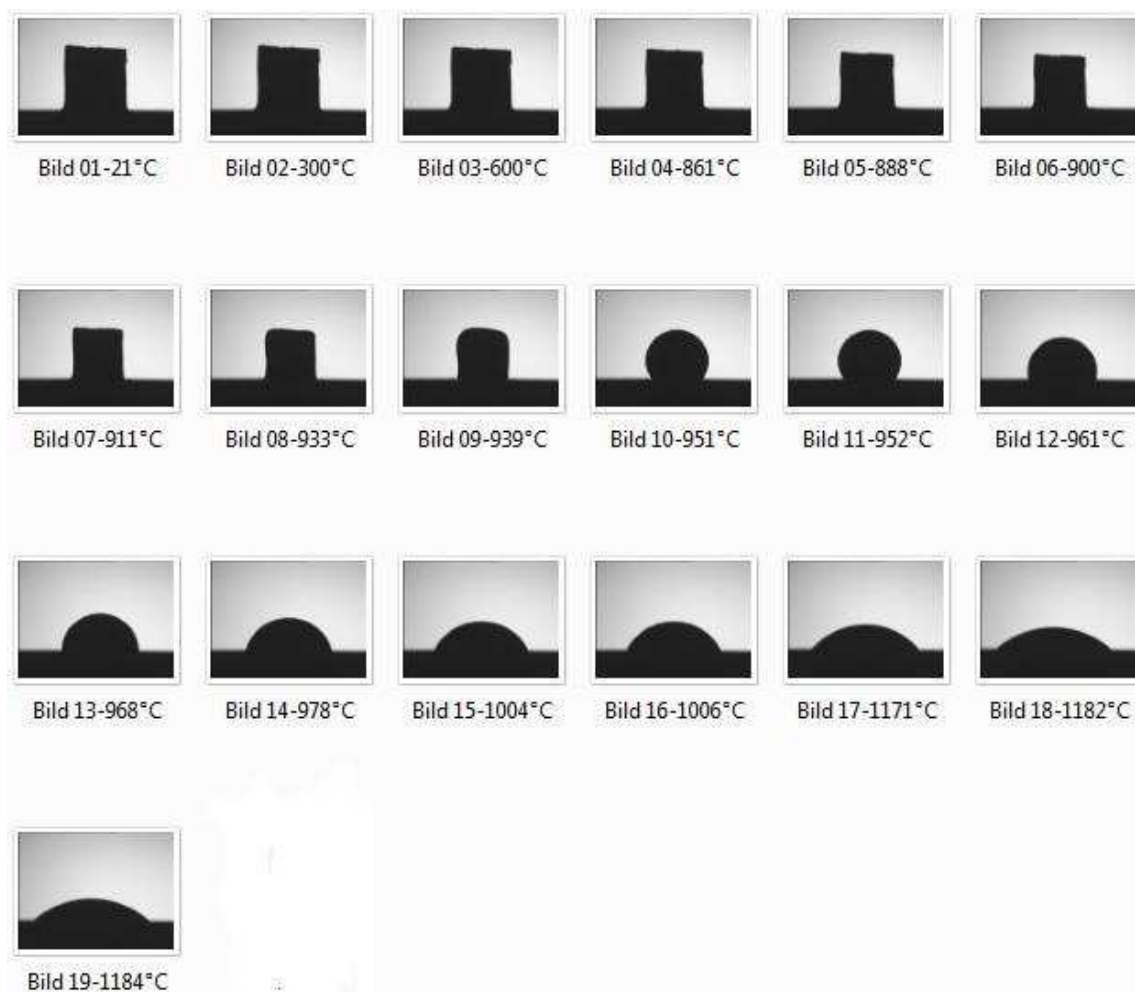
fig.20 picture of an LAS sample under the heating microscope

CHAP 3: LASER SINTERING OF LAYERWISE SLURRY DEPOSITION (LSD)

F.Klocke et al. **(31)** proposed all the steps that have to be studied in a laser sintering layers from ceramic slurries (**fig.21**). This process is based on a spray-drying deposition, but can be easily extended to a doctor-blade deposition.
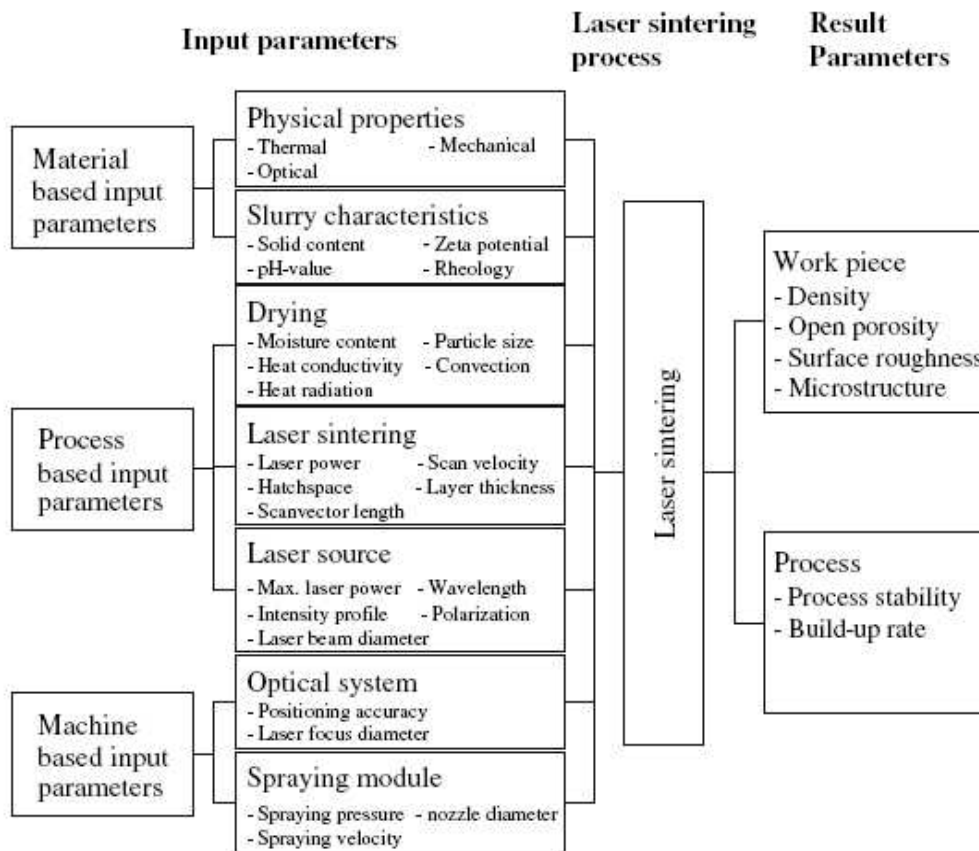
fig.21 influence on laser sintering of ceramic slurries, proposed by Klocke et at.

This general pattern was basically followed in the experiments with silica and LAS: first, a study of the slurry, then the laser parameters and finally the samples characterization.

3.1 Slurries preparation and characterization

3.1.1 Overview

Finding a suitable slurry composition is of great importance in order to achieve a stable

and defects-free tape from the deposition process.

In particular two are the main properties to control:

1) stability is clearly necessary to avoid the precipitation of the powder, which subsequently leads to either a rough layer surface, because of the agglomerates that are formed, or even worse to the pump blockage.

Although it is not necessary for the slurry to be absolutely stable for long periods of time, it has to be stable at least for the time of the process, which is in the order of few hours usually.

2) viscosity is the main parameter, since it influences the pumping and the spreading of the slurry under the blade.

Too high viscosity will result in sticking of the slurry under the doctor blade, while too low viscosity will cause the slurry to spread too fast, without following the doctor blade.

Both the stability and the viscosity depend on many other parameters:

1) solid content.

2) shape and particle size distribution of the powder.

3) electrical charge on the oxide surface, that in turn is mutually related to the pH and to the oxide composition.

4) presence of organic additives

Since there are so many variables, and also the viscosity and the stability are related each other, it's really hard to optimize both.

When the organic content is low, stability is mainly due to the electrostatic repulsion between the particles, caused by the presence of electrical charges on the surface.

A brief overview on stabilization principles will be given here.

3.1.2 Slurries stabilization

Electrostatic stabilization

Derjaguin, Landau, Verwey and Overbeek explained independently the electrostatic interaction between two suspended particles, and they formulated a theory known as DLVO.

It is well known that on the surface of a particle in a liquid some electrical charges can be formed.

Since all the particles charge in the same way, there is a repulsive effect, that counter the attractive Van Der Waals forces, that on the opposite tend to coagulate the suspension.

The hydrate oxides in water can react and develop positive or negative charges:

$M\text{-}OH + H^+ \rightarrow M\text{-}OH_2^+$

$M\text{-}OH + OH^- \rightarrow M\text{-}O^- + H_2O$
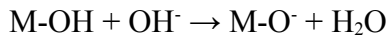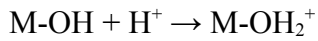
Clearly this equilibrium depends on the pH, and so also the surface charge.

For every suspension there is a pH when the surface is neutral, and this is called point of zero charge (PZC).

When the pH is close to PZC the particles are almost neutral, so there is no repulsion and they tend to coagulate.

The surface charge is not enough to describe the system, because the particle tends to attract opposite charged ions from the liquid.

So a layer of counter-ions is created, and the potential is faded away from the surface.

In particular there is a first layer, called Stern layer, where the counter-ions are bonded to the surface and the potential decreases linearly with the distance.

The second layer is called Gouy layer, and here the potential decrease exponentially [3]

[3] $\Phi \sim exp\ (\text{-}k(x\text{-}H))$ where

H is the Stern layer thickness,

x is the distance from the surface

1/K is the screening length, and depends on the solvent properties [4]:

$$[4] \quad K = \sqrt{\frac{F^2\ \Sigma\ c_i z_i^2}{\epsilon_r \epsilon_0 N_A k T}}$$

F= Faraday constant, c_i and z_i= concentration and valence of the counter-ions

k= Boltzmann constant, NA= Avogadro constant, T= temperature, ϵ_r and ϵ_0 = dielectric constants of the solvent and vacuum.

When K is high, the repulsion is more effective at big distance.

When an electric field is applied, the particles move together with only a part of the double layer: the plane that separates this part is named "slipping plane".

The potential at this point is called "zeta potential", and the pH when the zeta potential is zero is called isoelectric point.

What determines the stability is the sum of the attractive and repulsive potentials, that usually is plotted as in **fig.22**
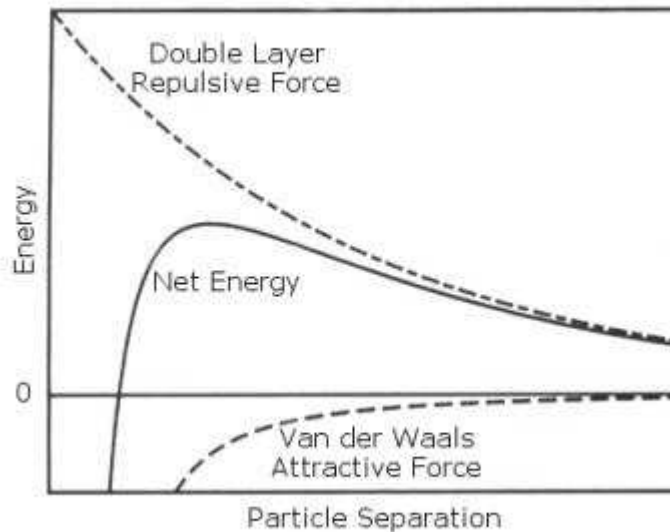
fig.22 plot of the Van der Waals attractive forces and the double layer repulsive forces

[5] U= Ua + Ur is the total potential, where

[6] $U_R = \dfrac{\epsilon_r a^2 \Phi_0^2}{4(x+a)} \exp(-Kx)$ is the repulsive potential

[7] $U_A = \dfrac{Aa}{24x}$ is the attractive potential

a= particles diameter, ϕ_0 is the surface potential, x= particles separation

A= Hamaker constant

When the particles are far apart they repel, but when, thanks to the Brownian motion or a shaking they have enough energy to overtake the energy barrier, then they come to a deep attractive minimum and they precipitate.

Often only the zeta potential is measured, because it gives a simple information of the particles charge, that can be approximatively correlated to the stability of the system by **tab.7**

Zeta potential [mV]	Stability
0- to ± 5	instantaneous coagulation
±10 to ±30	instable
±30 to ±40	quite stable
±40 to ±60	good stability
> ±61	very stable

tab.7 approximative correlation between zeta potential and stability

Steric stabilization

For polymers with molecular weights >10000 D, the chain dimensions are comparable to, or in excess of, the range of the VDWL attraction. Hence, as long as they can generate repulsion, these polymer molecules can be used to impart colloid stability.
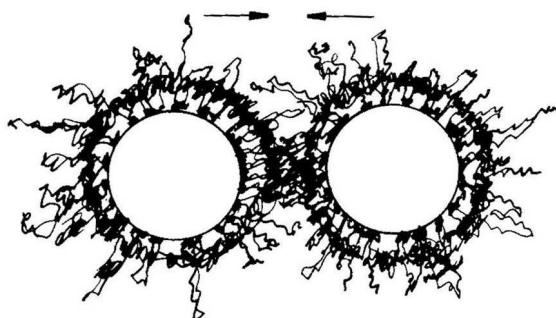
fig.23a Scheme of steric stabilization
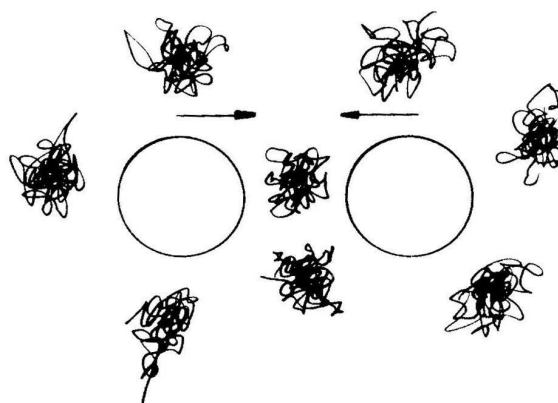
fig.23b Scheme of depletion stabilization

There are two different mechanisms accepted for polymeric stabilization of colloidal dispersion: steric stabilization and depletion stabilization.
Steric stabilization of colloidal particles is achieved by attaching (grafting or chemisorption) macromolecules to the surfaces of the particles (**fig.23a**[8]). The stabilization due to the adsorbed layers on the dispersed particle is generally called steric stabilization.
Depletion stabilization of colloidal particles is imparted by macromolecules that are free in solution (**fig.23b**). The study of this type of stabilization is still in its initial stage.
Electrostatic and steric stabilization can be combined as electrosteric stabilization.

---

8   Image from: Centre for Industrial Sensors and Measurements Department Materials Science & Engineering Group Inorganic Materials Science Literature Review; Ohio State University

3.1.3 Slurries viscosity

Viscosity is the ratio of the shearing stress (F/A) to the velocity gradient (dv_x/dz).

Simple fluids like water are Newtonian, which means that their viscosity does not change with the shear rate.

Non-Newtonian fluids can be mainly divided in two groups:

-Pseudoplastic: as shear increases, viscosity decreases. Many polymeric materials are pseudoplastic.

- Dilatant: these are the opposite of pseudoplastic that is, as shear increases the

viscosity increases. Some highly filled materials are dilatant.

The effect of the powder parameters on the slurry viscosity will be explained (32)

Effect of particle size

Reducing the particle size means increasing the number of particles in the system; a higher number of smaller particles results in more particle-particle interactions and an increased viscosity.

As shear rate increases, this effect becomes less marked, suggesting that particle-particle interactions are relatively weak and break down at high shear rates; this leads to a pseudoplastic behaviour, that is often observed in slurries containing a fine powder.

Effect of volume fraction

The effects of volume fraction and maximum volume fraction on viscosity are described using the Krieger-Dougherty equation:

[8] $$\frac{\eta}{\eta_0} = \left(1 - \frac{\Phi}{\Phi_m}\right)^{-[\eta]\Phi_m}$$

h - Viscosity of the suspension,

η_0 – viscosity of the medium,

f - Volume fraction of solids in the suspension,

f_m – maximum packing fraction

$[\eta]$ – Intrinsic viscosity (2.5 for spheres)

This correlation indicates an increase in viscosity with increasing volume fraction. As the volume fraction of solids in the system goes up, the particles become more closely packed together, particle-particle interactions increase and so viscosity rises.

As the volume fraction nears maximum for the sample, viscosity rises very steeply.

Effect of particle size distribution

Particle size distribution influences particle packing: a polydisperse population with a broad size distribution packs more closely than a monodisperse one. The effects on viscosity can be explained with reference to the Krieger-Dougherty equation.

With a polydisperse sample smaller particles can fill gaps between larger ones and the maximum volume fraction is greater. Increasing the distribution width for any given volume fraction of solids will reduce the viscosity of the system.

3.1.4 Silica slurry

Based on the zeta potential measure (by A. Gahler) in **fig.24**, a suitable pH value was chosen for the silica slurry.
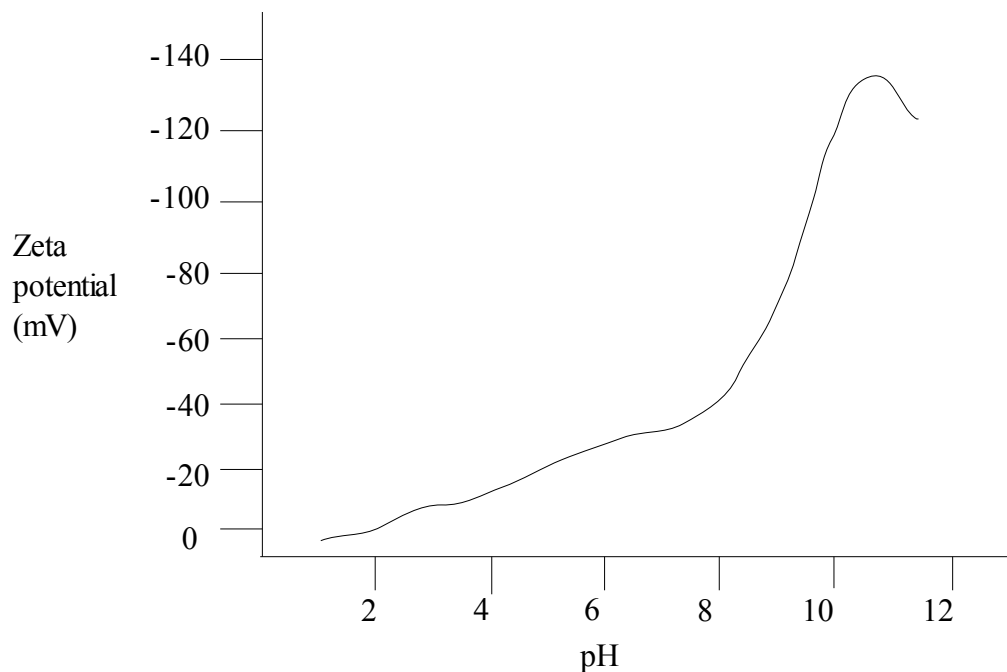
fig.24 zeta potential vs pH of the silica slurry (60%silica + 6% nano-silica)

At the natural pH, the silica slurry is completely unstable since this pH is really closed to the zero charge point value. In facts a suspension like this is actually stable only for few minutes, after that a dense precipitate forms at the bottom of the container.

A sufficient stability can be obtained for pH values between 5.5 and 11.

The exact value was chosen in this range in order to have a suitable viscosity.

The measured viscosity curves (**fig.25**) at different pH show a pseudoplastic behaviour.
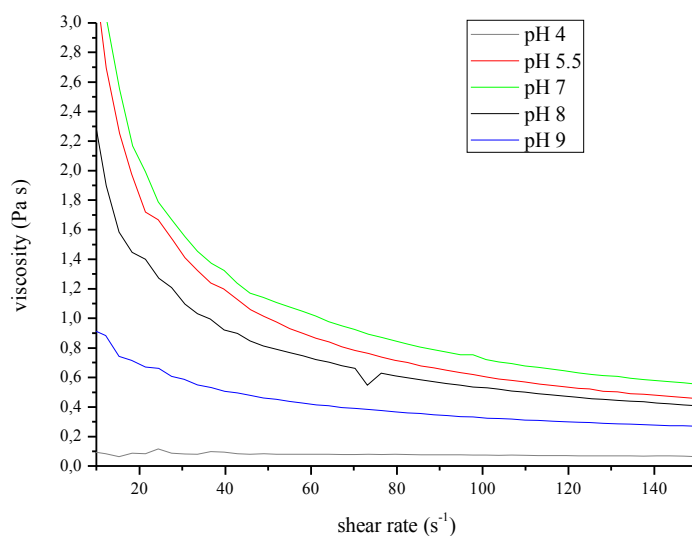
fig.25 viscosity curves of the silica slurry at different pH

At natural pH 4 the viscosity is far too low, moreover this slurry forms a deposit within few minutes, so it is totally not utilizable.

An addiction of KOH to higher the pH, instead, suddenly increases the viscosity.

There is a maximum in the apparent viscosity at pH 7 and then it slightly decreases.

Even though the slurries at pH 5.5-9 have a high viscosity for low shear rates, the data at 50 s^{-1} and 150 s^{-1}, that are more relevant for the process are between 0,8 Pa s and 1,2 Pa s, which is a good value.

At the end a good compromise between stability and viscosity was found with a pH 7.

3.1.5 LAS slurry

Viscosity was measured for the compositions listed below, with the aim of investigate the influence of different parameters, as it will be discussed in this paragraph.

Ls1= powder LAS1 70%wt + H₂O 30%wt

Ls2= powder LAS2 75.5% + H₂O 24.5%

Ls3= powder LAS2 75.5% + H₂O 22% + PEG 2.5%

Ls4= powder LAS2 75.5% + H₂O 21% + PEG 3.5%

Ls5= powder LAS2 78% + H₂O 22%

Ls6= (powder LAS2 78.2% + H₂O 21.5% + 0.3% dolapix) + 5% binder

binder= H₂O 82% + PVA 16% + PEG 2%

Ls7= powder LAS2 64% H₂O 34% + hydroxyethylcellulose 2%

Ls8= powder LAS2 67.5% + H₂O 30.7% + PEG 0.9% + hydroxyethylcellulose 0.9%

Fig.26 shows the effect of the pH on the viscosity of a LAS slurry (Ls1).
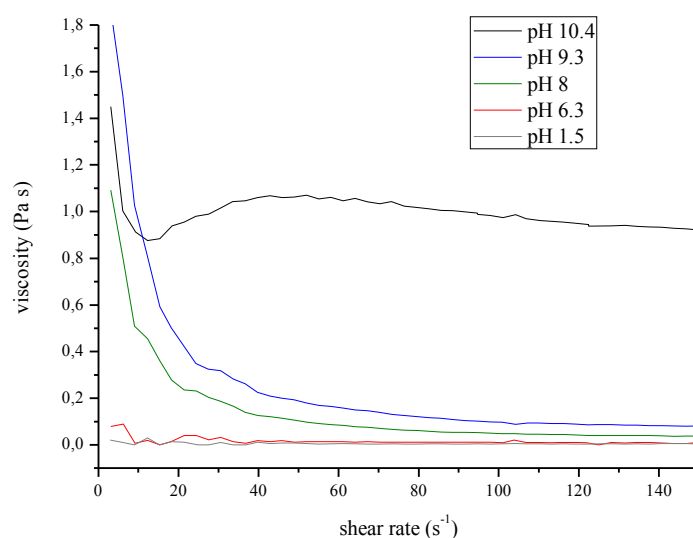
fig.26 viscosity curves for the Ls1 slurry at different pH

At natural pH (about 10.5), the viscosity already fits with the parameters required for the process, while lowering the pH leads to a pseudoplastic behaviour and to an unwanted strong decrease of the apparent viscosity.

Moreover, for all the LAS compositions, a good stability could be achieved without changing the pH.

So it was decided to maintain always the natural pH, and, when needed, to regulate the viscosity by varying the solid content or adding some organics.

In **fig.27** eight different viscosity curves are plotted, which differ for particle size, solid

content and organic additives.
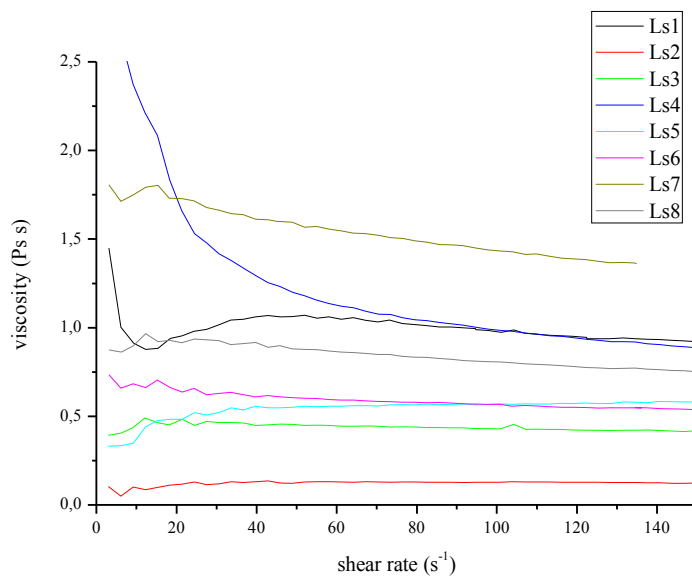
fig.28 Viscosity curves for eight different LAS slurries

Ls2, Ls3, Ls4 have the same solid content but increasing content of PEG.

It is pretty evident that adding more PEG means increasing noticeably the viscosity, even with few percent (2-3%).

Note that laser burns the organics, so only few percent of additives is allowed, otherwise cracking will occur because of the gas release. This is also good because few organics and high solid load will result in a high layer density.

An addiction of more than 3% (Ls4) causes also a relevant pseudoplastic behaviour, while this effect is not noticed for lower amounts.

A comparison between Ls1 and Ls2 curves highlights also the effect of the particle size:

although Ls2 has a higher solid content (75.5% instead of 70%), Ls1 still has a higher viscosity.

Ls2 in facts has a mean particle size of about 9 μm, and Ls1 only 6 μm (see 2.3.2).

This can be explained easily, because the smaller are the particles, the higher is their number (for a constant mass), so also is higher the number of interactions and resistance to flow.

These interactions cause also the tixotropic behaviour of the Ls2 curve, since these weak bonds are effective at low shear rates, but then are broken for high shear rates.

The solid load effect is quite easy to understand: Ls5 has the same powder of Ls2 but a higher amount, and consequently also a higher viscosity.

Hydroxyethylcellulose has a strong influence on the viscosity, but contrary to PEG does not cause a strong pseudoplasticity.

Ls7 has the highest viscosity, even if it has the lowest solid load (64%) and only 2% hydroxyethylcellulose.

Finally, Ls8 with PEG and hydroxyethylcellulose   is probably the best slurry for the viscosity and stability point of view, with values around 0,9-1 Pa s and stable over many days.

3.2 Layers deposition

3.2.1 Overview and experimental apparatus

Fig.29 shows the instrumentation used to simulate the layerwise slurry deposition process: first the slurry is dropped on the ceramic tile, then the blade is pulled and a layer of constant thickness is deposited.

After a waiting time for the drying (possibly made faster with a heater) the blade is lifted up of 100-200 μm, so the process can restart with a new layer and so on.
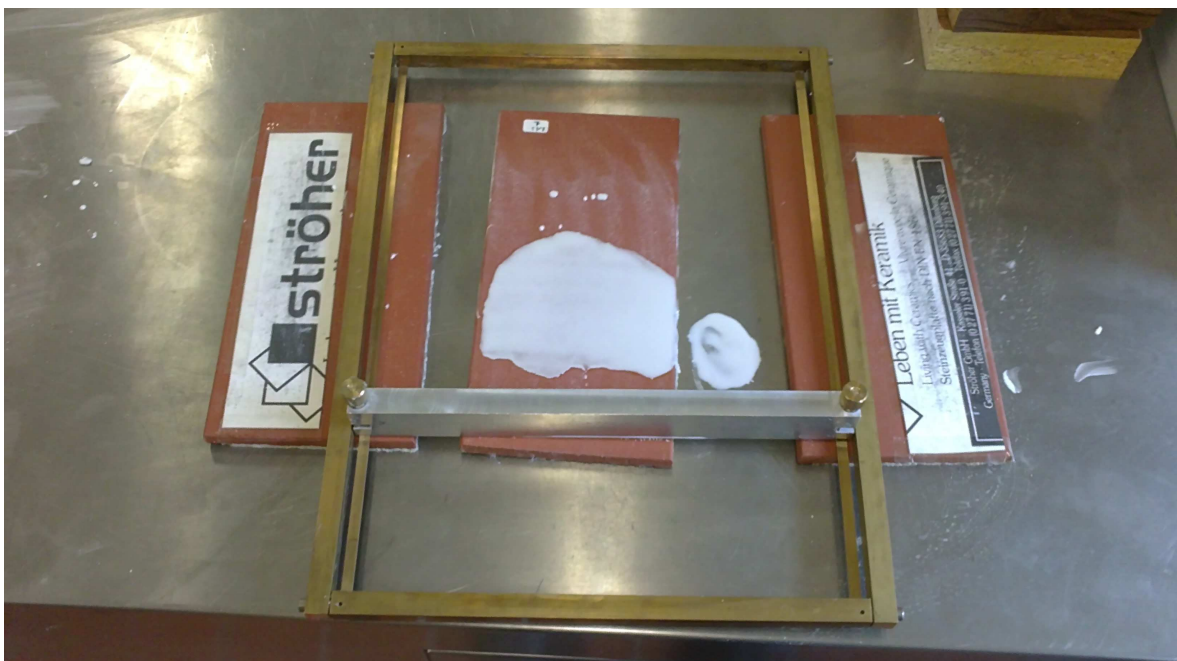
fig.29 Instrumentation used to simulate the layerwise slurry deposition

50

In the machine for the automatic laser sintering of LSD the operations are basically the same, except for the fact that the table moves instead of the blade, and moreover the slurry is provided by a pump.

A picture of the fiber laser rapid prototyping apparatus can be found in **fig.30**
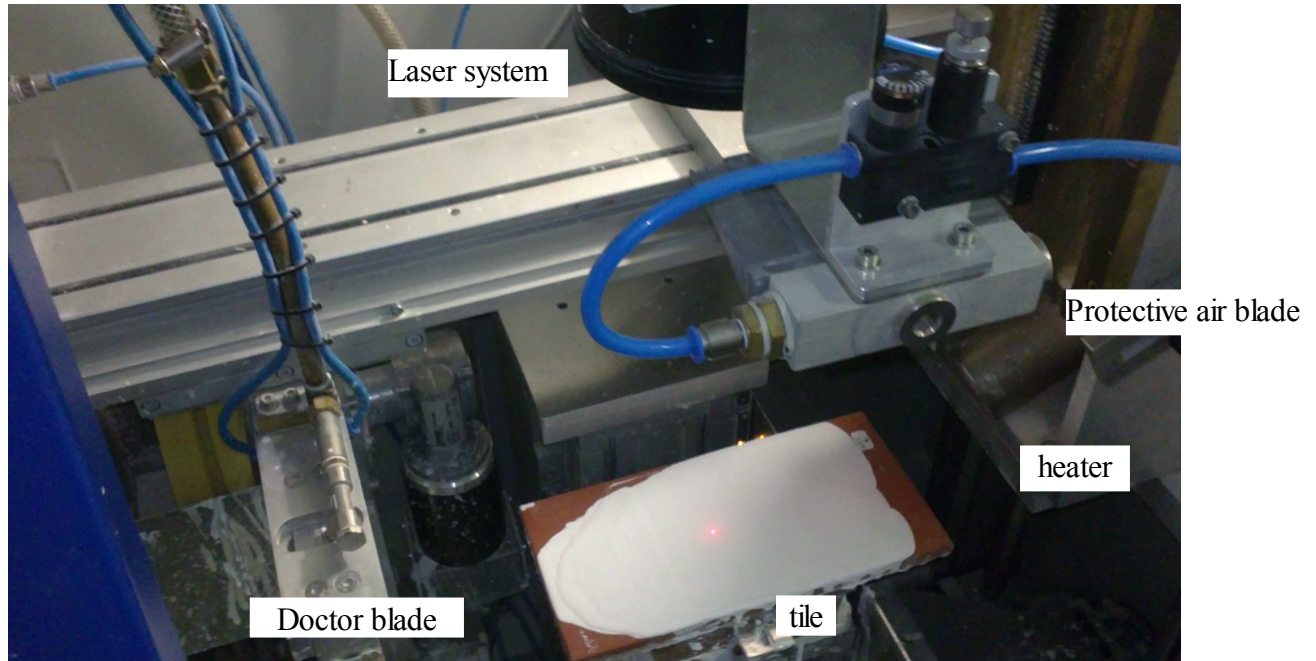
fig.30 Automatic machine for Laser Sintering of LSD

It is very important that when the laser starts there's no more than a 3% of left water in the layer. Otherwise the sample would be cracked and seriously damaged by water evaporation **(33)**.

Thus, it is fundamental to ensure a perfect drying of the layer.

On the other hand, often the main problem in a tape casting process is the formation of cracks and delamination during this stage, due to the mechanical stresses developed mainly during the shrinkage.

So it seems worthy to present briefly the basics of the theory of drying, and the consequences that this has on the deposition.

3.2.2 Drying stage

This theory was elegantly summed up by George W. Scherer **(34)** in the case of sol-gels, but it can easily be extended to many processes where a drying stage is involved.

Although there can be different forces involved in drying, as the osmotic pressure for example, the main role is surely played by the capillary forces.

In facts when the evaporation of water is at the point to expose the solid phase, the liquid tends to spread curving in a meniscus, so avoiding to replace a solid/liquid interface with a more energetic solid/vapour interface.

The pressure P in the liquid is related to the radius of curvature (r) of the meniscus by

[9] $\quad P = \dfrac{-2\gamma_{lv}}{r}$

γ_{lv} is the liquid/vapour surface tension.

The maximum pressure is reached when the meniscus fits into the pore: in this situation

[10] $\quad r = \dfrac{R}{\cos\Theta}$

where R is the radius of the pore and Θ is the contact angle. So, substituting [10] in [9]:

[11] $\quad P_{max} = \dfrac{-2\gamma_{lv}\cos\Theta}{R}$

The pore is supposed to be cylindrical, but the equation can be corrected for a general shape.

The stages of drying are mainly two:

(1) Constant rate period (CRP)

in this stage the evaporation rate is constant and similar to the bulk liquid, because the surface is still covered with a thin film of water (**fig.31**).
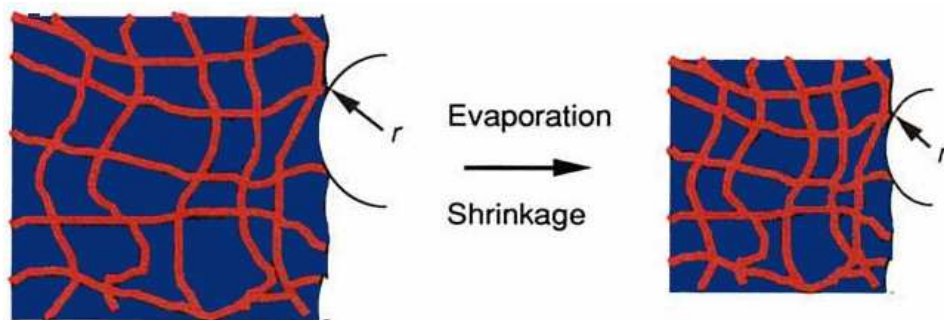
fig.31 Sample shrinkage in the constant rate period

The evaporation rate is given by:

[12] $\quad V_e = k\left(P_o \exp\left(\dfrac{-2V_m\gamma_{lv}}{R_g T r^\circ} - P_a\right)\right) \qquad r^\circ = -\left(\dfrac{R}{\cos\Theta}\right)$

where k is a constant and depends on the drying conditions, P_0 is the vapour pressure over a flat water surface, Vm is the molar volume of water, Rg is the ideal gas constant, T is the temperature in Kelvin and Pa is the ambient vapour pressure.

When the menisci are formed, the rising tension in the liquid is supported by the solid phase, which goes in compression.

In this way the body starts to shrink, and the total shrinking corresponds to the volume of liquid evaporated.

While evaporation continues the menisci radius decreases gradually, and so the pressure increases, until the menisci fits into the pore and the maximum tension is reached.

At this point there is the changeover to the following stage, and shrinking stops.

(2) Falling rate period (FRP)

When shrinkage stops and the meniscus enters into the capillary, air starts to enter the pores (**fig.32**).
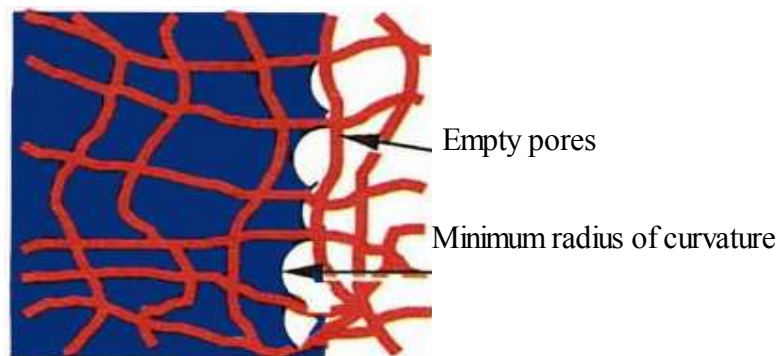
fig.32 sample during the falling rate period

The liquid near to the surface remains in funicular conditions, in a wet layer that covers the walls (**fig.33a**). Through this phase the liquid can flow from the inside to the outside.
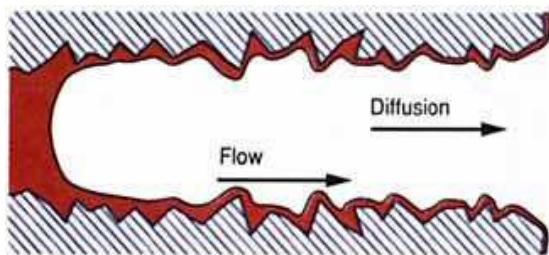
fig.33a liquid in funicular conditions
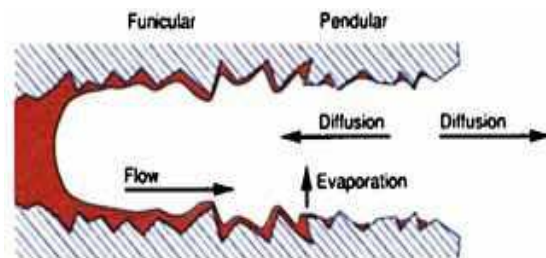
fig.33b liquid in pendular conditions

Some liquid also evaporates from the interior part, and vapour is transported by diffusion.

At a certain point the flow becomes too slow to preserve the funicular condition, so only isolated drops remain (**fig.33b**).

The only transport process possible from now is the diffusion, so this step may take a long time.

Surely a high capillary pressure helps to achieve a low porosity in the green body, but it might also lead to cracking. Cracking can be caused by the high absolute value of the stress developed, but also to warping, due to a stress gradient.

At first indeed the surface exposed to air is compressed more than the lower surface, and liquid from the other surface is drawn in order to have a uniform hydrostatic pressure.

If the structure is not permeable enough, a gradient is created and the upper surface is much more compressed than the other, so the body tends to warp as in **fig.33a**.

At the end of the drying the upper surface is dry, while the bottom is still wet and compressed, so the body tends to warp in the opposite direction (**fig.33b**).
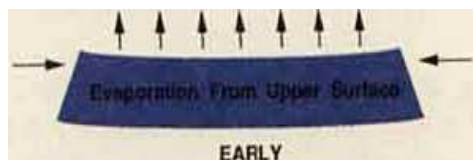
fig.33a warping during drying   *fig.33b*
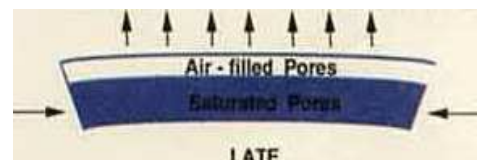
In a laminated system, the layer is not free neither to warp nor to shrink, but it is sticked to the previous layer, so as a consequence mechanical stress rises.

Even though the standard thickness is only 100 μm, cracking may happen, but it can usually be avoided finding a suitable slurry composition.

It has also to be explained that the thickness of the first slurry layer as deposited is 100 μm, but during the drying it decreases because of the shrinkage.

Weihua Lan and Ping Xiao **(35)** measured a thickness reduction up to 48% for a YSZ slurry with a 33% water content and a thickness of 500 μm.

So the first layer is surely less than 100 micron thick, but yet for the next layer the blade moves exactly 100 μm up: the new distance between the layer and the blade then is more than 100 μm, so the value after drying will be closer to 100 μm and so on for the following layers. At the end a constant value of 100 μm after drying is reached.

The real thickness can be calculated by the following formula, **(5)**

[13] $T_l(n)=H(1-a^n)$ where $T_l(n)$ is the thickness of the n-th layer after drying, H is the pre-set slurry deposition thickness (0.1mm in this research) and "a" is the shrinking ratio of slurry layer during drying process.

If a= 0.4 and n=10 then t(10)= 99.99 μm so the theoretical value is achieved.

Usually in the process ten pre-layers are built before starting with the laser layers, and this is done both for this reason and also because often the first few layers have some defect.

3.2.3 LAS layerwise slurry deposition

The standard drying theory however does not consider the effect of the substrate, since the hypothesis is that the liquid is removed only from the upper surface.

This is true of course for the first layer, because the substrate is a dense material.

For the following layers anyway the substrate is another layer, so it is porous, and the water can be drained also from the bottom.

This might be problematic, as illustrated in the sequence of pictures in fig.34a,b,c

fig.34a first layer with Ls1   *fig.34b second layer*
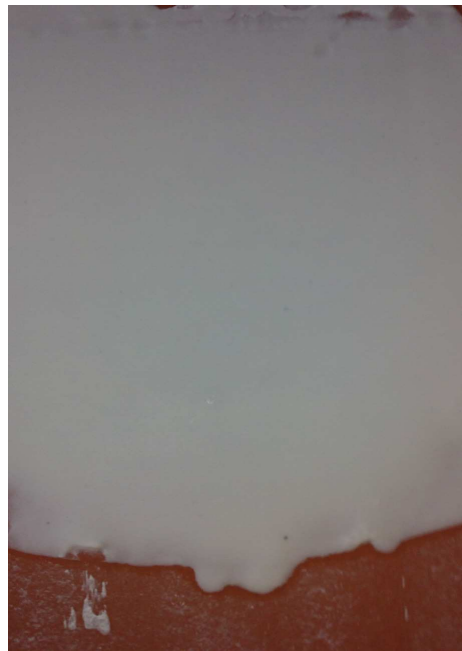
fig.34c third layer

With the simple Ls1 slurry, which has no organics inside, the first two or three layers can be well casted.

After that the water is literally drained immediately by the layers beneath, so the slurry agglomerates, sticks under the blade and scratches all the surface.

For this reason other compositions were formulated, hoping to solve this point.

PolyEthylenGlicole was added (Ls3) with the aim of reducing the capillary forces that suck the liquid.

PEG acts as a non-ionic surfactant, lowering the surface tension of the liquid and the contact angle: it is pretty clear looking eq. [11] and [12] that both the capillary pressure and the evaporation rate must decrease.

PEG furthermore has also other advantages, since it increases the viscosity and it helps the stability, thanks to a steric stabilization effect.

In facts very good layers, defect-free and smooth have been laminated, as shown in the sequence of picture in **fig.35a,b,c,d**, thanks to the fact that they dry out slower.

*fig. 35a First layer deposited
with Ls3*

*fig. 35b Second layer deposited
with Ls3*

*fig. 35c Third layer deposited
with Ls3*

*fig. 35d Last layer deposited with
Ls3*

But these tapes could be deposited only using a little trick: with the PEG the layers remain wet longer, so it's possible to spread the slurry while the substrate is still slightly wet.

Otherwise, when the perfect drying is guaranteed by an external heating source, the problem comes back again, as the water is still drained quickly by the substrate (**fig.36a**).

For other tape casting processes, it might not be a big deal if the tape is slightly wet during the process, but as already explained, for the laser sintering this is not acceptable.

To have better results it probably would be enough to higher the PEG percentage, but this again does not fit the laser sintering requirements.

Other two compositions were examinated, one with hydroxyethylcellulose as additive instead of PEG (Ls7), and the other more complex, with dolapix as dispersant and a water-based binder containing PVA and PEG (Ls6).

Both with Ls6, Ls7 and Ls8 the drying behaviour is apparently improved, and most of the water is removed from the top instead than from the bottom layer (**fig.36b**)

fig.36a water drained from the slurry by the substrate

fig.36b with Ls6,7,8 the water is not drained any more

In facts ceramic tapes could be laminated even after complete drying with a heater.

These slurries seem to be promising for an application to the automatic process, even though they still should be optimized in some further studies.

Ls6 has PVA and PEG as main additives, while Ls7 has some hydroxyethylcellulose and Ls8 a mix of hydroxyethylcellulose and PEG.

The surface of the Ls6 layers is too porous and a few defects can be recognized (**fig.37**) due to the formation of bubbles. This might be solved either by addiction of a anti-foam agent or by slightly lowering the binder content.

Ls7 layers produced instead are defect-free, but the surface is quite too rough (**fig.38**).

With Ls8 is possible to produce good layers, but often the surface is ruined by the presence of many bubbles (**fig.39**).

58

Ls8 probably could be improved finding the best ratio PEG/Cellulose: cellulose improves the drying behaviour, while PEG helps to make the surface smooth.

Fig.37 Layers with slurry Ls6 (PVA + PEG as binders)
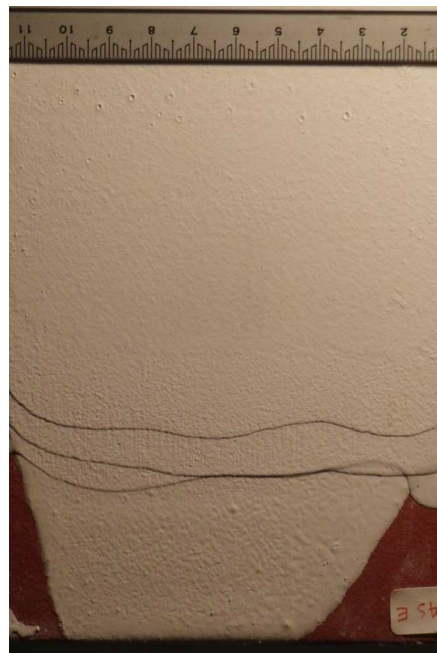
Fig.38 Layers with slurry Ls7 (Hydroxyethilcellulose as binder)
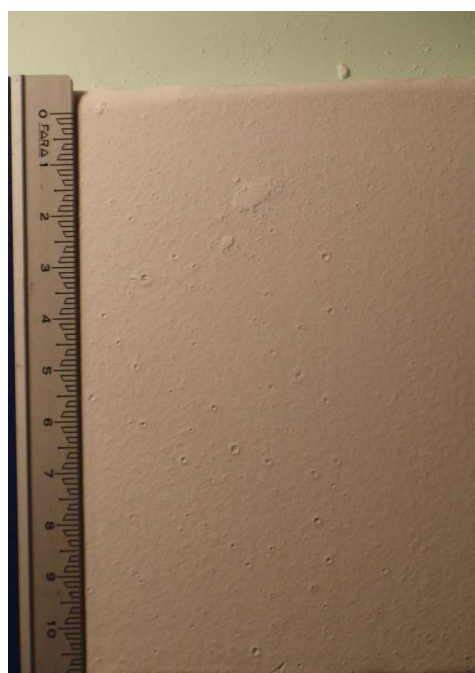
Fig.39 Layers with slurry Ls8 (PEG + Hydroxyethilcellulose as binders)

A laminated sample of 20 green layers (slurry Ls3) was sintered and crystallized in a furnace. The heating treatment is RT → (860°C, 8h) → RT with in this case a heating rate of 5°C/min and uncontrolled cooling.

The oven sintered object was then analyzed by SEM and XRD.

A SEM picture is shown in **fig.40**
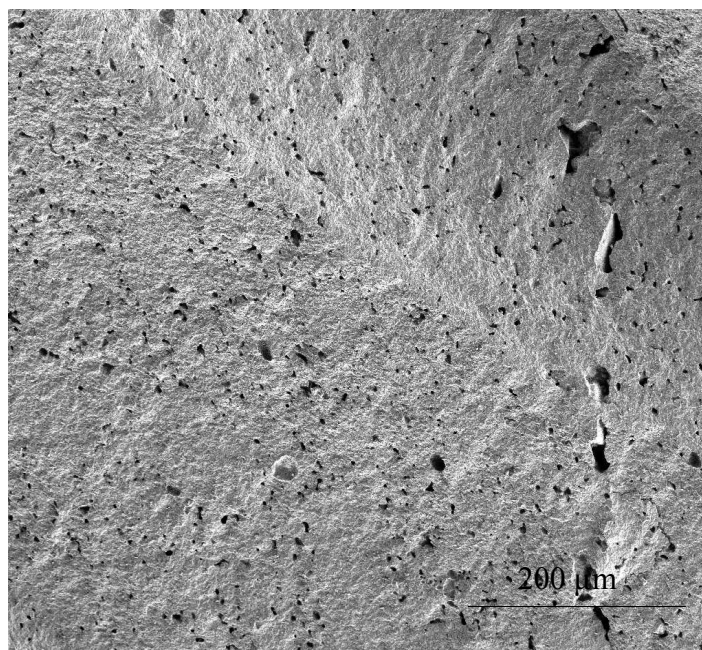
fig.40 SEM picture of 20 oven sintered layers

First of all, except for a line on the right, the laminated structure is not recognizable.

This means that the layers are sintered together very well, creating a connected sample.

The line of the right is instead one of the first layers, and as already said the first three or four are often not perfect.

The theoretical density was measured with a pycnometer (AccuPyc 1340 Pycnometer) on some powder crystallized in the same way and the value is 2.48 g/cm3.

Pores of diameter 5-10 μm remain and a density of 2.28 g/cm3 (92% of the theoretical density) was measured by Archimede's method in distilled water.

Only 1% of open porosity was measured, so the major part is closed porosity.

The phase composition was studied by XRD, and the relative diffractogram is in **fig.41**

As expected, the main phase is β-spodumene, and the second phase is lithium silicate $Li_2(Si_2O_5)$ [082-2396].
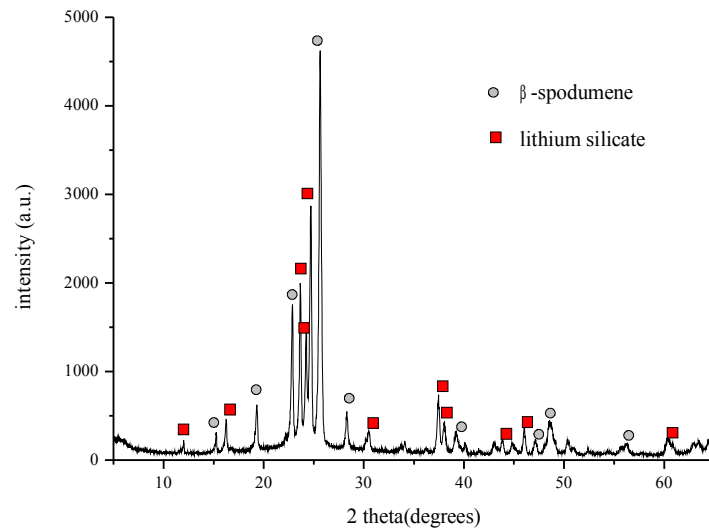
fig. 41 diffractogram of the oven sintered sample

Seemingly, the starting glass crystallized almost completely, and only a little fraction of amorphous is left.

3.2.4 Silica layerwise slurry deposition

The silica slurry could be successfully deposited without macroscopic defects, and so was used for the automatic process.

A sequence of pictures in fig.**42a,b,c** displays the casting of the first four layers.

fig.42a First silica layer deposited

fig.42b Second silica layer deposited

fig.42c Fourth silica layer deposited

A laminated sample made up of more than 50 layers is shown in **fig.43**
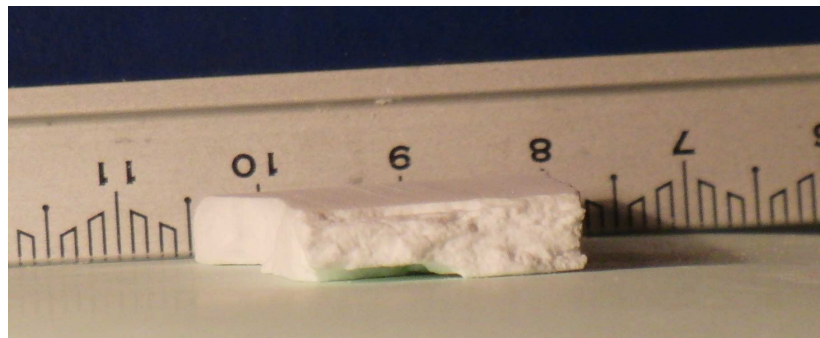
fig.43 Silica laminated sample with over 50 layers

A density of 1.57 g/cm3 was measured by Archimede's method; this value is 71% of the theoretical density of silica, and is close to the maximum packing density for a green object.

This value might be a little overestimated because the water may have not saturated all the small pores; nevertheless, it is certainly true that with this process a high green density can be achieved.

62

3.3 LASER SINTERING

3.3.1 Laser parameters

3.3.1.1 Overview

The main variable parameters are three:

- **output power**

- **scan velocity**: when an area has to be scanned, it is first hatched, that means divided in parallel lines.

The laser scans a first line, then moves and scans another parallel line and so on, until all the area is filled.

- **hatch** = the distance between two scanning lines is called hatch.

Since the interaction laser-material is never in a single point but there always is a heat affected zone around, also the material between the "geometrical" lines is sintered.

A parameter that includes power and scan velocity is the laser energy density, defined

[14] $ED = \dfrac{P}{Dv}$ $(\dfrac{Ws}{mm^2})$

where P= laser power D= spot diameter (mm) v= scan velocity (mm/s)

Two different lasers have been used, a fiber laser (D=0.08 mm, maximum power=100W) for LAS and a CO_2 laser (D=0.2 mm, maximum power= 100W) for silica.

3.3.1.2 Silica laser parameters

For sintering the silica slurry the following parameters were used, because they were found to be suitable in a previous work by André Gahler **(36)**:

hatch= 0.05 mm

power= 60W   --------------> laser energy density= 3 Ws/mm²

speed= 100 mm/s

3.3.1.3 LAS laser parameters

A single layer of LAS, casted with slurry LAS2, was laser sintered to observe the effect of the scan velocity and the power. The hatch value was instead set to 0.1mm and not modified.

First of all it was noticed that when the sample is at room temperature it is not possible to sinter without creating cracks and severe delamination (**fig.44**).
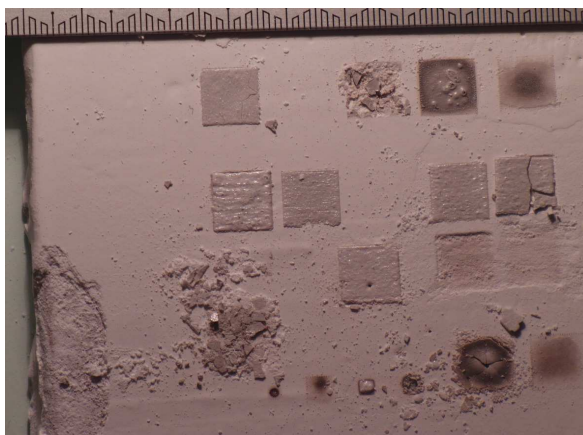
fig.44 when the tile is not preheated it is impossible to sinter

However this problem was solved with a pre-heating to 150°C, whose effect is hereby explained.

The cause of cracking is probably the quick burning of the polymer after the laser interaction, because of the gas expansion inside the material.

A pre-heating probably slowly burns part of the polymer, so less organic is left when the laser starts.

This theory is supported by the fact that a layer that does not contain any organic can be sintered even at room temperature without delamination.

The layers parameters were analysed sintering 1cm x 1cm squares, with power in the range 15-39 W and scan velocity 20-80 mm/s. The result is shown in **fig.45 (next page)**
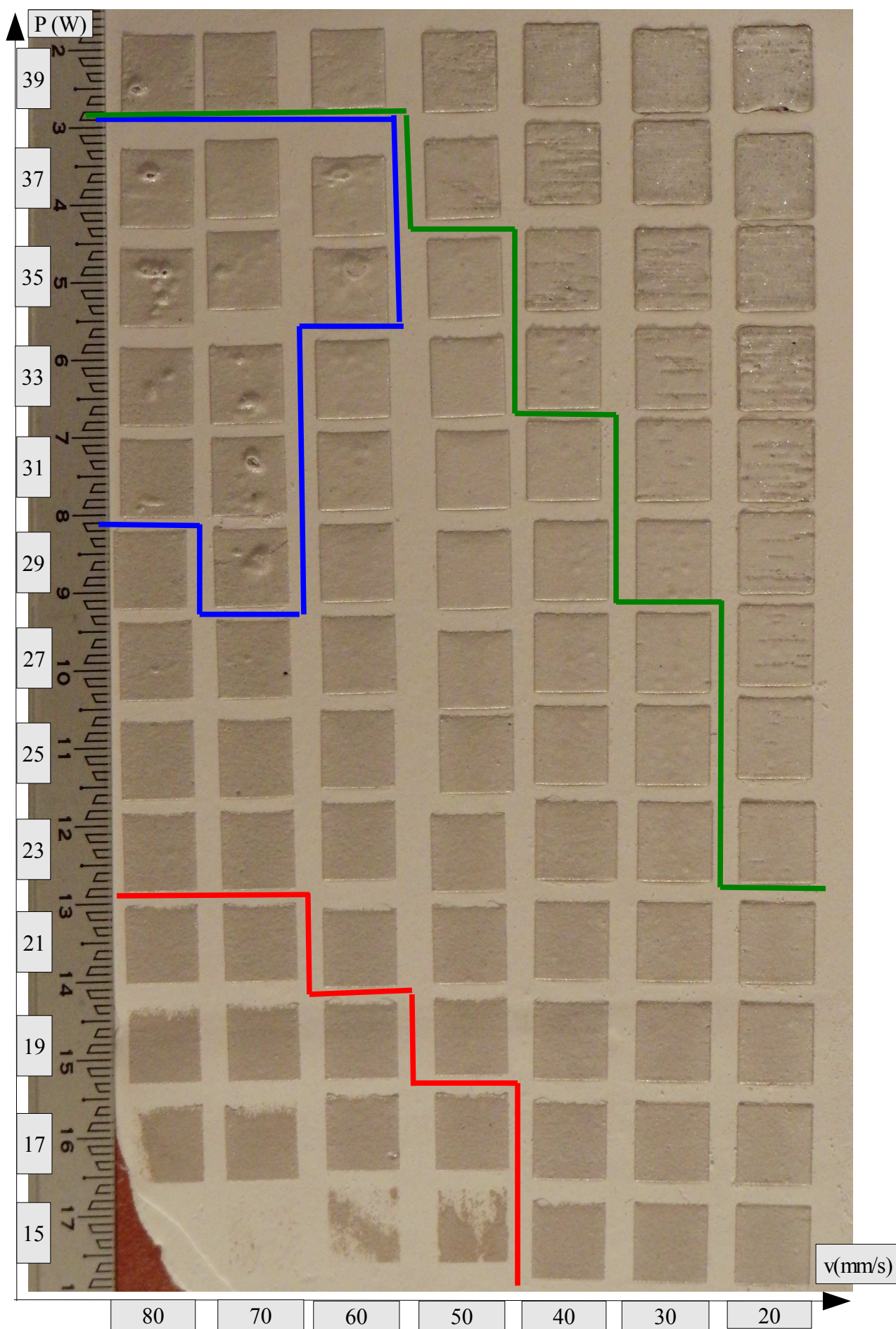
The graph is divided in four zones:

A	B	C	D
———	———	Middle zone	———

A) marked by the red line, it is a non completely sintered zone, where the energy is too low.

B) marked by the green line, it is a zone where the energy is too high, and a rough surface, cracks and delamination are the consequences.

C) with these parameters in the middle, it is possible to sinter stable parts, defect-free, with a smooth surface and a relatively high penetration depth.

D) in the zone marked in blue, the squares have a quite regular surface, but there are many big bubbles that ruin the samples. This is probably due to the polymer evaporation, as will be examined more in detail later.

However it has to be remarked that these squares have a rough appearance for a different reason than the squares in the zone C), where instead the roughness is strictly related to the excessive power.

To visualize better the situation, the points of fig.45 have been plotted in a graph, in **fig.46**. In red there are the "stable" value, while in grey-black the points that lead to a defected structure.
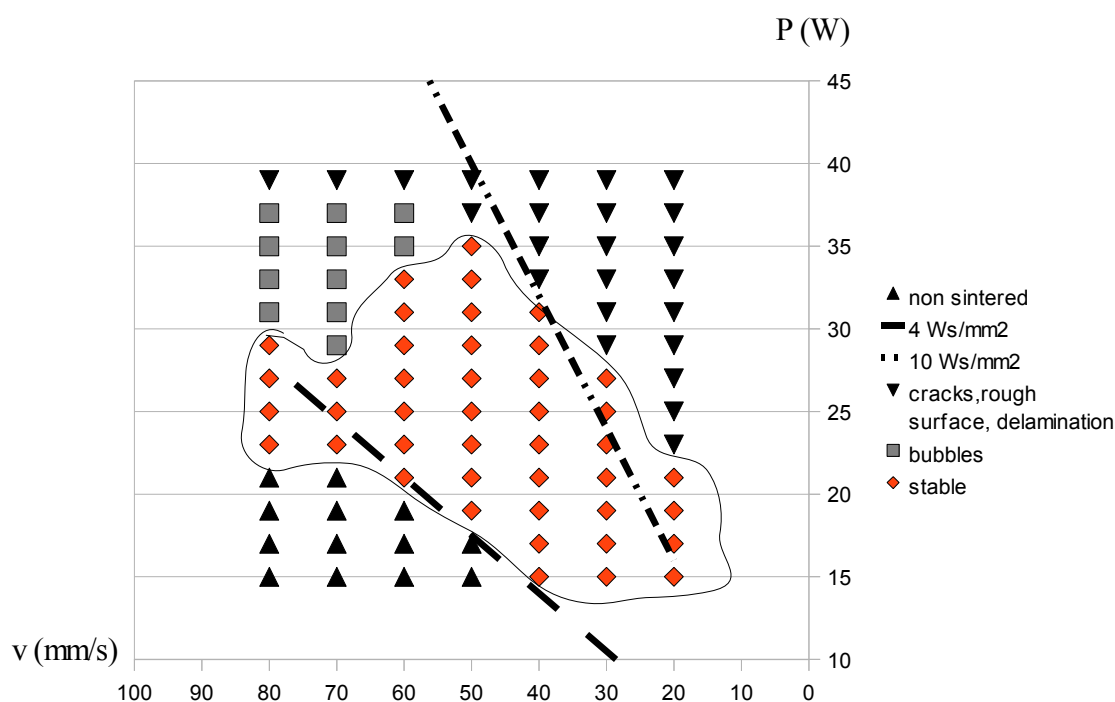
fig.46 Plot of the points corresponding to the squares in fig.45

The area of stability is surrounded with a black line. In fig.46 two lines are also drawn, that correspond to a constant value of the energy density, as defined previously.

The energy density seems to represent well the interaction of the two parameters power and scan velocity. More or less squares that have the same energy density value look in facts similar.

In particular the squares sintered with an energy density above 10 Ws/mm^2 have defects and they are in the green zone.

Furthermore, squares between 4 and 10 Ws/mm^2 are well sintered, and the ones with values < 4 Ws/mm^2 tend to be not completely sintered.

Actually for high scan velocities this pattern is not kept up, and it is possible to sinter stable parts even with parameters under the line, so with higher powers than one can expect.

This is probably because when the scan speed is high, only a limited intensity can be absorbed by the substrate. A similar behaviour was observed in other studies **(23)**

The squares have been pictured at higher magnification with a stereoscope (**fig.47a,b,c,d,e**); it can be noted that there are cracks at the corner of many samples, and that there are always a lot of small bubbles, even at low energy.

It is evident at 17W, 70 mm/s that the sample (**fig.47a**) is not completely sintered.

The big bubbles of a sample in the blue zone are instead well visible in fig.47e.

The surfaces have a glassy appearance, especially at high energy density (for example at 37W, 30 mm/s, fig.47d) that will be investigated later.

Fig.47a square sintered at 17W 70 mm/s

Fig.47b square sintered at 23W 80mm/s
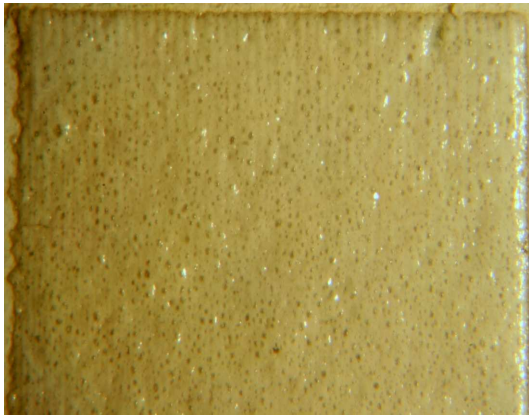
Fig.47c square sintered at 27W 60mm/s
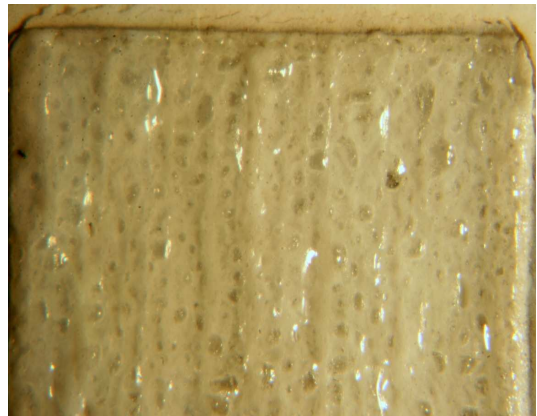
Fig.47d square sintered at 37W 30 mm/s
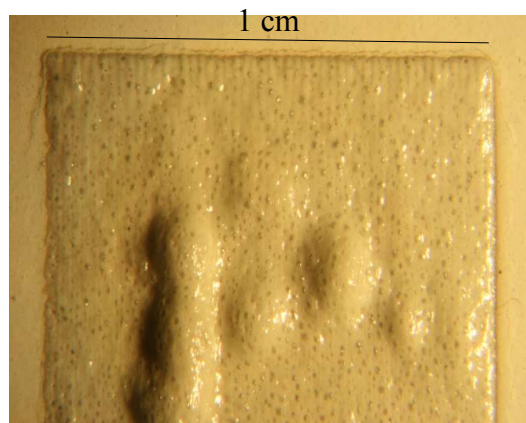
Fig.47e square sintered at 35W 80 mm/s

Another layer deposited without any organic inside (slurry Ls1) was laser sintered to explain two not clear points:

– why the squares are grey-brownish, while the glass should be transparent

– why the small bubbles are present in every sample

A picture of this layer is in **fig.48** The squares are 1cm x 1cm

fig.48
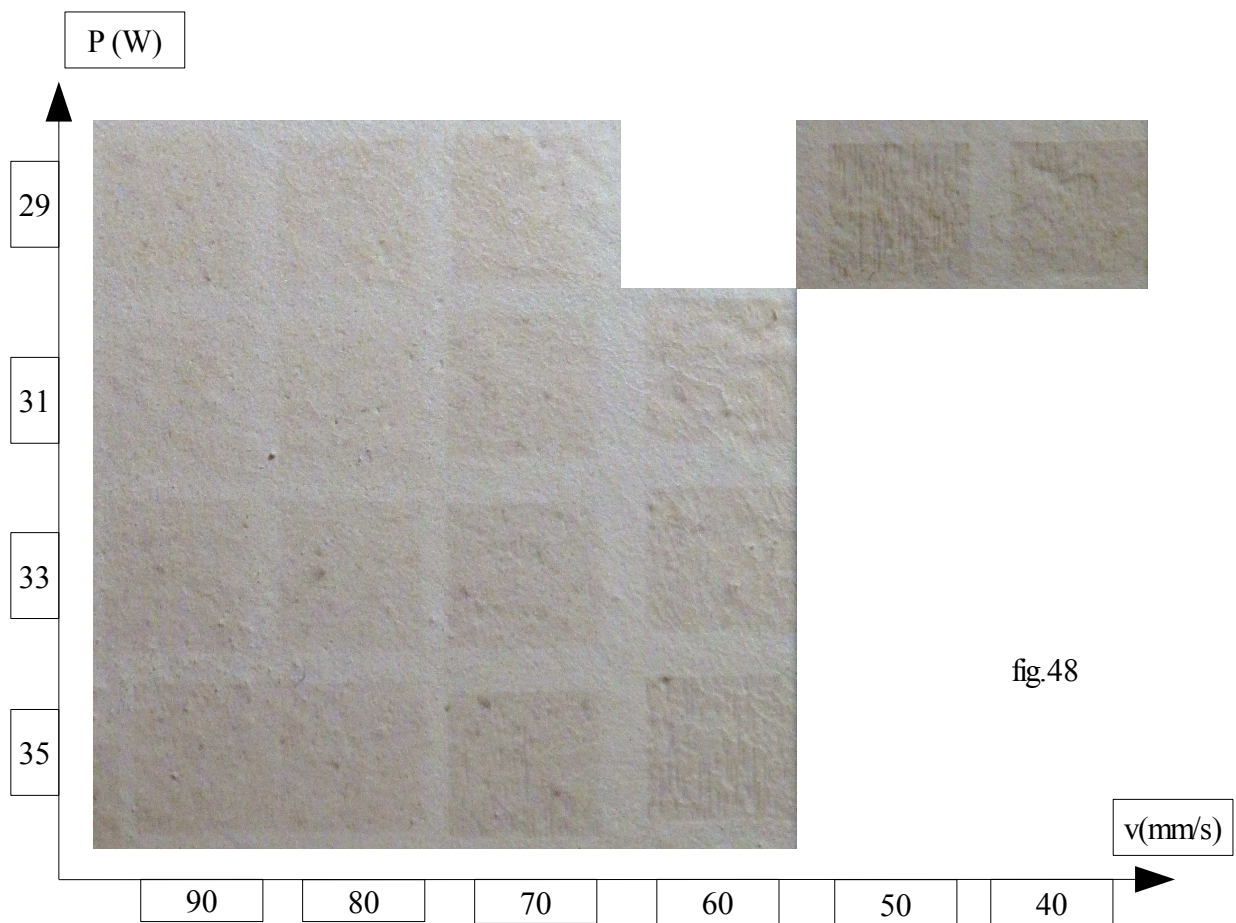
Concerning the first point, there is no doubt that the colour is caused by the organic burning, and otherwise the sintered material would be transparent as in the picture.

Secondly, there are no bubbles in this layer, but it seems also more complicated to sinter the pure material without additives.

In facts even using a high energy density, the laser does not sinter the material in depth.

So, it is likely that the bubbles are due to the interaction between the laser and the organics, but also that this interaction is necessary at least to start the sintering, because otherwise the laser does not couple well with the raw powder.

This aspect should be however investigated wider in further studies, and it would be interesting to tailor the material absorption by modifying the organic content.

3.3.2 Laser sintered layers characterization

3.3.2.1 LAS

The square sintered with (27W, 60mm/s) was analyzed at SEM to observe the cross-section (**fig.49**).

laser

200 μm
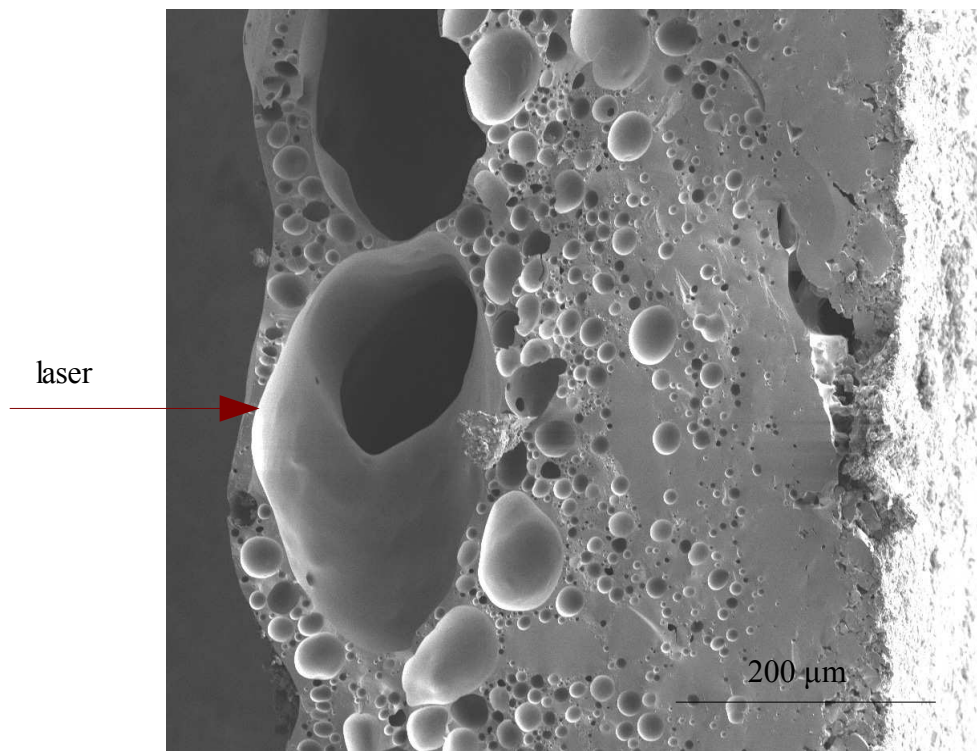
fig.49 SEM picture of the cross-section of the square sintered at (27W, 60mm/s)

Even if the sample seemed to be well sintered, it is clear that the employed energy density was far too high.

The surface in the laser direction is wavy and there are very big drops of glass that were completely melted.

Two big pores, with a diameter between 100 and 200 μm are evident, and this is compatible with the pores observed under the surface in fig.47c.

The penetration depth is about 500 μm, that is also too much, because in the automatic process every layer is only 100 μm.

For this reason an ideal depth should be slightly more than 100 μm, where the part that exceeds is needed only to connect together two adjoining layers.

When the laser penetrates in the material, it is partially absorbed and reflected, so the intensity gradually decreases, until the loose powder can be seen near to the other face of the square.

When a laser beam of intensity I_0 penetrates in the layer, its intensity decreases as follows:

[15] $\dfrac{I_x}{I_0} = 10^{-k\lambda x}$ (Lambert Beer Law)

I_x is the intensity after a x penetration, λ is the wavelength and k is the extinction coefficient.

After the first 100 μm the melted drops start to decrease in size and number.

As already discussed, the pores are probably caused by the polymer burning, but this mechanism is also responsible of the power absorption, that otherwise is difficult, as demonstrated when discussed about the layer sintered without organics.

The measured density (by Archimede) is 1.07 g/cm^3. The laser-sintered material is glassy, so this value has to be compared to the starting glass density, that is 2.35 g/cm^3.

It follows that the layer density is only 45.5% of the theoretical value.

This low density is explained by the closed porosity under the surface and by the presence of some zones of non-sintered material.

A 16.5% of open porosity was measured, due to the non-sintered powder on the side far from the laser.

This is only a little fraction, so the most part (29%) of the porosity is closed.

Another square was analyzed, sintered with a lower energy density, 23W 80mm/s.

The picture in **fig.50** shows that the layer is less thick, about 250 μm, which is still too high for the process but much more suitable compared to the previous sample.

Nevertheless, also in this case the laser interaction causes a lot of big porosity, including many big pores near to the surface, up to 100 μm diameter.
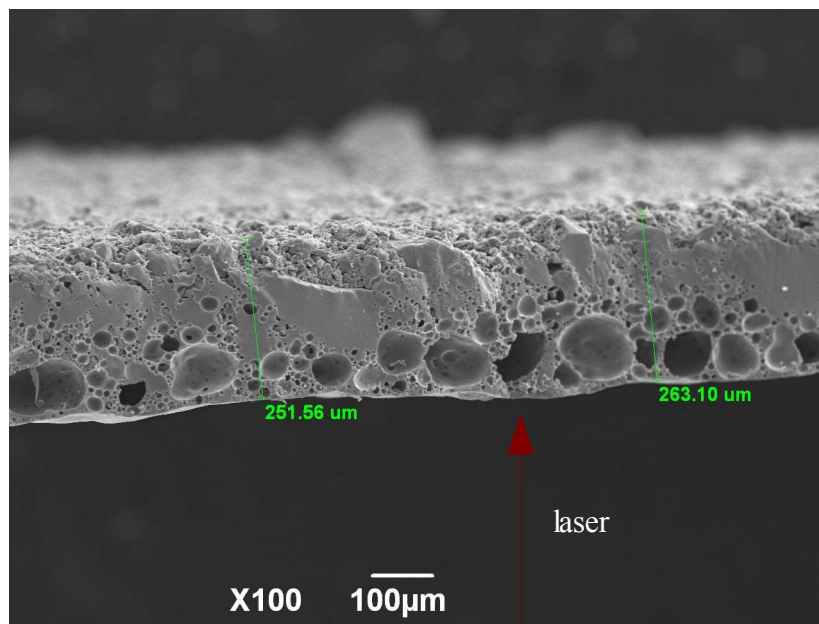
fig.50 SEM picture of the cross-section of the LAS square sintered at (23W, 80mm/s)

In **fig.51** are shown the different parts of the layer:

      1) a zone where there are big bubbles of melted material and big pores

      2) a zone where the particles are quite well sintered together, with low porosity

      3) a zone of partially sintered or non sintered powder, far from the laser source
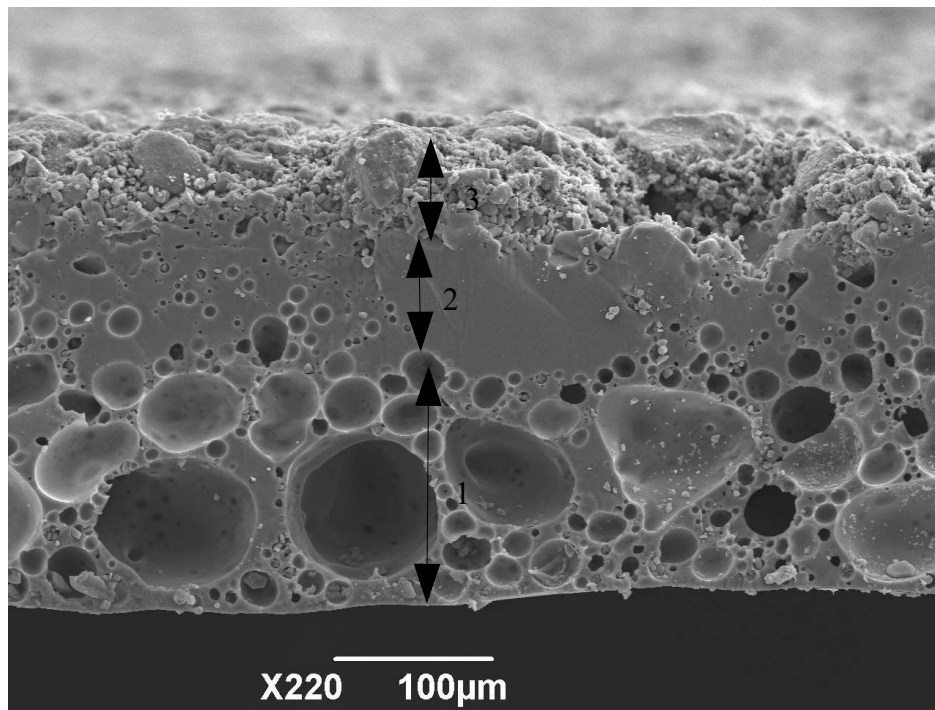
fig.51 SEM picture of the cross-section of the LAS square sintered at (23W, 80mm/s) showing the three zones of sintering

Four squares sintered with different energy density, from low to very high, were analyzed by XRD and the diffractograms are presented in **fig.52**
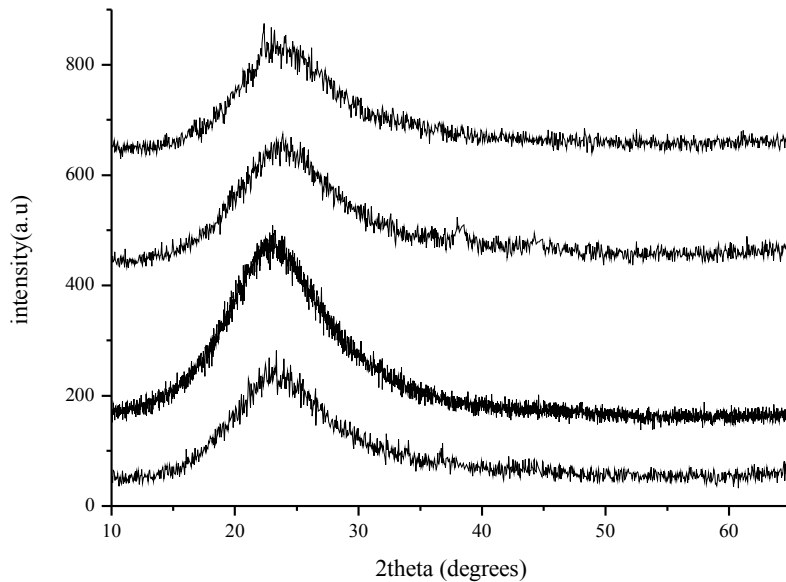
fig.52 Diffractograms of the squares sintered with different parameters

All the samples are amorphous, only in the sample at (35W, 20mm/s) there might be some peak of a crystalline lithium aluminium silicate phase.

Thermodynamically there is enough energy for crystallization, but kinetically there is no time for the new phase arrangement, because the laser heating is very intense but also quick, and the following cooling down happens in few seconds.

This fact however may offer some advantage in the control of the composition: after the sintering the sample can be densified in an oven, and at the same time the crystallization can be controlled, regarding the crystals dimension, amount and structure.

The square was post-sintered to densify in a furnace for 8h at 870°C, heating rate of 2°C/min and non controlled cooling.

The density was increased to 1.51 g/cm3, a value that now has to be compared to the density of the crystallized material (2.48 g/cm^3).

The density so is increased from 45% to 61% of the theoretical density.

3.3.2.2 Silica

Also a silica 1cm x 1cm square sintered with (60W, 100 mm/s) was analyzed at SEM (**fig.53**).

In this case the surface is more smooth compared to the LAS sample, and the laser zone is more homogeneous. The melted drops are less and smaller, and only few small pores are visible.

As the depth increases, there is a transition between a completely melted zone and a zone where the particles are still recognizable but are sintered together by the necks.

Finally, far from the surface, the single "green" particles remain.

The total laser penetration is about 180 μm.

Probably it is still too high, but it can considered acceptable, and actually permits a good connection of the layers, since the same parameters were utilized successfully to build up stable 3D samples.
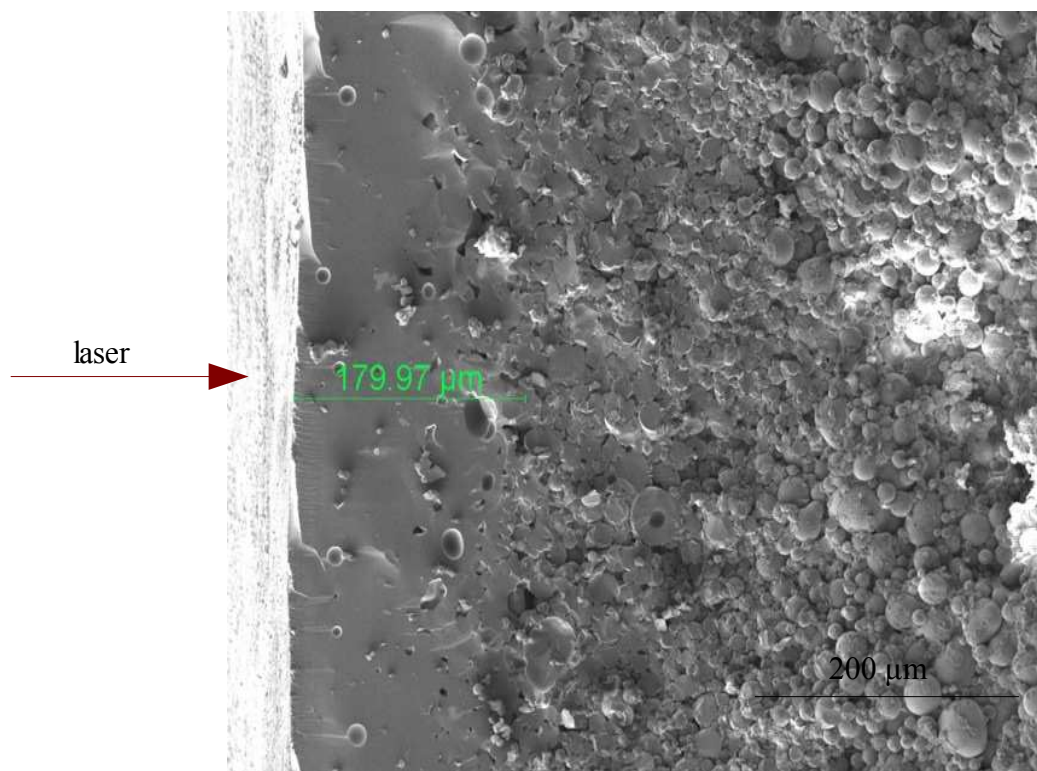
*fig.53 SEM picture of the cross-section of the silica square
sintered at (60W, 100 mm/s)*

3.3.3 Process accuracy

Z-resolution
The minimum z-resolution is determined by the layer thickness. For all the experiments the thickness was set to 100 μm.

This fact causes a ladder effect, as can be observed in fig.54a for a laminated silica object and represented in fig.54b

fig.54a laddered lateral surface of a silica laser sintered sample
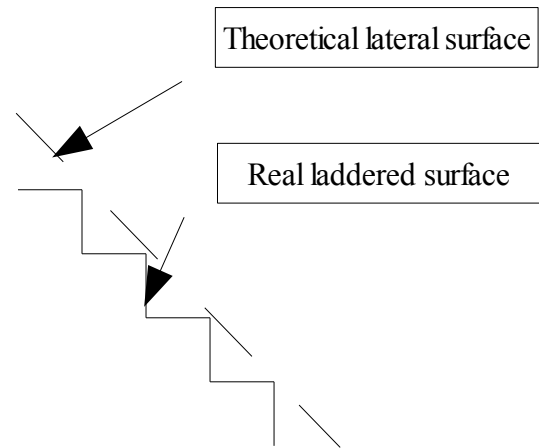
fig.54b

X-Y resolution

In the perspective of building a structure like a scaffold, with very thin walls, it seemed useful to find a correlation between the energy density and the minimum line width.

The resolution in the x-y plane in facts depends on the spot diameter and on the width of the heat affected zone.

3.3.3.1 LAS

To analyze the minimum possible width, the machine program was set to draw just single "geometrical" lines, and their width was measured with an optical microscope, for different powers and scan velocities.

A picture of the sintered layer is shown in **fig.55**
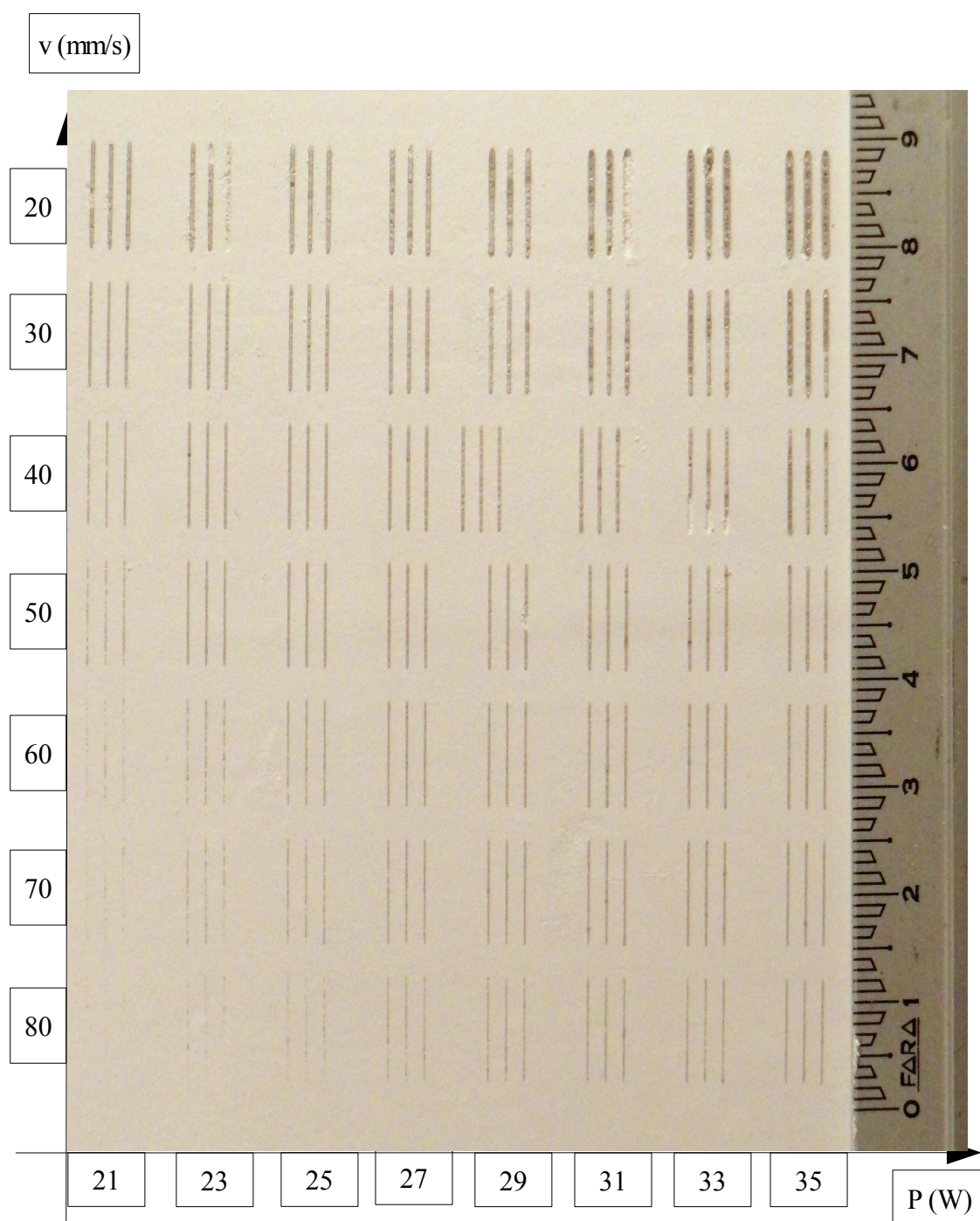
fig.55 lines sintered at different powers and scan velocities

76

As one can expect, the line width increases for increasing power and decreasing velocity, that means for increasing energy density.

Again, the lines in the down-left corner are not well sintered, while the ones in the up-right corner have a rough surface.

This impression is confirmed when the samples are viewed at the optical microscope.

Four picture of some representative parameters can be found in **fig.56a,b,c,d**
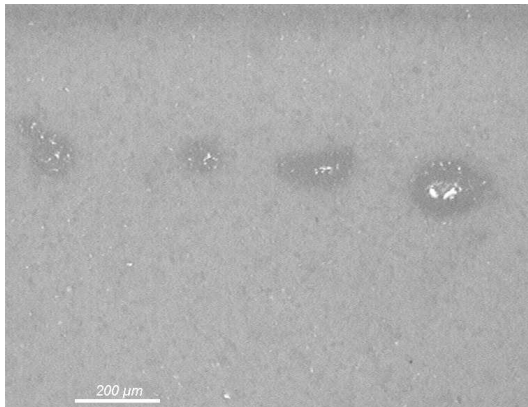
Fig.56a Microscope picture of the line at 23W 80mm/s
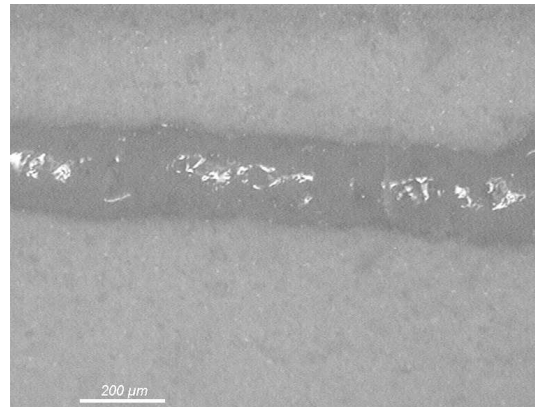
Fig.56b Microscope picture of the line at 27W 60mm/s
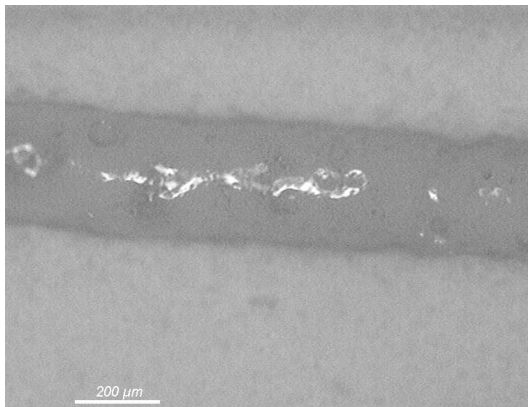
Fig.56c Microscope picture of the line at 23W 30mm/s
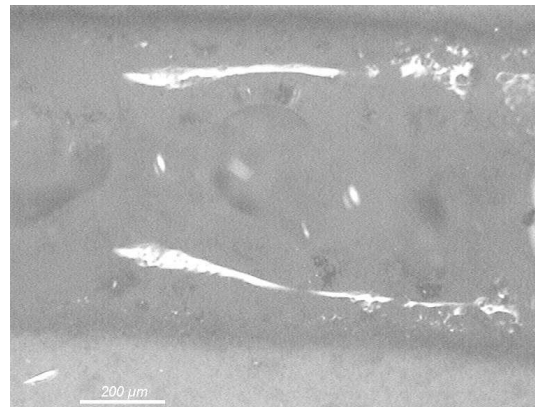
Fig.56d Microscope picture of the line at 35W 20mm/s

Not all the lines are completed, for example in fig.56a; note that this line is sintered with the same parameters used for the square in fig.47b, which instead is completely sintered. This is not particularly surprising, because when an area is hatched, usually the hatch value (100 μm in this case) is lower than the line width, so there is an overlap of the adjacent

lines. The material of an hatched are is then heated more than one time, while it is heated only one time when a single line is sintered.

This observation may be extended easily to the fact that the effect of the laser parameters depends on the sintered area, that means on the wall thickness of the sintered geometry.

The measured width has been plotted (see **fig.57**) vs the laser power for different constant scan velocity.
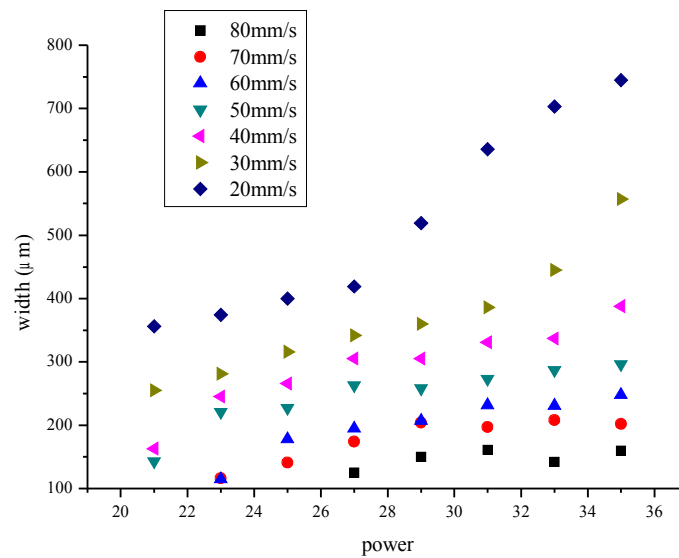
fig.56 width of the line vs laser power for different scan velocities

For high scan velocity the width increases with the power only until 28-30 W, and above this value it remains more or less constant.

This may be explained by the fact that the power transferred to the material is in a way limited by the short time of the interaction.

For lower scan velocities, instead, the behaviour seems to be the opposite: the width at the beginning has a linear dependence on power, until above 28-30W it starts to increase with a higher slope.

A really wide line (up to 700 μm) is obtained with the maximum energy density (fig.56d for example).

The lowest thickness that could be obtained when sintering a complete and constant line is about 200 μm (fig.56c for example); it is displayed that even if the laser spot is 80 μm, the heat affected zone is at least 2-3 times this value.

3.3.3.2 Silica

The silica samples were sintered with a CO_2 laser, which has a spot of 200 μm.

The line width measured with (60W, 100 mm/s) is up to 700-800 μm, so it has to be considered that the wall thickness of a scaffold produced with this machine should be at least 1 mm.

3.4 SAMPLES CHARACTERIZATION

3.4.1 LAS

No 3D parted could be built by laser sintering of LSD, because a further research should be done to optimize the slurry for the automatic process.

The base section of a 3D scaffold however was sintered on a single layer, and the result is shown in **fig.57**
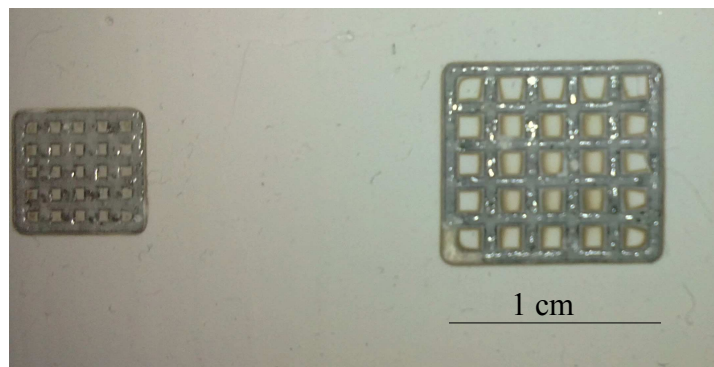
Fig.57 Scaffold sections sintered on an LAS layer

The layer is deposited with the slurry Ls1 and the laser parameters are (25W, 20mm/s).

The grill is composed of just geometrical lines in the CAD file; the cells have a side of 1mm for the small square and 2mm for the big one.

Because of the line width, the cells are actually smaller, and they were measured with an optical microscope.

Two pictures of the big square are presented in **fig.58a,b**. The lines are quite precise even though they don't have a perfectly constant width.

The line width was measured as a mean of 15 values, it is about 670 μm and the mean square side is about 1410 μm. It has to be highlighted that the geometrical value of 2mm is so reduced to 1.4 mm.

This effect may be overlooked for bulk samples of few millimetres dimension, but it has to be taken in account when "drawing" a scaffold with very small lines and cells.

The white spots are the light reflexes that give a glassy appearance to the material, while the dark spots are pores or bubbles.

Unexpectedly however the horizontal lines are wider than the vertical ones, so also the cell sides are not equal.

An aspect ratio of about 1.1 was measured, even if quite variable because the lines are not constant.
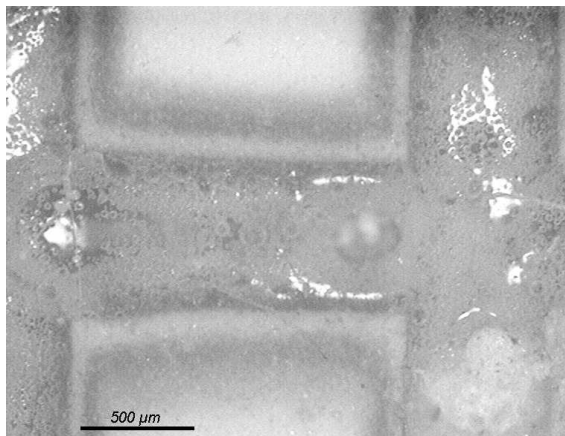
fig.58a Microscope picture of the laser sintered scaffold section on a LAS layer (big square)
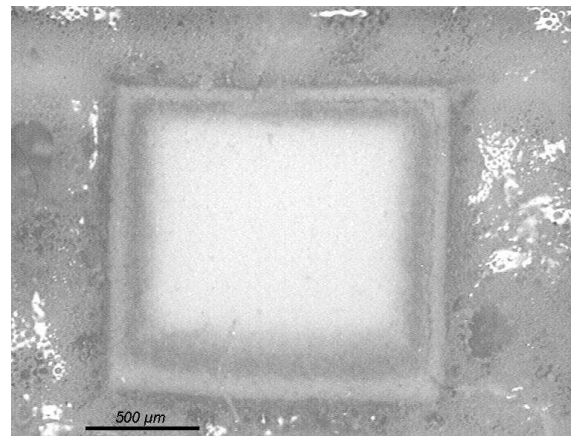
fig.58b Microscope picture of the laser sintered scaffold section on a LAS layer (big square)
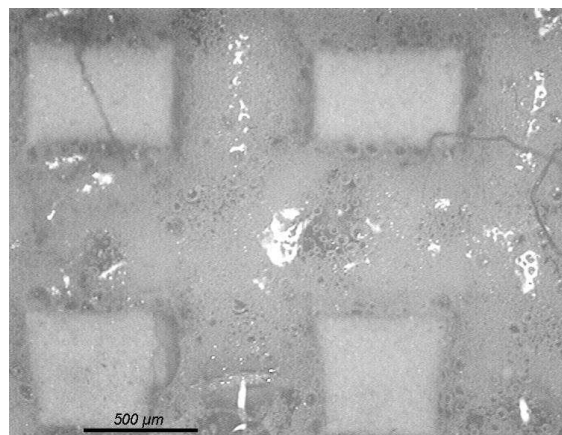
Fig.58c Microscope picture of the laser sintered scaffold section on a LAS layer (small square)

Similar considerations can be done for the small square (**fig.58c**)

The mean line width is 610 μm for the vertical lines and 750 μm for the vertical ones;

the mean cell side is 490 μm (instead of 1mm), with an aspect ratio of 1.2.

A crack is also visible in the corner-left cell of fig.58c, probably caused by the stress induced by the laser heating.

3.4.2 SILICA

The first attempt of producing a 3D scaffold was done with the CAD model in **fig.59**, as a proof of concept of the feasibility of such a complex shape.
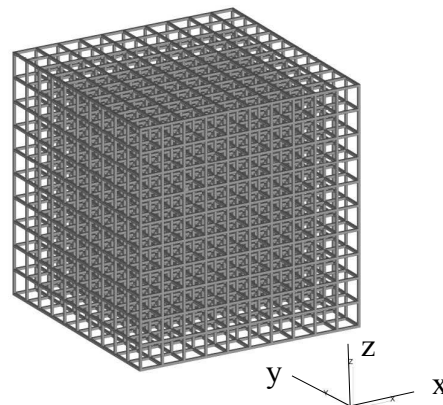
fig.59 CAD model of the silica scaffold

The side of the cube is 2 cm, composed of 10 cells of 2 mm each, and struts that are just geometrical lines.

This is a scaffold with almost the minimum cell size and best resolution possible, since it was noticed that the line width is 700-800 μm.

The laser parameters are the usual, 60W and 100 mm/s.

Only a part of the structure was built, approximatively the first 2 mm height. First the laser sinters the base grid, then the columns, and finally the "second floor" grid.

The part was cleaned in a sonication bath; the silica green layers are particularly difficult to dissolve, so some KOH was added to the bath.

The final result is pictured in **fig.60** and **fig.61**
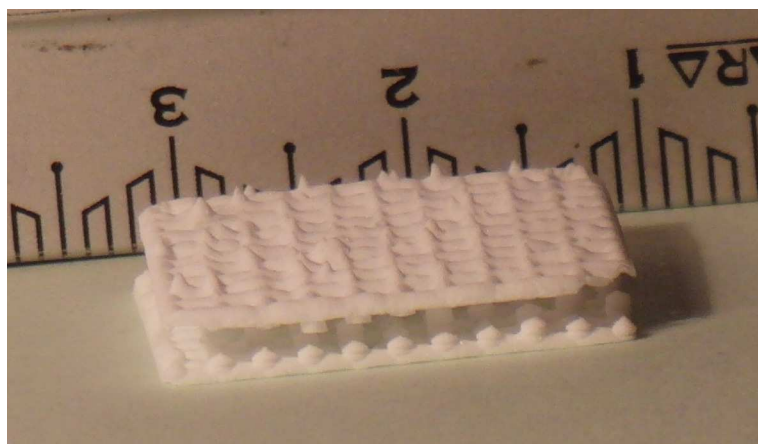
*fig.60 Picture of part of a silica scaffold built using the
model in fig.59*

*fig.61 Picture of the base grid of the silica scaffold.
Unfortunately the columns broke down*

Unfortunately the columns connecting the two parts broke down during the sample removal from the green.

Fig.62 is a picture of the sample taken under a stereoscope, and it can be noticed that in spite of all the grid is quite regular and well sintered, even though the line width is pretty high and so the cell size is quite smaller (~1 mm) compared to the geometrical model (2 mm).
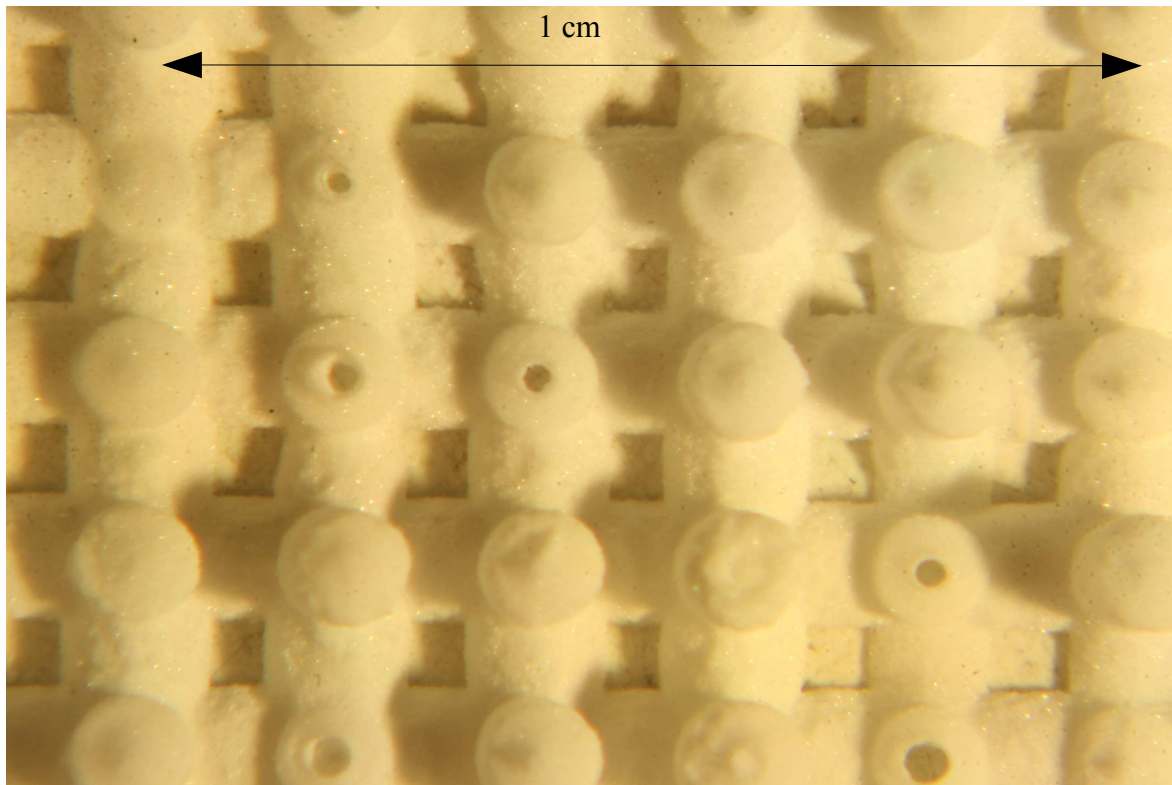
fig.62 Stereoscope picture of the base grid of the silica scaffold and the first columns

The columns are circular instead than square because the point of intersection is really small, so the laser sinters just a spot.

Anyway it was basically proved that it is possible to sinter this structure, even if when the columns are so thin it is too easy to break them while removing the part.

The following experiments so were carried out with a more tough structure, a cube of 1 cm^3 side, and 3x3x3 cells with a side of 2 mm (**fig.63**)
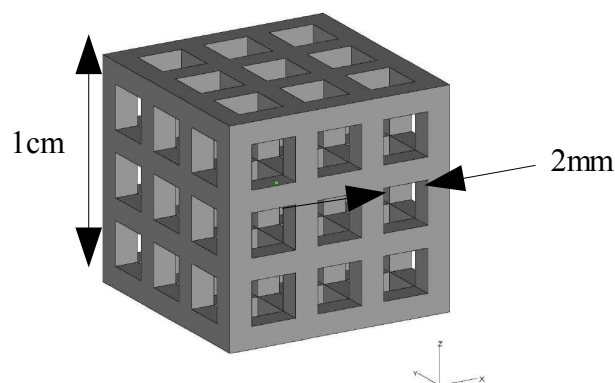
fig.63 silica scaffold CAD model1

Also this model was partially built up with silica, and the sample is shown in **fig.64** (side

view) and **fig.65** (from the top)
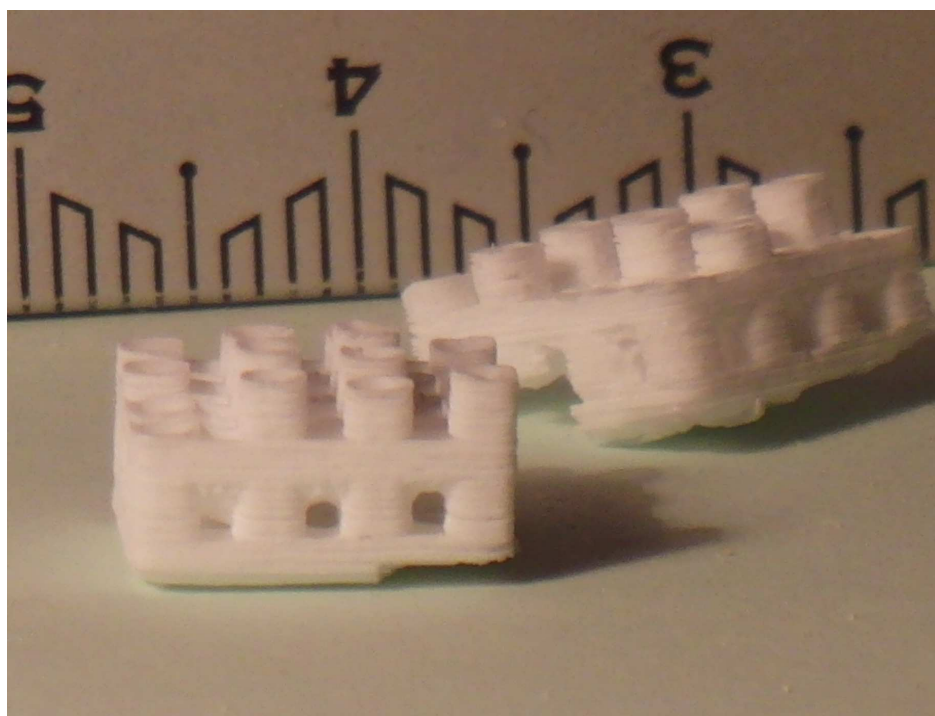
*fig.64 side view of a silica scaffold produced by laser sintering of LSD*
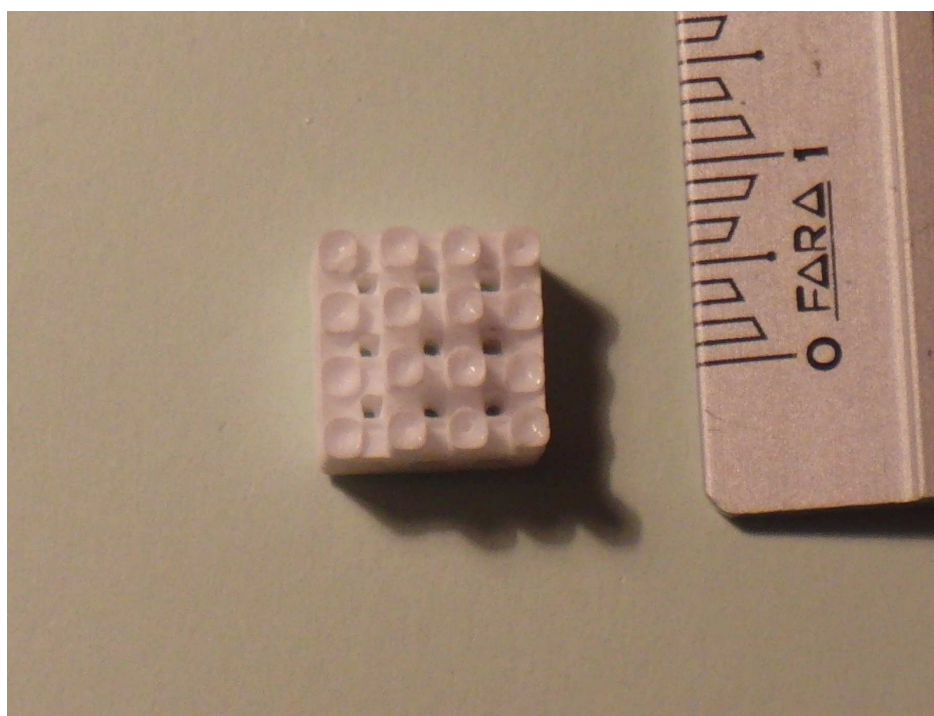
fig.65 top view of a silica scaffold produced by laser sintering of LSD

This time the sample did not break, but the building just stopped after the first 60 layers.

While overall the object has a good quality, it is evident that the accuracy and the surface finish in the x-y plane is much better than along the z-axis.

This happens because near to a free edge two adjoining layers are never perfectly joint, and there is always some delamination.

Pictures taken under the stereoscope give a better view of the upper surface (**fig.66a**) and the side surface (**fig.66b**); the accuracy and the surface finish are much better in the x-y plane than along the z-axis.
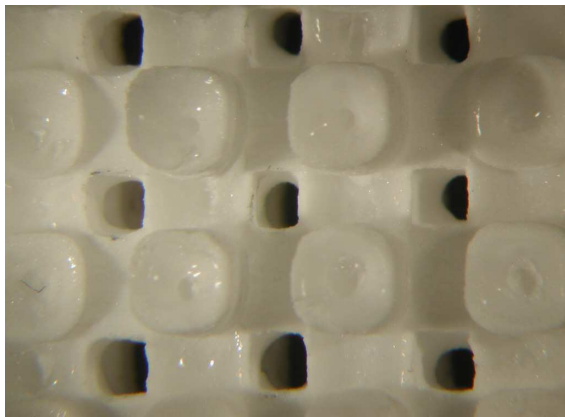
fig.66a stereoscope picture of the top view of the silica scaffold
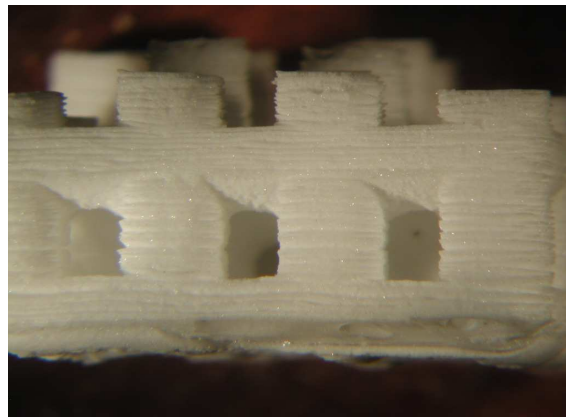
fig.66a stereoscope picture of the top view of the silica scaffold

In an attempt to investigate better this feature, the side surface of the sample was examined under an SEM microscope (JEOL JSM-6490).

The pictures reveal a laddered surface as expected: at the end of each layer, only the surface that was exposed to the laser is well sintered, while the rest of the layer thickness was not sintered or broke because it was too fragile.

A cubic cell can be observed in **fig.67** and a column in **fig.68** where also the layers disposal is evident.

A picture of the layers at higher magnification is in **fig.69**: it is confirmed that the layer distance is 100 μm, but also that only a thin surface has been sintered, or at least partially sintered.

The gap between two layers was filled of unsintered material, that was therefore washed out during the cleaning.
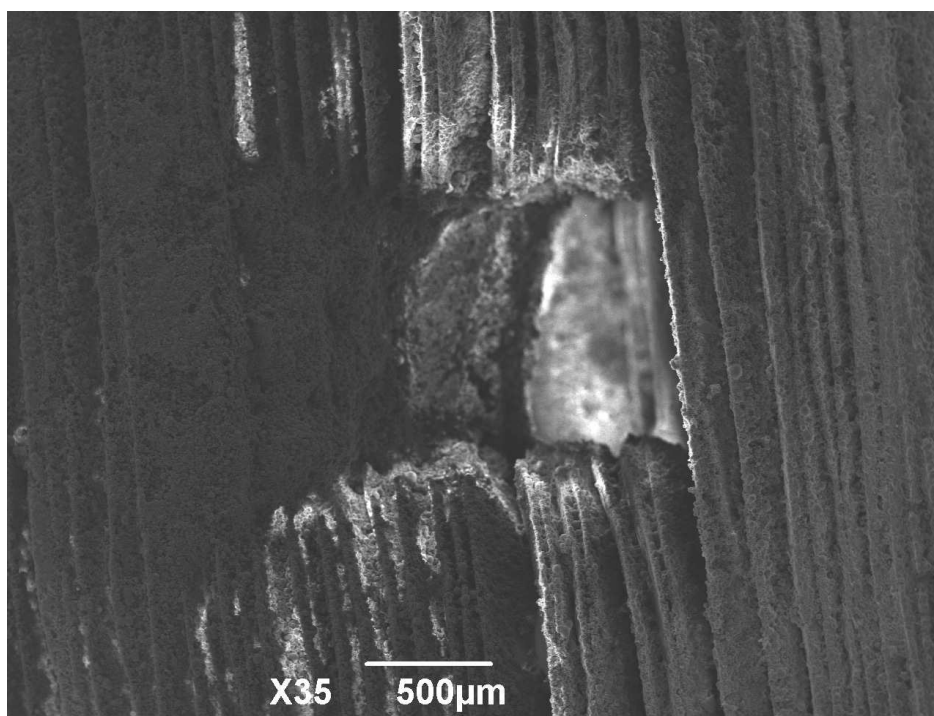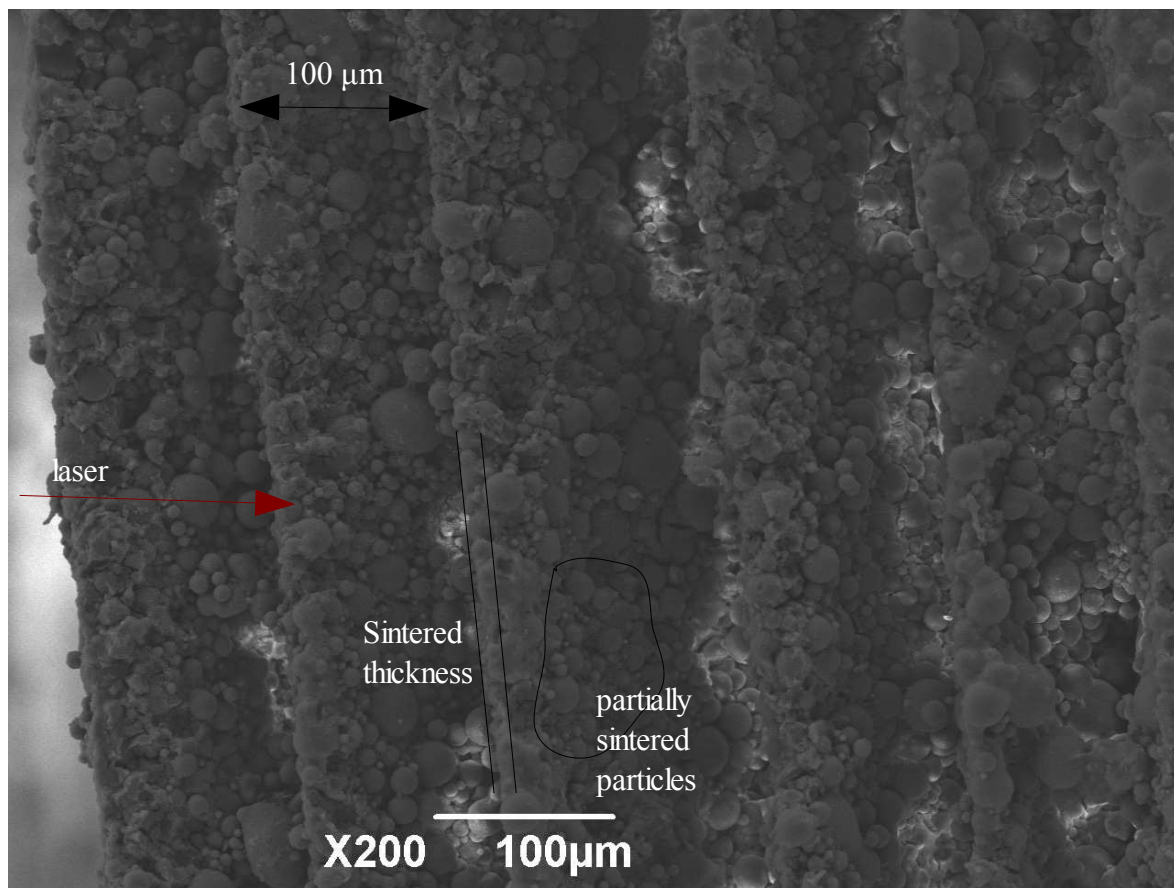
*fig.67 SEM picture of the side view of a cell, showing the laminated structure*
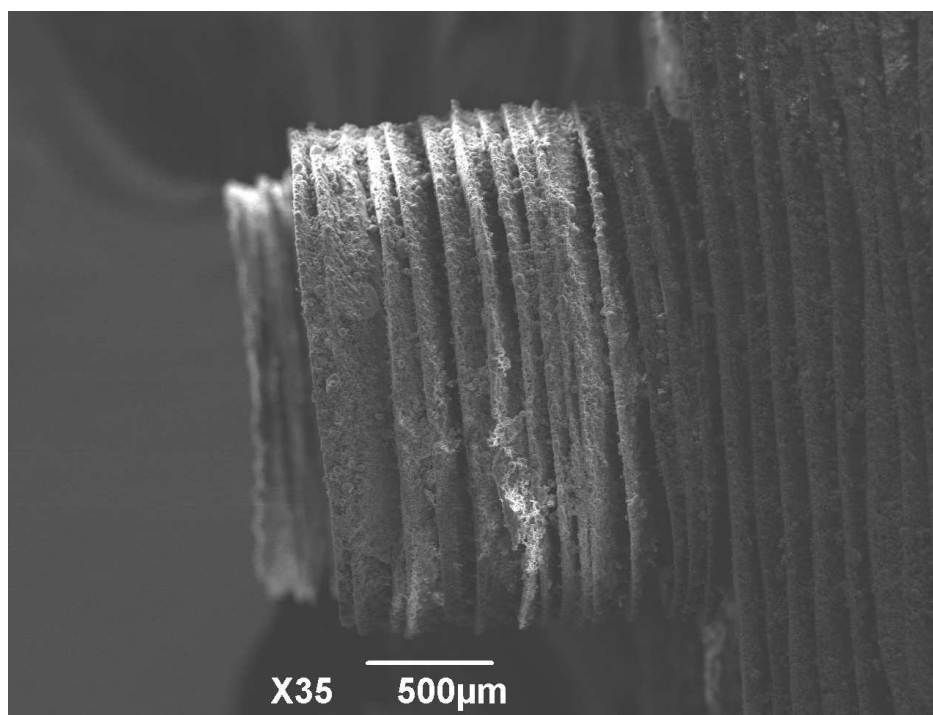
fig.68 SEM picture of the side view of a silica column, showing the laminated structure

Far from the edge, instead, all the layer thickness is at least partially, in a way that two layers are welded together in some points (**fig.70**), ensuring a minimum mechanical strength to the object.

fig.69 SEM picture of the silica layers; the layers are not well joint together near to the edge
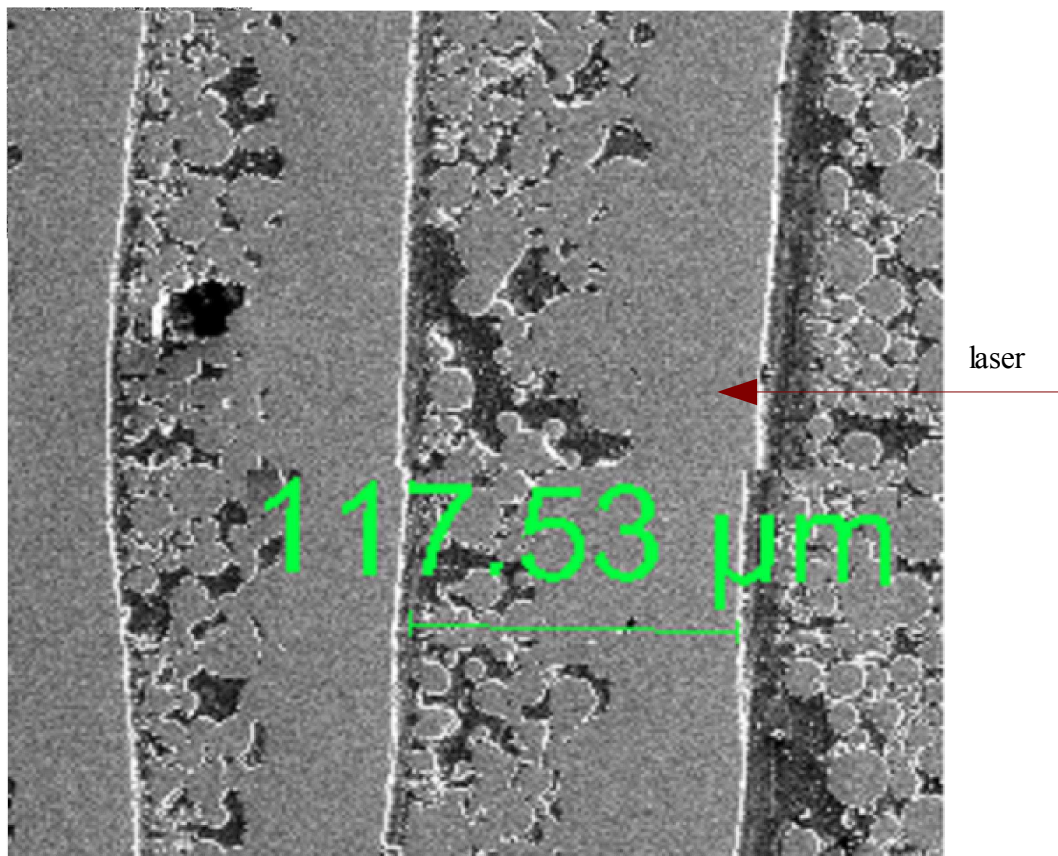
Fig.70 SEM picture of the inside of the silica structure, where the layers are joint together

The first part of the layers is perfectly densified, but then there is a zone of partial sintering where some porosity is left.

This picture in fig.70 was taken from a polished cross-section of the sample in **fig.71**, laser sintered with the same parameters as the scaffold
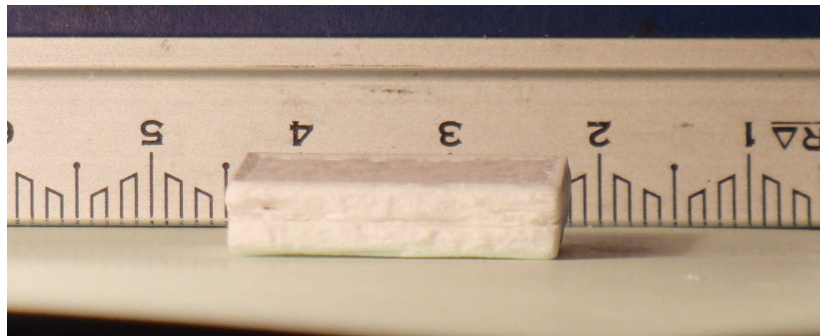
fig.71 silica sample produced by laser sintering of LSD

For this specimen was measured a density of 1.76 g/cm^3 (80% of the theoretical density), with a densification respect to the green body (1.57 g/cm^3), and a decrease of the open porosity from 27.5% to 16.3%.

For the scaffold in fig. instead the density is only 1.59 g/cm3, and also the open porosity is similar to the green (24.2%).

In facts, of course the laser treatment causes a densification also in the scaffold, but the border effect, that causes the laddered lateral surface as shown, causes a lot of porosity too. This effect is present also in the simple object of fig.71, but the scaffold has much more surface compared to the volume, so the effect is more relevant.

CHAP 4: 3D PRINTING

Similar scaffold structures were produced by 3D printing at BAM institute in Berlin, with the same LAS glass-ceramic powder used for laser sintering.

The 3D printer is a Prometal RX Series (Germany), the basic working principle being described in section.1.5

Two CAD models were utilized, the first is the same of fig.63 (Model1), and the second (Model2) is in **fig.72**, a 0.9 x 0.9 x 0.9cm cube but with with four 1mm cells for each side.
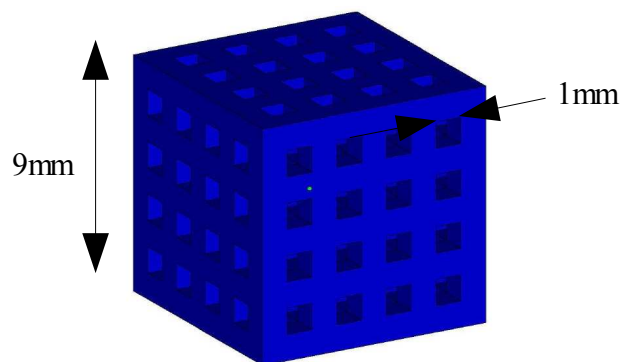
fig.72 CAD Model2 of a scaffold for 3D printing

4.1 Qualitative analysis

Different experiments with different parameters were carried out.

The two powders employed have been characterized in section 2.3.2, LAS3 is the finest and was sieved under 125 μm, LAS4 is bigger and was sieved under 200 μm.

Easily, LAS3 will be indicated as 63-125 μm and LAS4 will be indicated as >125 μm.

The parameters used for the experiments are summarized in **tab.8**.

Clearly, when the powder >125 μm is used, the layer thickness must be at least 200 μm.

The passes are related to the amount of binder droplets per pixel, where the standard parameter is 10 print passes/jet spacing.

Increasing the number of passes the amount of binder is increased, that reasonably leads to better packing and higher green density.

	CAD	powder	Layer thickness (LT)	Passes (P)	Time (DT)	result
A	2	>125	200 μm	10	60 s	failed
B	1	63-125	100 μm	10	60 s	failed
C	2	63-125	100 μm	10	60 s	distorted
D	1	>125	200 μm	10	60 s	ok
E	1	>125	200 μm	20	120 s	ok
F	1	63-125	80 μm	15	60 s	ok
G	1	63-125	100 μm	20	300 s	ok

Tab.8 parameters used for the LAS samples built by 3D printing

The DT time instead is the time between the printing of one layer and the following.

In this time the powder is heated (usually around 80°C) to partially cure the polymer;

the cure is later completed out of the machine at 125°C for one night.

Again, reasonably, the more time is set for the cure, the more the resin hardens.

The last column of the table refers to the final aspect of the sample, if broken or distorted in case the process does not give the expected result.

In **tab.9** is summed also the heating treatment, that consists of 1) complete the cure of the binder 2) binder burnout 3) sintering (and crystallization in the case of the glass-ceramic).

|	Cure T / time	Heating rate	Dwell T/time binder burnout	Heating rate	Dwell T/time sintering	Cooling
A	125°C/ 1night	120K/h	400°C/1h	120K/h	870°C/8h	uncontrolled
B	125°C/ 1night	120K/h	400°C/1h	120K/h	870°C/8h	uncontrolled
C	125°C/ 1night	120K/h	400°C/1h	120K/h	870°C/8h	uncontrolled
D	125°C/ 1night	120K/h	400°C/1h	120K/h	870°C/8h	uncontrolled
E	125°C/ 1night	400K/h	300°C/1h	300K/h	860°C/8h	uncontrolled
F	125°C/ 1night	400K/h	300°C/1h	300K/h	860°C/8h	uncontrolled
G	125°C/ 1night	400K/h	300°C/1h	300K/h	860°C/8h	uncontrolled

Tab.9 Heating treatment for the LAS samples built by 3D printing

The printing of **sample A** failed because the columns and the cells of the CAD2 are too small to be built with the powder > 125 μm; the consequence is that the cells were filled with powder.
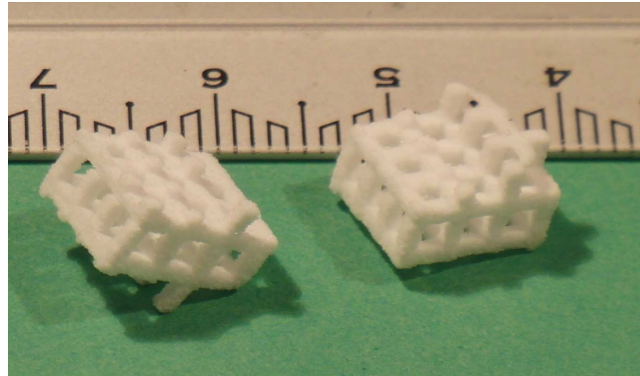
Sample B on the other side was printed with the finer powder and the bigger model (CAD1); in this case basically the structure could be printed, but the layers started to shift,

so the scaffold broke at a certain point (green sample in **fig.73a**, sintered in **fig.73b**).
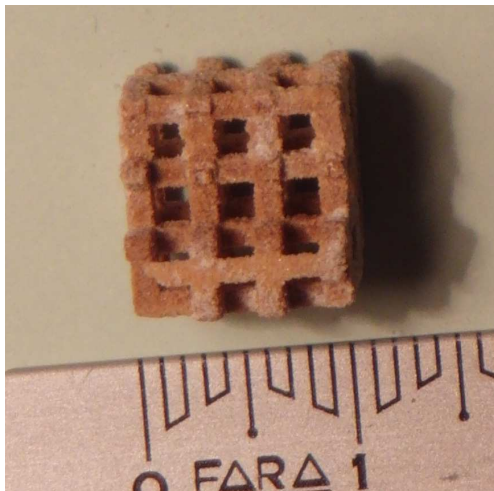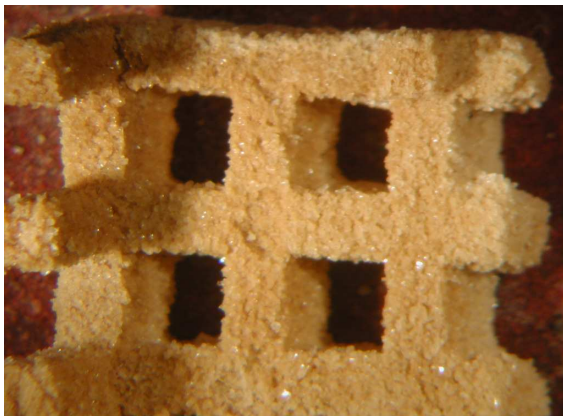

*fig.73a LAS Scaffold B by 3D
printing, green*

*fig.73b LAS Scaffold B by 3D printing, after
sintering*

A magnified image of the green sample can be seen under the stereoscope, at 6.4X (**fig.74a**) and 16X (**fig.74b**), showing that the structure is formed of grains of powder, connected only by the binder.

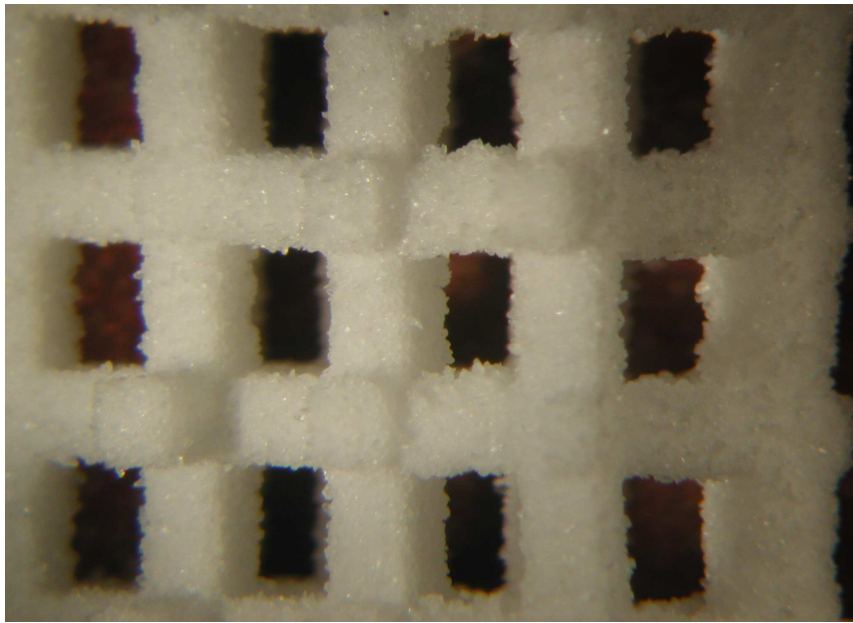
*fig.74a Stereoscope picture of the green
sample B (6.4X)*

*fig.74b Stereoscope picture of the green
sample B (16X)*

In fig.74a, a crack in the top-left corner is visible, where there is the connection of the struts and the column, that is the weakest point of the scaffold.

The sample after sintering and crystallization appears as in **fig.75** (stereoscope 6,4X), where the grains are still visible but now are directly connected each other.

The nature of this bond will be better investigated with SEM in the next section.

fig.75 Stereoscope picture of the sintered sample B (6.4X)

A similar problem of shifting happened with **sample C**, using the fine powder and the other model (CAD2).

In this case the object did not break, but it was skewed because of this shifting of the layers. In facts, the 63-125 μm powder is less flowable than the bigger one, so when a new layer is spread by the roller, if the previous layer is not bonded strongly enough, it tends to be shifted, resulting in a structure like **fig.76a** (green) and **fig.76b** (sintered).
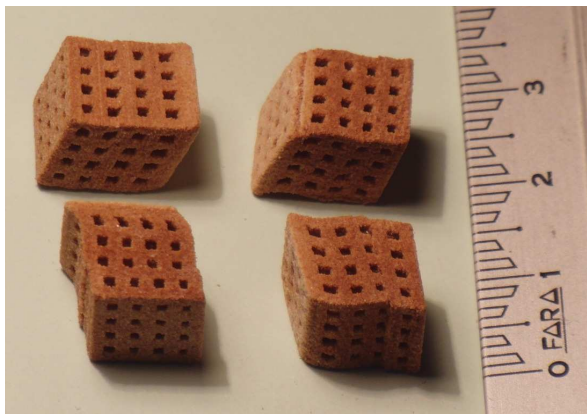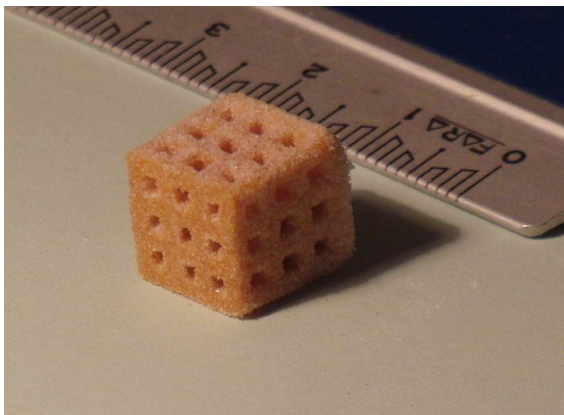

fig.76a LAS Scaffold C by 3D printing, green
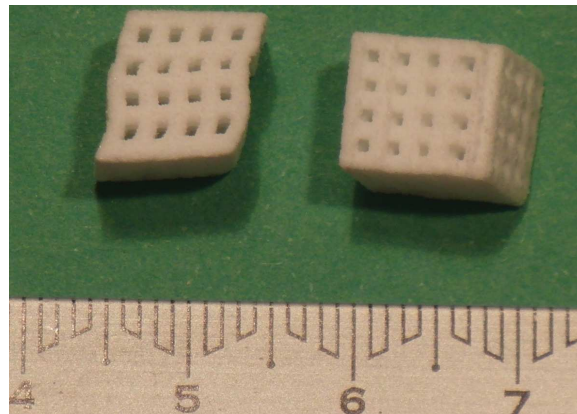
fig.76b LAS Scaffold C by 3D printing, sintered

The powder > 125 μm has a better flowability, so the model CAD1 was easily printed without distortions (**sample D**)
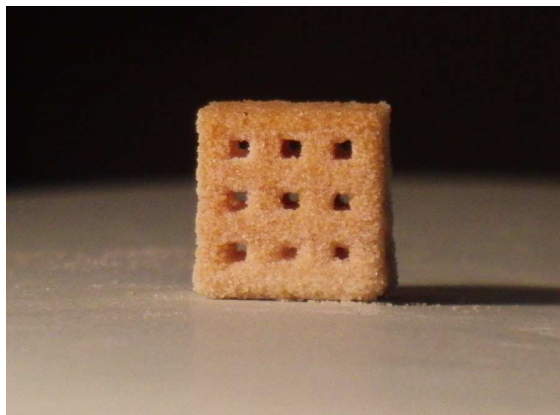
On the other hand, this powder is quite big, so the accuracy and the surface finish are much

better with the other powder, both because of the powder size itself and because of the doubled layer thickness.
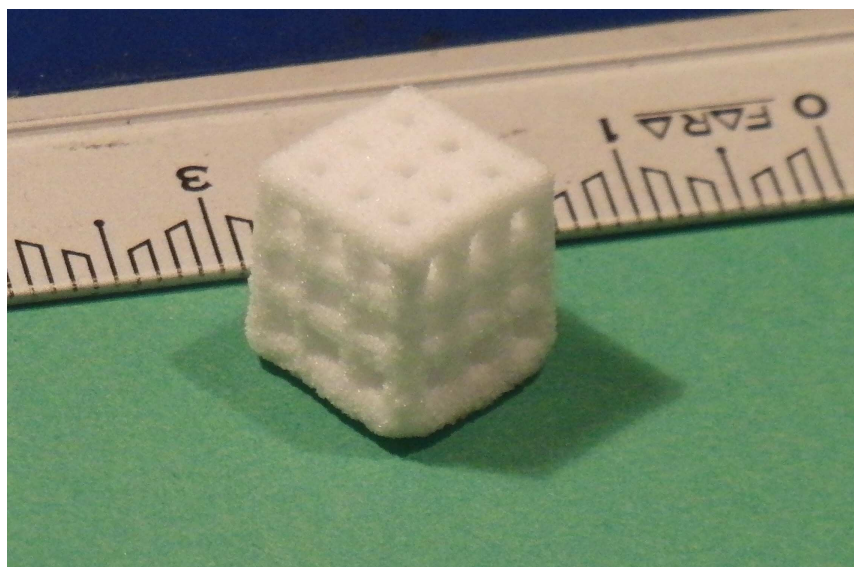
The printed scaffolds are shown in **fig.77a,b** (green) and **fig.78** (sintered).

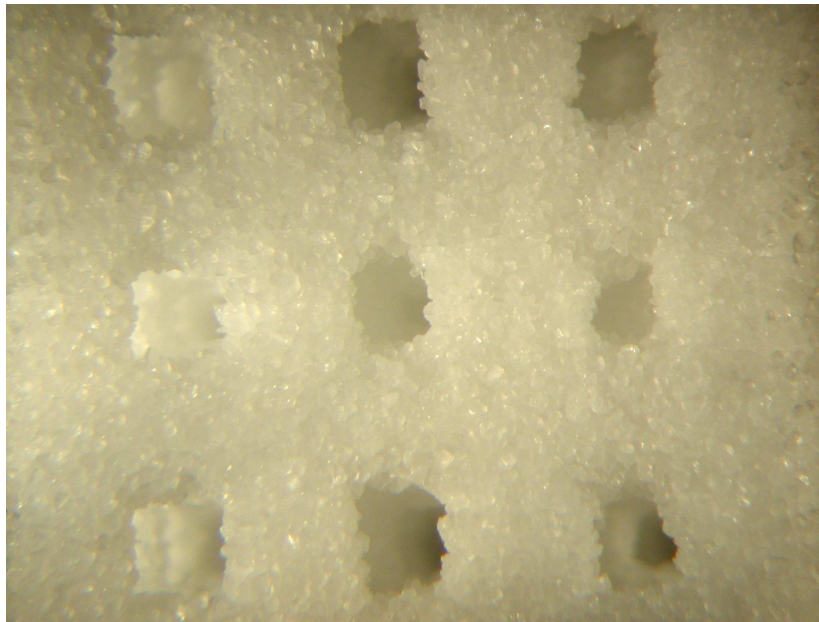*fig.77a LAS Scaffold D by 3D printing, green*

fig.77b LAS Scaffold D by 3D printing, green

fig.78 LAS Scaffold D by 3D printing, sintered

Despite the fact that the complete scaffold could be printed and sintered, the surface is rather rough and the cells are not printed very precisely, as it is observed under the stereoscope (**fig.79,** 6.4X).

94

*fig.79 Stereoscope picture of the sintered sample D (6.4X)*

This same sample was reproduced with same powder but different parameters (**sample E**, LT= 200 μm, DT= 120s, P= 20).

Increased curing time and passes provide a higher green density and better accuracy, even though this is however limited by the big grain size and layer thickness.

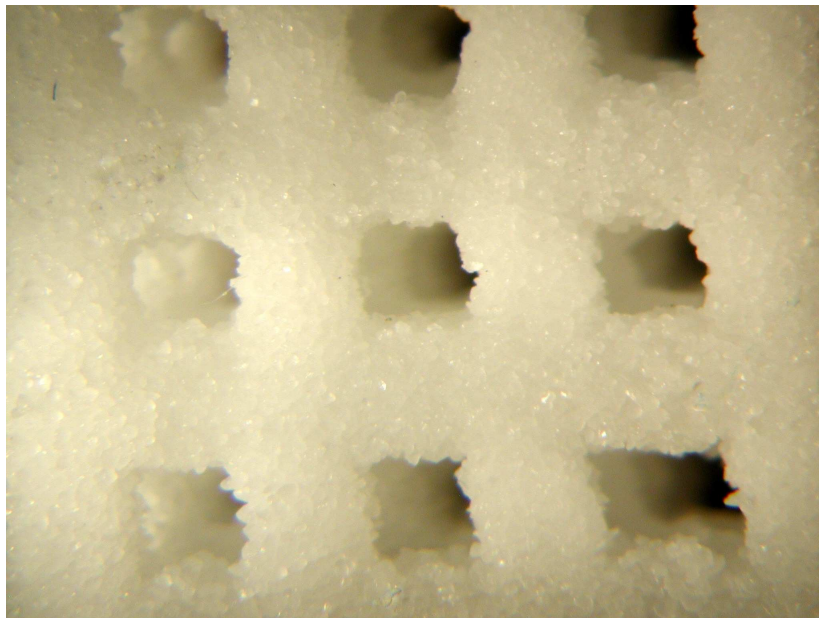The printed and sintered sample is pictured in **fig.80a,b**
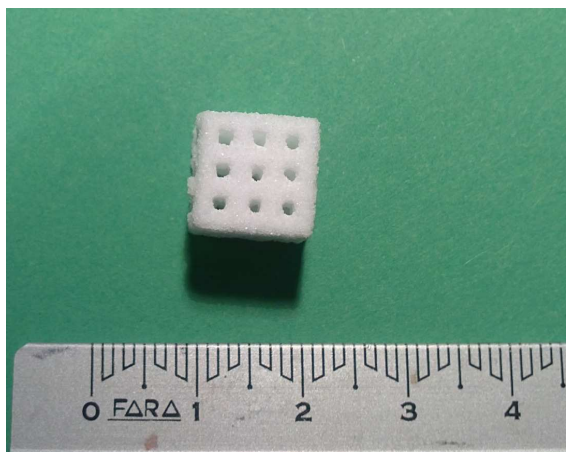
fig.80a LAS Scaffold E by 3D printing, sintered
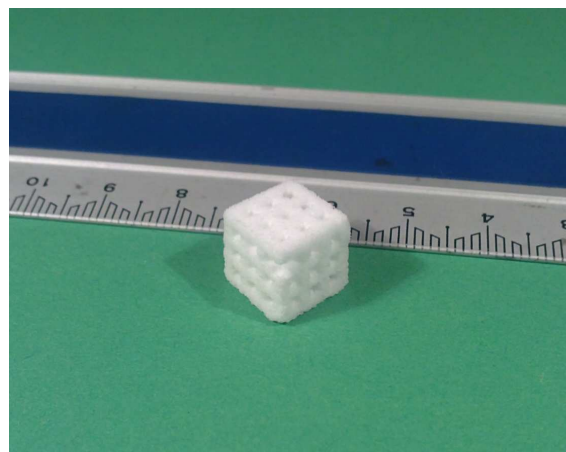
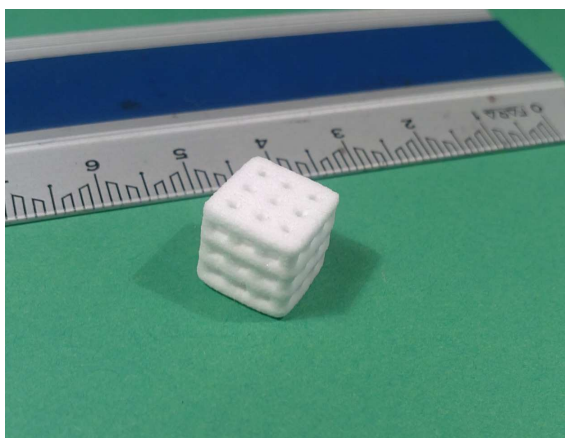*fig.80b LAS Scaffold E by 3D printing, sintered*

Also this sample was seen under the stereoscope (**fig.81**, 6.4X), demonstrating that some improvement was achieved, since the powder seems more packed and the cells are more open.

fig.81 Stereoscope picture of the sintered sample E (6.4X)

However this powder is probably too big to achieve a good accuracy, so the parameters were changed to have better results with the fine powder 63-125 μm.

Firstly was set DT= 60s, P=15, LT= 80 μm (**sample F**), and actually a non-distorted sample could be printed and sintered (**fig.82a,b**).

fig.82a LAS Scaffold F by 3D printing, sintered
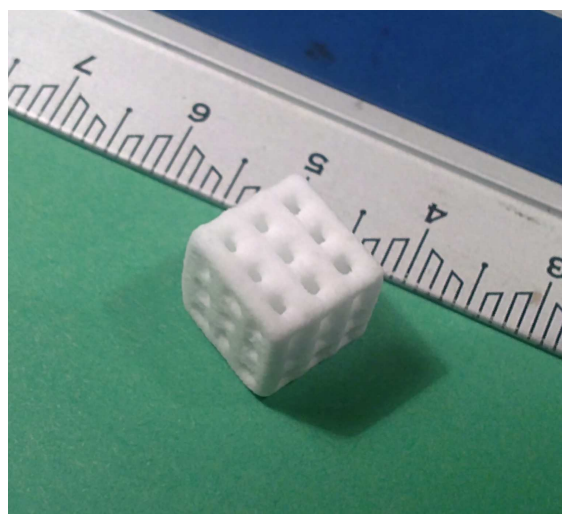
fig.82b LAS Scaffold E by 3D printing, sintered

Likely, the increased time and number of passes provided a better stability of the green

layers, thus avoiding the shifting that was found in sample C.

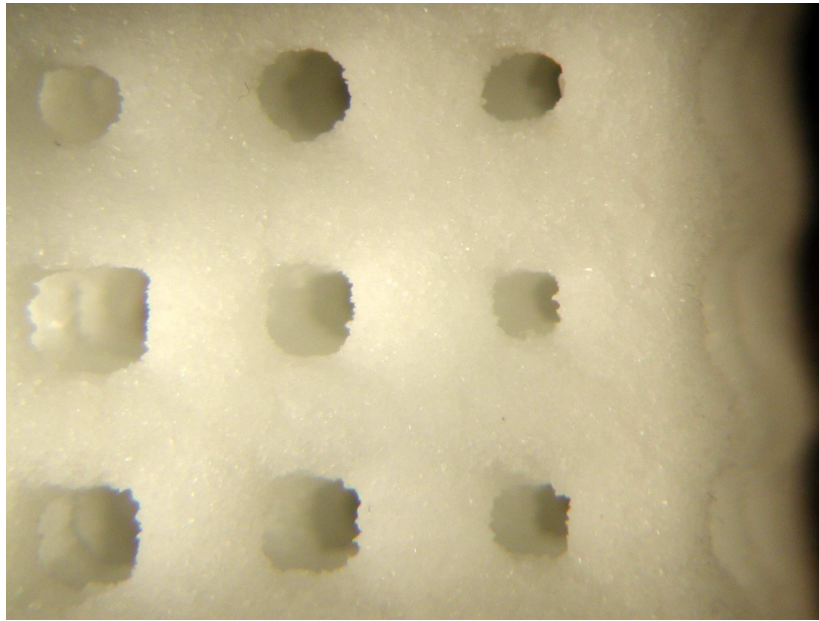Even though the shape of this sample is regular, the cells are quite well defined and the surface appears smooth, there are still some imperfections. The lateral surfaces are wavy, and the cells in the upper and bottom plane are smaller than the others and circular instead than squared (stereoscope picture in **fig.83**, 6,4X).

fig.83 Stereoscope picture of the sintered sample F (6.4X)

For **sample G** was set DT= 300s, P= 20, LT= 100 μm and with these parameters the best result was obtained.
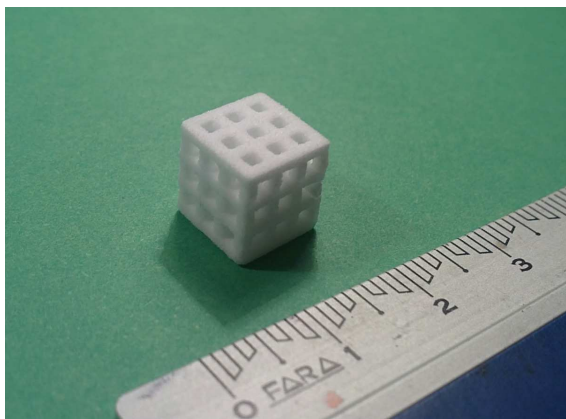
fig.84a LAS Scaffold G by 3D printing, sintered
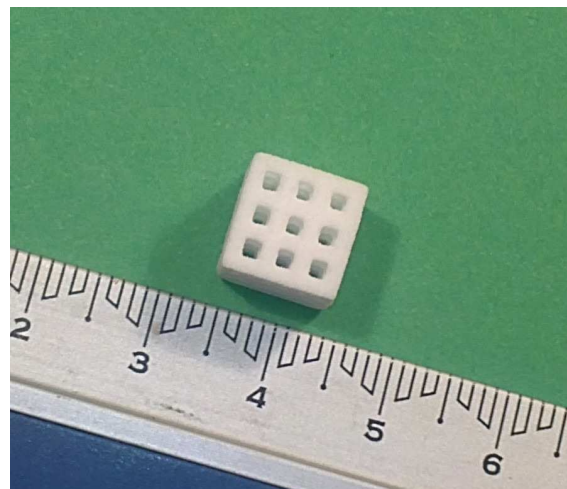
fig.82b LAS Scaffold F by 3D printing, sintered

Fig.84a,b shows a picture of scaffold G, that seems to have the best surface finish and the best accuracy. In facts the cells have a very regular, squared shape and the side surfaces are similar to the top and the bottom.

The pictures under the stereoscope show the lateral surface (**fig.85**) and the upper surface (**fig.86**) of this scaffold.

The accuracy is similar for the two planes, and the layered structure can not be recognized.

This highlights a remark about the comparison between laser sintering and 3D printing:

with laser sintering the best x-y accuracy and surface finish can be achieved, but the side surfaces along z-axis are rough; on the other side with 3D printing the accuracy is lower, but usually there is not a big difference depending on the direction.

This seems to be quite general for the processes, even though two different materials were examined, so the comparison is not easily predictable.
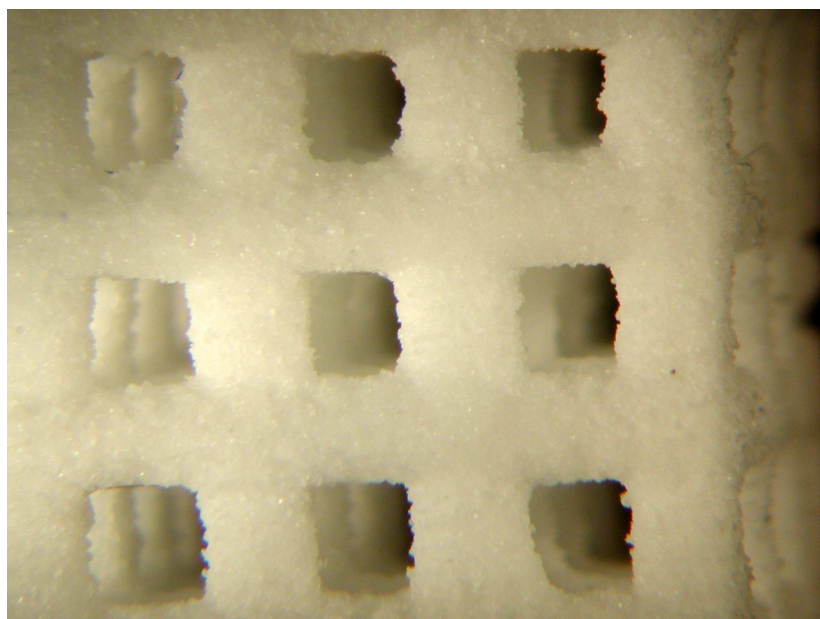
Fig.85 stereoscope picture of the lateral surface of LAS scaffold G
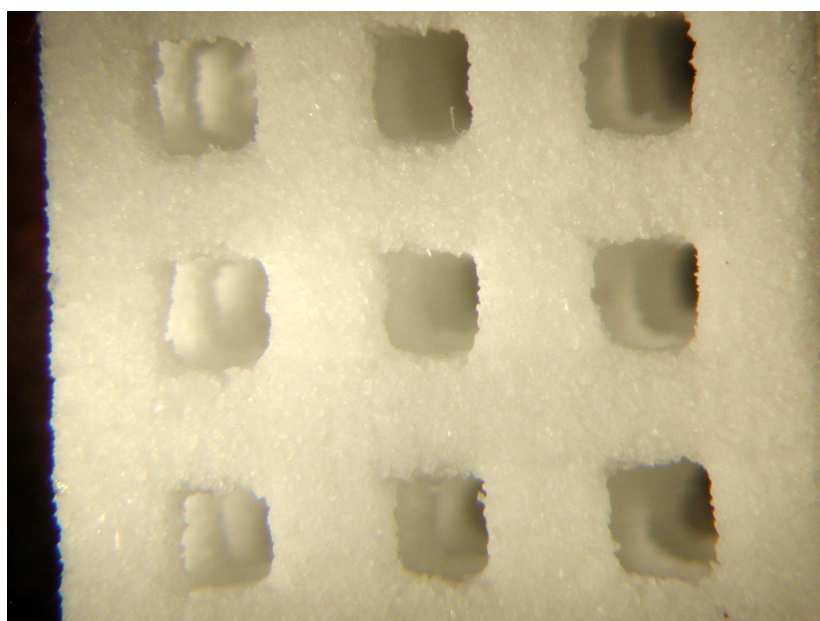
Fig.86 stereoscope picture of the top surface of LAS scaffold G

98

4.2 Microstructure analysis

For an investigation on how the particles are kept together and on the microscostructure, the samples where observed under the SEM.

First of all a part of the green body of sample B was examinated. **Fig.87** shows a broken column that at higher magnification reveals the cross section of the binder drops that bonded the particles before the fracture (**fig.88**).
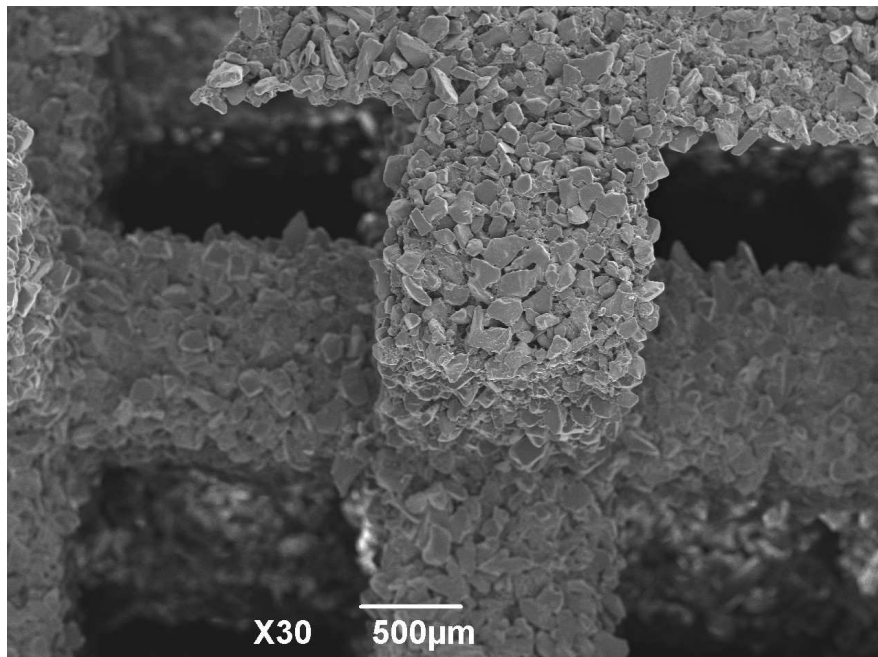
fig.87 SEM picture of the green sample B
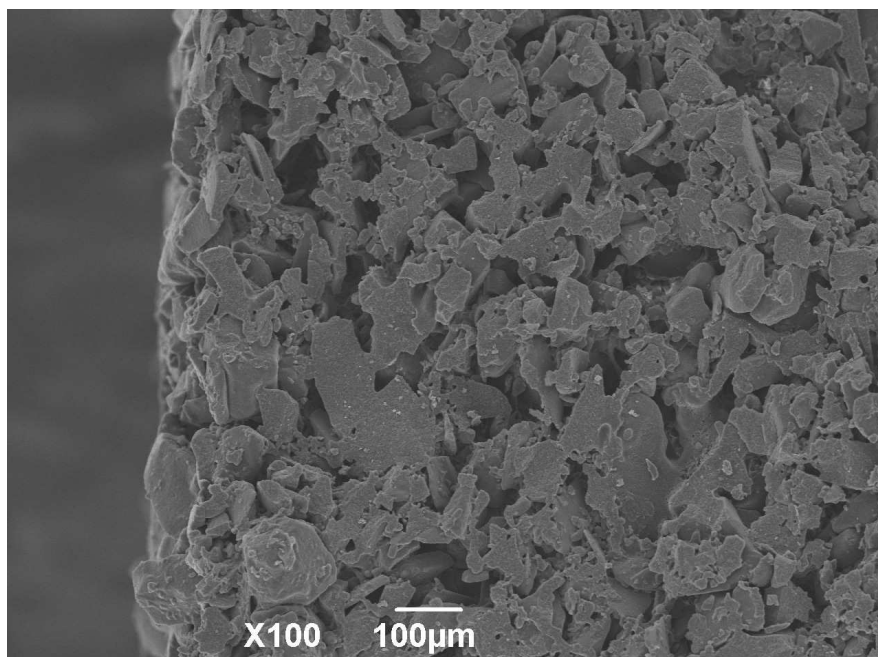
fig.88 SEM picture of green sample B, showing the drops of resin binding the powder

There is a lot of porosity in the gaps between the particles, because the powder was not pressed.

Fig.89 shows in detail a drop of binder connecting two particles.
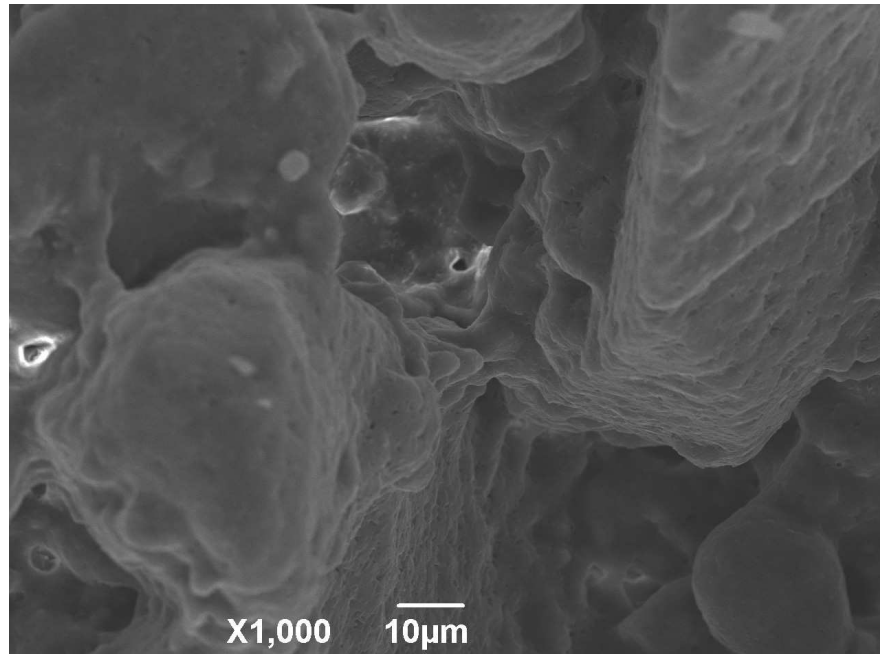
fig.89 SEM picture of a drop of binder connecting two LAS particles

After the heating treatment the binder is burned and the particles sinter.
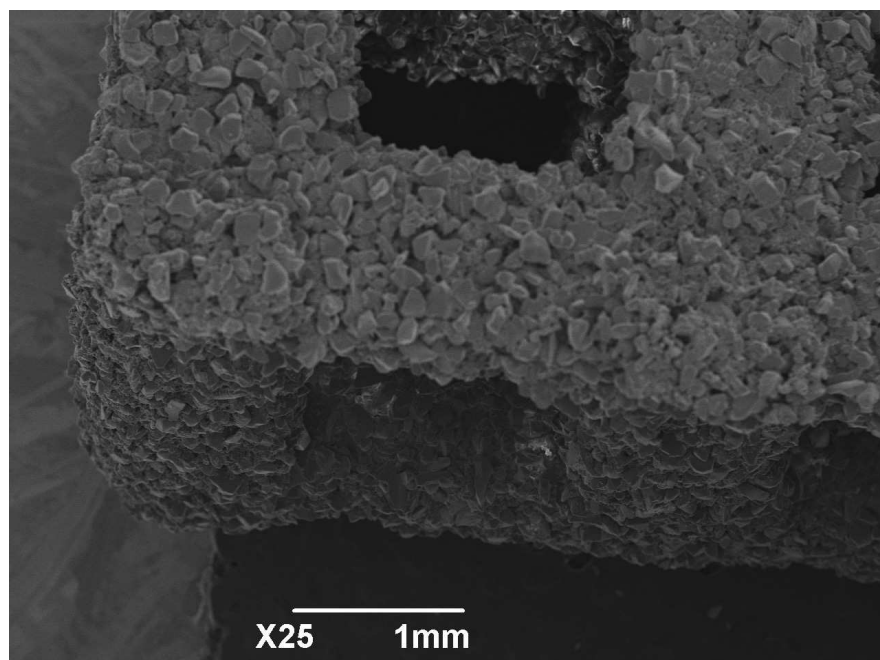
fig.90 SEM picture of sample B after sintering

fig.90 and **fig.91** are pictures of parts of sample B after sintering and crystallization.
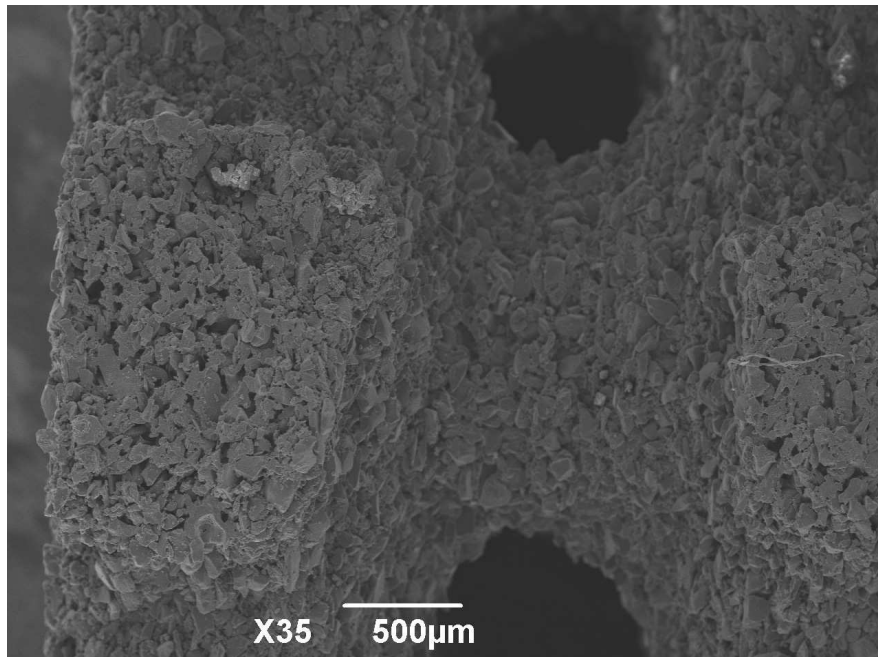
fig.91 SEM picture of sample B after sintering

The single particles are still noticeable, but now are partially sintered together, as in **fig.92**
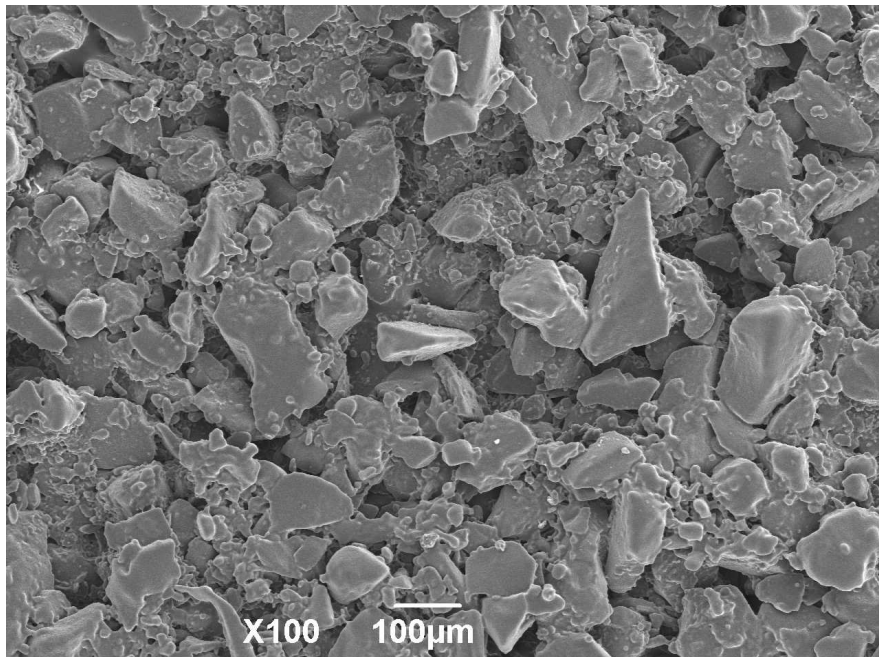
fig.93 SEM picture of the LAS4 particles partially sintered together

Sample E was also examined, and a fracture surface can be seen in **fig.94**.

As one can easily see, this sample has bigger starting particles, resulting in a more rough structure.
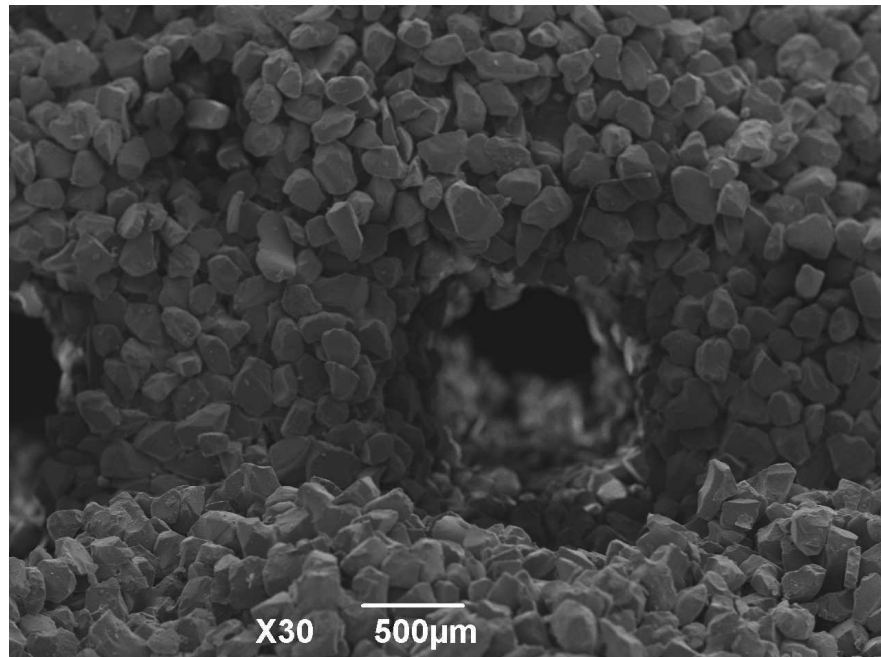
fig.94 SEM picture of a fracture surface of sample E

The big particles does not seem to be sintered together, but at higher magnification (**fig.95**) it can be noticed that the grains are connected in some points.
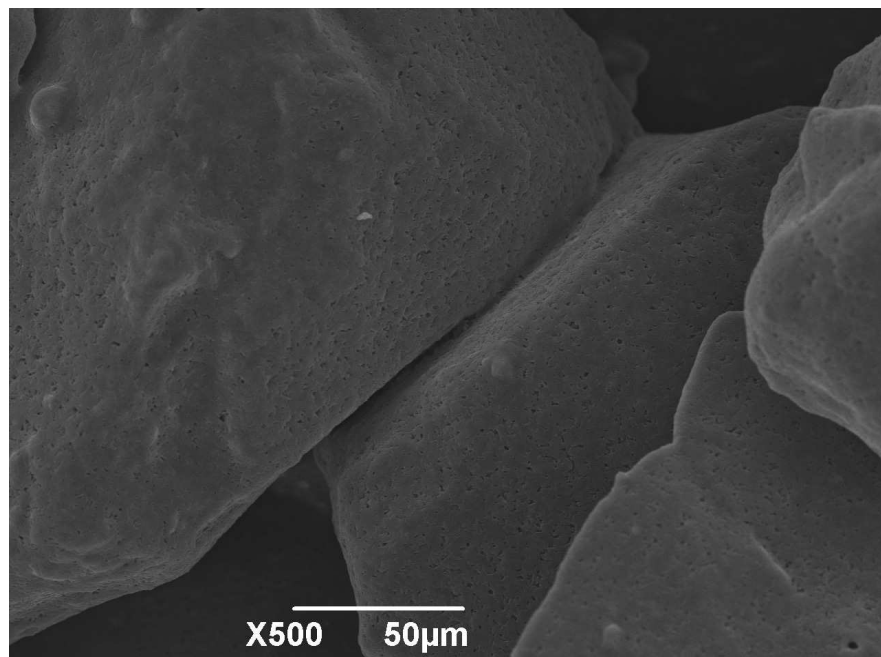
fig.93 SEM picture of the LAS3 particles partially sintered together

These connections are limited, so one can expect a low mechanical strength for this

scaffold.

The grains are composed of rod crystals of approximatively 5 μm (**fig.94**), of spodumene according to XRD (see section 3.2.3). The diffractogram measured for the 3D printed and sintered material is pretty much the same of fig.41.
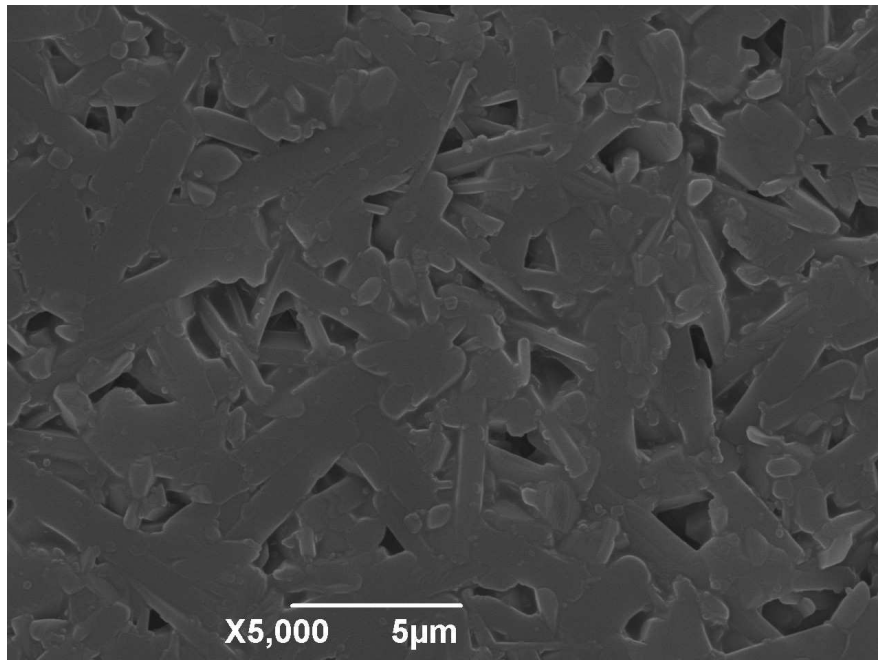
fig.94 crystals of spodumene in the sintered LAS sample

Fig.95 represents the base of a column of sample F (powder 63-125 μm), showing that the connection zone is homogeneous and so the column is well joint to the rest of the structure.
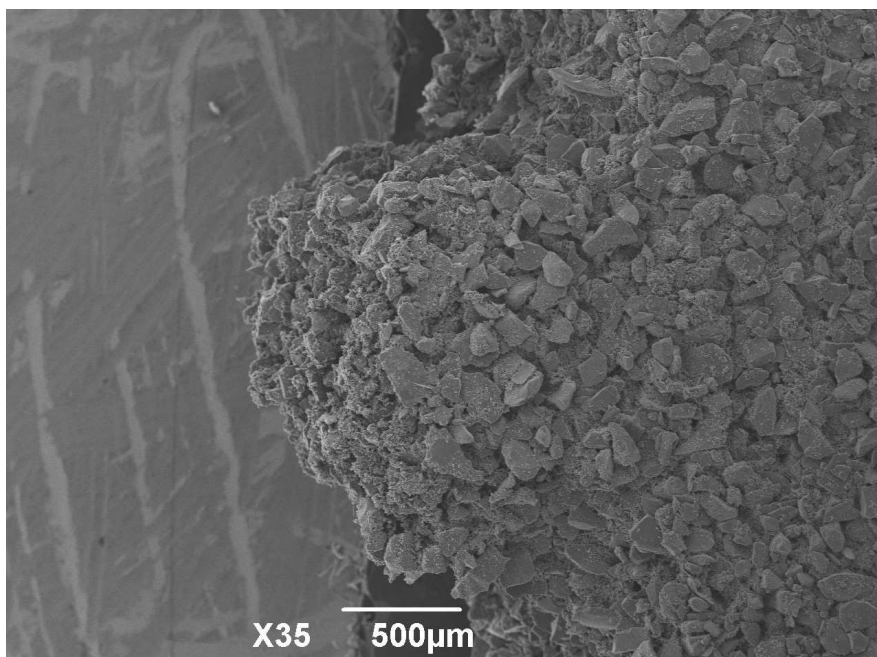
fig.95 SEM picture of a column of LAS scaffold F

Finally, **fig.96** shows a cell of sample G, which seems to have the best packing (**fig.97**) amongst all the samples, resulting also in a better sintering of the grains.
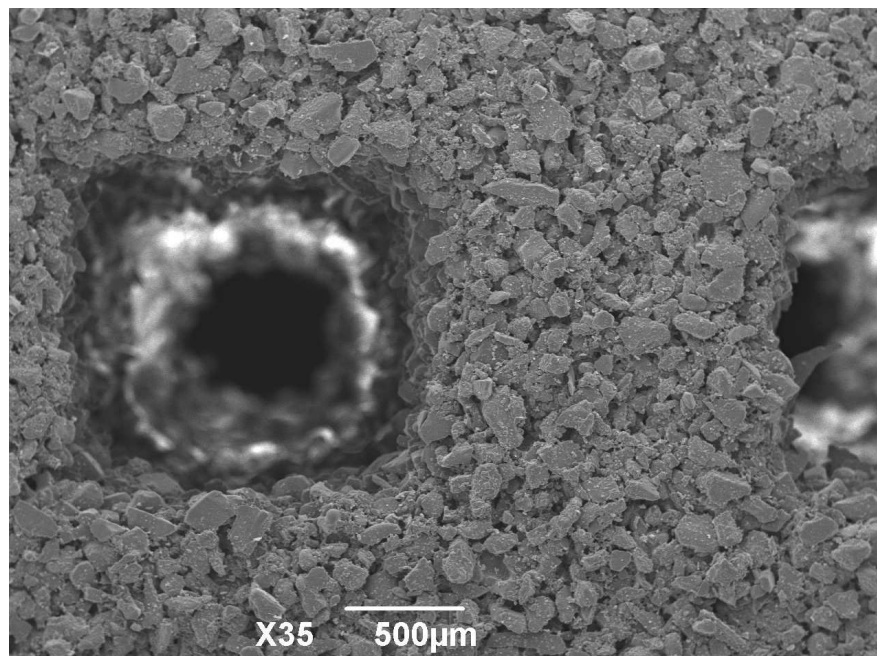
fig.96 SEM picture showing a cell of scaffold G
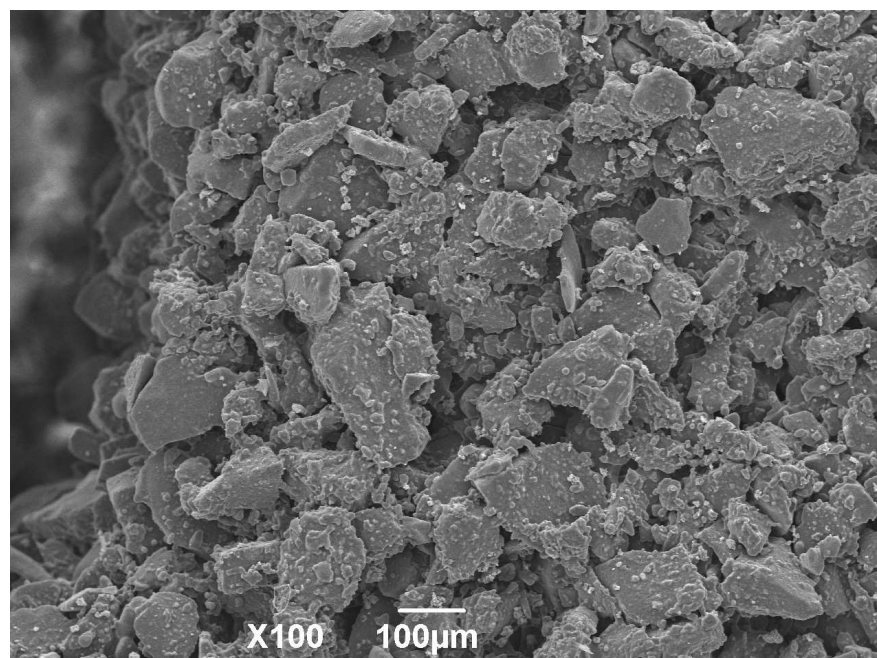
fig.97 SEM picture showing the packing of the sintered powder in sample G

4.3 Density

All the densities (except for samples A and B that were broken) were measured by Archimide's or geometrical method, and the results are summarized in **tab.10**

sample	powder	LT	P	DT	Apparent density (g/cm3)	Total Porosity	Struts density (g/cm3)	Struts porosity
C	63-125	100 μm	10	60 s	0.94	62%	1.42	40.2%
D	>125	200 μm	10	60 s	0.96	61%	1.39	41.0%
E	>125	200 μm	20	120 s	0.95	61%	1.47	38.4%
F	63-125	80 μm	15	60 s	1.10	56%	1.51	36.6%
G	63-125	100 μm	20	300 s	0.90	64%	1.57	34.2%

tab.10 density measures of the LAS samples

Two types of porosity are present in the scaffolds:

- – macro-porosity, that means the empty cubic cells
- – micro-porosity, that means the open porosity between the granules or possibly some close porosity, inside the struts or inside the single granules

It is reasonable to expect that the major part of the the porosity is open.

The apparent density is the ratio between the mass and the total exterior volume, and was determined geometrically. This value takes in account all the porosity, either macro or micro.

By Archimede's instead is possible to measure the density and the open porosity of the struts, from the dry, suspended and saturated weights.

The apparent porosity is mostly related to the geometry of the scaffold, so since all the models have the same geometry (except C), the values are similar.

Variations are due to the fact that the theoretical geometry is never perfectly reproduced and also to different strut density.

The samples with the powder >125 μm tend to have a slightly bigger side and lower strut density, but also the cells are smaller than expected (see fig.78) so at the end a similar geometrical density is achieved.

Sample F instead has a more dense structure and also some cells are not well printed (fig.82) so this explains the higher geometrical density.

Regarding sample G, it has higher strut density, but it also has the most precise struts, with a cell size similar to the geometrical model; so at the end it has the lowest density.

The struts have a lot of open porosity, up to 41% for sample D. With 3D printing a low porosity can not be obtained, because the powder is not pressed. Furthermore the powders used for 3D printing are usually quite big, so it is almost impossible to completely densify the structure during sintering.

The lowest porosity however is 34.2% for sample G; this specimen was printed with 20 passes (double of standard) and a long curing time of 300 s, and this permits to achieve a better packing and so also a better density after sintering.

In general it was observed that increasing the number of passes (that means the amount of binder) and the curing time, results in a better accuracy and an increased density.

CHAP 5: CONCLUSIONS

Two rapid prototyping techniques were investigated for the production of ceramic scaffolds.

Laser sintering of layerwise slurry deposition was used employed, with a CO_2 laser, on layers deposited from a silica slurry and it was proved that is possible to build up a scaffold.

A slurry of composition 60% silica, 6% nano-silica, 34% water titrated to pH7 and without organic additives has suitable characteristics for the process.

With the layerwise slurry deposition a high density of the green layers could be achieved, up to 71% of the theoretical density, so close to the theoretical maximum packing value.

A good precision was obtained in the x-y laser plane, but the surface along the z-axis resulted rough and laddered.

An LAS glass-ceramic slurry was also developed; a good stability and viscosity could be achieved with a slurry composed of 75.5% powder, 2.5% PEG and 22% water.

This slurry however could not be used for the automatic process because it dries out too quickly.

Other slurries with an addiction of hydroxyethylcellulose or PVA were prepared to improve the drying behaviour, but they still have to be developed to improve the quality of the layers.

The effect of the laser parameters on an LAS tape was studied, sintering $1cm^2$ squares in a range 15-39 W and 20-80 mm/s, with a fiber laser.

After sintering the material remained amorphous, probably because even if there is enough energy for the crystallization, kinetically there is no enough time for it to happen.

A range of stability was found, where the material is completely sintered but it is not damaged. Yet, also the "stable" parts reveal big bubbles under the surface, an excessive penetration depth and a non homogeneous structure.

The presence of a few percent of organics was proved to have an important role in the laser absorption.

So, in order to optimize the laser sintering, two ways are possible for further studies. The first is to investigate scan velocities higher than 80 mm/s, where another zone of stability is possible. The second and probably more interesting, would be to regulate the organic percentage to achieve a tailored absorption, avoiding the bubbles formation and the other defects.

The influence of the laser parameters on the line width was also investigated, revealing that the minimum width possible for a complete line is about 200 μm.

The same CAD model used for laser sintering of the silica scaffold was used in a completely different 3D printing machine, and with LAS, a different material, showing the outstanding versatility of Rapid Prototyping.

Different printing parameters were used and their effect was analyzed: powder size, printing "passes", layer thickness and curing time.

After printing, the binder was burned at 400°C and the LAS was crystallized and sintered at 860-870°C for 8h. The resulting crystalline phase is composed mainly of β-spodumene and also some lithium silicate.

The bigger powder had a better flowability and with that was easier to build complex geometries as a scaffold.

On the other hand with this powder only a limited accuracy and surface finish can be obtained.

The finer powder was also used to build scaffolds and the better results were obtained increasing the curing time of the resin and doubling the standard number of passes.

In general it was observed that increasing the number of passes (that means the amount of binder) and the curing time, results in a better accuracy and an increased density.

The surface finish that was obtained with 3D printing is worse compared to the laser sintered surfaces in the x-y plane, but it has the advantage to be uniform along all the three axis, while big difference were noticed for the laser sintering process.

Scaffolds with a geometrical density of 0.9 g/cm^3 were printed (64% total porosity), where also the struts are highly porous, with an opened porosity up to 41%.

Objects with a high density are not possible to produce by 3D printing, because the powder is not pressed by the roller.

So, when a low porosity and high mechanical strength are required, the laser sintering seems to be more convenient.

To conclude, with both processes is possible to build 3D scaffolds, but they have different advantages and disadvantages.

LS of LSD is more suitable for producing dense parts and it is fast when the starting material is well known.

A drawback of this process is that many aspects have to be optimized for each new material, first the slurry and then the laser parameters; furthermore some materials may not

stand the high temperatures caused by the laser.

With 3D printing instead a lower density and probably lower mechanical properties can be obtained, but this machine has the advantage that is very simple to use and versatile, even if also this process needs to be optimized for the best results.

Bibliography

(1) Ian Gibson "Advance Manufacturing Technology for medical applications" 2005

(2) T. D. Roy, J. L Simon, J. L Ricci, E D. Rekow, V.P Thompson, J . Parsons; "Performance of hydroxyapatite bone repair scaffolds created via three-dimensional fabrication techniques"; Journal of Biomedical Materials Research Part A (2003) Volume: 67, Issue: 4, Pages: 1228-1237

(3) M.G. Manera, J. Spadavecchia, D. Buso, C. de Julian Fernandez, G. Mattei, A. Martucci , P. Mulvaney, J. Perez-Juste, R. Rella, L. Vasanelli, P. Mazzoldi, "Optical gas sensing of TiO2 and TiO2/Au nanocomposite thin films" Sens. Act. B, 132, 107 (2008)

(4) Chua C.K., Leong K.F. and Lim C.S.: "Rapid Prototyping" (second edition), World Scientific, 2001

(5) Xiaoyong Tian, Dichen Li and Jürgen G. Heinrich (2011). "Net-Shaping of Ceramic Components by Using Rapid Prototyping Technologies"; Advances in Ceramics - Synthesis and Characterization, Processing and Specific Applications, Costas Sikalidis (Ed.), ISBN: 978-953-307-505-1, InTech, Available from: http://www.intechopen.com/articles/show/title/net-shaping-of-ceramic-components-by-using-rapid-prototyping-technologies

(6) Griffith, M. L. & Halloran, J. W. (1996). "Freeform fabrication of ceramics via stereolithgraphy", *J. Am. Ceram. Soc.*, 79, 2601-2608.

(7) Bandyopadhyay, A.; Panda, R. K.; Janas, V. F.; Agarwala, M. K.; Danforth, S. C. & Safari, A.(1997). "Processing of piezocomposites by fused deposition technique", *J. Am. Ceram.Soc.*, 80, 1366–72.

(8) Lous, G. M.; Cornejo, I. A.; McNulty, T. F.; Safari, A. and Danforth, S. C. (2000). "Fabrication of piezoelectric ceramic/polymer composite transducers using fused deposition of ceramics", *J. Am. Ceram. Soc.*, 83, 124–28.

(9) Cappi, B.; Oezkol, E.; Ebert, J. & Telle, R. (2008). "Direct inkjet printing of Si3N4: Characterization of ink, green, bodies and microstructure", *J. Euro. Ceram. Soc.*, 28, 2625–2628.

(10) Lejeune, M. & Chartier, T.; Dossou-Yovo, C. & Noguera, R. (2009). "Ink-jet printing of ceramic micro-pillar arrays", *J. Euro. Ceram. Soc.*, 29, 905–911.

(11) Travitzky, N.; Windsheimer, H.; Fey, T. & Greil, P. (2008). "Preceramic paper-derived Ceramics", *J. Am.* Ceram*. Soc.*, 91, 3477–3492.

(12) Schindler, K. & Roosen, A. (2009). "Manufacture of 3D structures by cold low pressure lamination of ceramic green tapes", *J. Euro. Ceram. Soc.*, 29, 899–904.

(13) Regenfuss, P.; Streek, A.; Ullmann, F.; Suess, T.; Hartwig, L.; Horn, M.; Kuehn, Ch.; Ebert, R. & Exner, H. (2008). "Laser micro sintering of ceramics- reaction models and results", *cfi/Ber. DKG*, 85, 65-72.

(14) Bertrand, Ph.; Bayle, F.; Combe, C.; Goeuriot, P. & Smurov, I. (2007). "Ceramic components manufacturing by selective laser sintering", *App. Surf. Sci.*, 254, 898-992.

(15) Friedel, T.; Travitzky, N.; Niebling, F.; Scheffler, M. & Greil, P. (2005). "Fabrication of polymer derived ceramic parts by selective laser curing", *J. Euro. Ceram. Soc.*, 25, 193–197.

(16) J-P. Kruth, P. Mercelis, J. Van Vaerenbergh, L. Froyen, M. Rombouts, (2005) "Binding mechanisms in selective laser sintering and selective laser melting", Rapid Prototyping Journal, Vol. 11 Iss: 1, pp.26 - 36

(17) Yiquan Wu, Jing Du, Kwang-Leong Choy, Larry L. Hench (2007) "Laser densification of alumina powder beds generated using aerosol assisted spray deposition" ; Journal of the European Ceramic Society 27 (2007) 4727–4735

(18) J. G. Heinrich, A. Gahler, J. Gu¨nster, M. Schmu¨cker, J. Zhang, D. Jiang, M. Ruan "Microstructural evolution during direct laser sintering in the Al2O3–SiO2 system" (2007); J Mater Sci (2007) 42:5307–5311

(19) A. M. Waetjen, D. A. Polsakiewicz, I. Kuhl, R. Telle, H. Fischer; "Slurry deposition by airbrush for selective laser sintering of ceramic components"; Journal of the European Ceramic Society 29 (2009) 1–6

(20) J. Gunster, Engler, J. Heinrich; "Forming of complex shaped ceramic products via layerwise slurry deposition (LSD)" Bull.EcerS, 2003, 1, 25-28

(21) A. Gahler, J.G. Heinrich, J. Günster: Direct laser sintering of Al2O3-SiO2 dental ceramic components by layer-wise slurry deposition. J. Am. Ceram. Soc. 89 (2006), 3076-3080.

(22) Sachs, E.; Cima, M.; Williams, P.; Brancazio, D. & Cornie, J. (1992). "Three dimensional printing: rapid tooling and prototyping directly from a CAD model", *J. Eng. Ind.*, 114, 481-488.

(23) A. Gahler, J. G. Heinrich, H. Kawanowa, F. Schwertfeger, J. Günster: 3D laser surface sintering of SiO_2 green bodies. Int. J. Appl. Ceram. Technol. **3** (2006), 331

– 335.)

(24) Beta-spodumene ceramics for high temperature applications, Beall; Douglas M. (Painted Post, NY) Beall; George H. (Big Flats, NY) U.S Patent Documents: 3600204; 3839001; 4301214; 4595662; 5179051; 5403787; 5962351

(25) M. Mott, J. R.G. Evans; "Solid Freeforming of Silicon Carbide by Inkjet Printing Using a Polymeric Precursor"; Journal of the American Ceramic Society Volume 84, Issue 2, pages 307–13, February 2001

(26) V. V. Shumkova, V. M. Pogrebenkov, A. V. Karlov, V. V. Kozik and V. I. Vereshchagin; " Hydroxyapatite-Wollastonite Bioceramics" Glass and Ceramics Volume 57, Numbers 9-10, 350-353

(27) E. Bernardo, E. Tomasella, P. Colombo, "Development of multiphase bioceramics from a filler-containing preceramic polymer"; Ceramics International 35 (2009) 1415–1421

(28) Ischenko, V.; Harshe, R.; Riedel, R.; Woltersdorf, J.; "Cross-Linking of Functionalised Siloxanes with Alumatrane: Reaction Mechanisms and Kinetics" J. Organomet. Chem., 691 (2006) 4086-4091.

(29) E. Bernardow, P. Colombo, E. Pippel, J. Woltersdorf; "Novel Mullite Synthesis Based on Alumina Nanoparticles and a Pre-ceramic Polymer"; J. Am. Ceram. Soc., 89 [5] 1577–1583 (2006)

(30) Glass- Ceramic Technology, W.Holland and G.Beall, The American Ceramic Society, Westerville, OH, USA, 2002

(31) F. Klocke, C. Derichs, C. Ader, A. Demmer; "Investigations on laser sintering of ceramic slurries"; Prod. Eng. Res. Devel. (2007) 1:279–284

(32) J. Fletcher, A. Hill; "Making the connection - particle size, size distribution and rheology"; chemeurope.com

(33) Gauckler LJ (2000) Ingenieurkeramik 2-Herstellung von Keramik, vol 2. ETH-Zurich, Zurich

(34) George W. Scherer; "Theory of drying"; J. Am. Cerum. Soc., 73 [l]3 -14 (1990)

(35) W. Lan and P. Xiao; "Constrained Drying of Aqueous Yttria-Stabilized Zirconia Slurry on a Substrate. I: Drying Mechanism"; J. Am. Ceram. Soc., 89 [5] 1518–1522 (2006)

(36) André Gahler. "Direktes lasergestützes Rapid Prototyping im binären System Al_2O_3-SiO_2". February 2007.

Acknowledgements

My gratitude goes to Professor Jürgen Heinrich and Professor Jens Günster for the chance that they gave me to study at INW in Clausthal and to work at BAM in Berlin.

I am very grateful to Thomas Mühler, who has been a patient supervisor and first of all a good friend.

Many thanks to Carina, Firas and Simon, because it has been a pleasure to work with them at the institute and to Mr. Görke and Mr. Zellmann for their technical support. Thanks to all the wonderful people that I've met in Clausthal.

Ringrazio il Professor Paolo Colombo e il Professor Enrico Bernardo, per tutto il supporto che mi è stato dato in questi mesi e che mi ha permesso di vivere questa esperienza.

I miei ringraziamenti vanno anche alla ditta Colorobbia S.p.a. che mi ha fornito il materiale per gli esperimenti e in particolare a Luciano Pellicci e Giovanni Baldi per il loro cortese aiuto.

Ringrazio la mia famiglia, i miei genitori e mia sorella che mi hanno supportato economicamente e moralmente nel mio percorso di studi e personale. Non posso dimenticare Miriam che pazientemente mi ha sopportato in questi mesi e non mi ha mai fatto mancare il suo affetto.

Un ultimo ringraziamento va ai miei nonni, che mi custodiscono e che spero aver reso fieri di me.